Eötvös Loránd Tudományegyetem

MTA doktori értekezés

Szövetszerkezet kialakulásának kristálytani aspektusai polikristályos Al rendszerekben

Írta Prof. Dr. SIDOR Jurij

Informatikai Kar

Savaria Műszaki Intézet

Szombathely, 2020

Eötvös Loránd University

Doctoral Dissertation

for gaining the degree of Doctor of the Hungarian Academy of Sciences

Crystallographic aspects of microstructure evolution in polycrystalline Al systems

Prof. Dr. Jurij SIDOR
Faculty of Informatics
Savaria Institute of Technology

Szombathely, 2020

Table of Contents

Dedicated to my beloved ones: daughters Krisztina and Anna as well as my wife Andriana.

Acknowledgement

This work would not have been possible without the support of my wife Andriana, brother József and sister in law Mila as well as my dear parents Magdolna and József.

Special thanks to my friends and former colleagues: Roumen Petrov, Leo Kestens, Alexis Miroux, Tricia Bennett, Orlando Leon, Maria Santofimia, Tuan Nguyen, Victor Carretero, Alexandar Davidkov, Vitaliy Blyznyuk, Hadi Pirgazi, Edgar Gomes, Elisabete Pinto, Koen Decroos and Linsey Lapeire, with whom I spent nine wonderful years in Delft and Ghent.

Jaroslav Kish is gratefully acknowledged for his friendship and numerous consultations on C++ programming.

Paul van Houtte, Ricardo Lebensohn, Qingge Xie and Anand Kanjarla are gratefully acknowledged for collaboration, making available crystal plasticity codes and many fruitful discussions.

List of abbreviations

Alamel – advanced Lamel (model);
ARB – Accumulative roll bonding;
ASR – asymmetric rolling;
BCC – body centered cubic (crystal structure);
CP – crystal plasticity;
DC – Direct Chill (casting);
EBSD – electron back scattering diffraction;
FCC – face centered cubic (crystal structure);
FCT – full constraints Taylor model;
FEM – finite element model;
FLM – flow line model;
GPT – Growth potential textures;
HAGB – high angle grain boundaries;
HEM – homogeneous effective medium;
HSZ – highly strained zones;
ID – texture index difference;
ID_N – normalized texture index difference;
IPF – inverse pole figure;
ND – normal direction;
ODF – orientation distribution function;
PADZ – particle affected deformation zone;
PF – pole figure;
PSC – plane strain compression;
PSN – particle stimulated nucleation;
RD – rolling direction;
RVE – representative volume element;
RX – recrystallization;
SFE – stacking fault energy;
SGM – simple geometric model;
SIBM – strain induced boundary migration;
SPD – severe plastic deformation;
TD – transverse direction;
TF – Taylor factor;
TI – texture index;
TMP – thermomechanical processes;
VPSC – visco plastic self-consistent (model).

1. Introduction

Before reaching the final shape, metals are subjected to an intricate sequence of thermomechanical processes (TMP). In case of flat rolled products, the TMP comprises series of rolling and heat treatment steps, as it is revealed in Fig. 1.1. In commercial technological chain, the production of Al alloys starts with Direct Chill (DC)-casting to large ingots, which are subjected to homogenization annealing at 480-580 °C [1, 2s]*. Both the intercellular segregations and the soluble phases are dissolved in the course of homogenization treatment. Afterward, the ingot is transferred to the breakdown rolling mill (which could be either unidirectional or reversible) at elevated temperature. This technological step is followed by a high-speed multi-stand tandem hot rolling. The hot bands are coiled and cooled to room temperature before it is cold rolled to its final thickness, typically in the range of 0.6–1.2 mm. In some exceptional instances, materials are subjected to intermediate annealing. Subsequent to cold rolling, the deformed sheet is recrystallized in an annealing treatment, which is most commonly carried out on a continuous processing line. First the material is reheated to the recrystallization temperature to dissolve the hardening phases and then quenched to retain the alloying elements in solid solution. The cold rolled sheet tends to recrystallize during the reheating stage. After annealing, the age hardenable Al alloys are pre-aged for stabilization and improvement of age hardening response before being supplied for further stamping or other deformation operations.

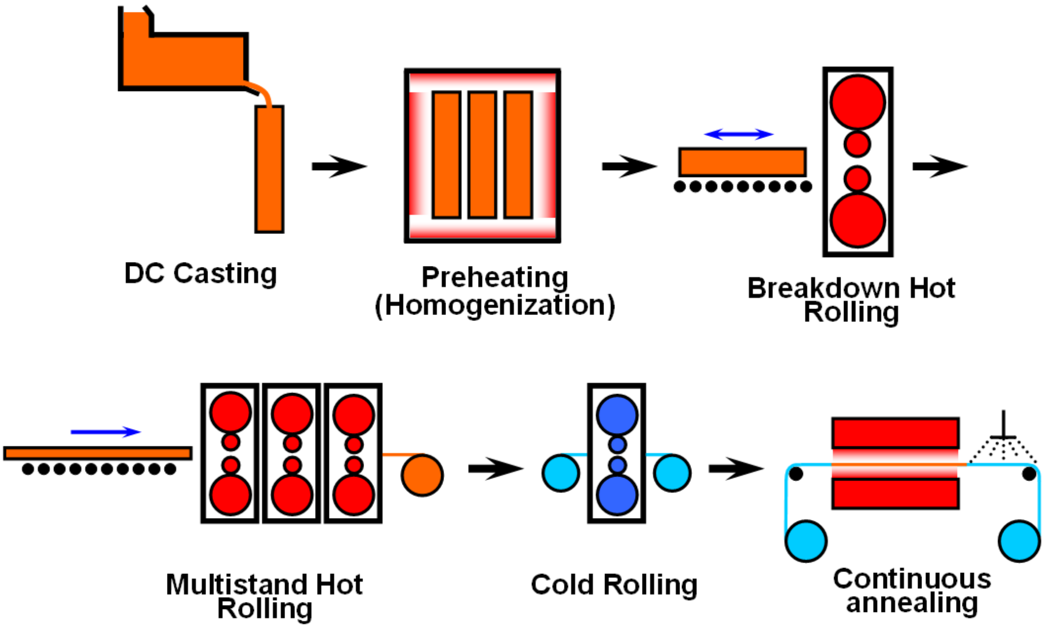

Fig. 1.1. Schematic illustration of TMP of flat Al products [2s].

<u> Please note </u>that literature sources numbered as [xs] are (co)-authored by Jurij Sidor*

This work summarizes scientific activities in the field of microstructure and texture control in Al alloys described in great detail in Refs. [2s-35s] and focuses on the microstructural transformations involved in the last two steps of TMP chain, i.e. cold rolling and recrystallization annealing. The research activities, presented in this scientific contribution, cover the area of both conventional and innovative processing technologies. The last are as yet far away from industrial implementation, however, they may allow exploring the limits of material's performance. In conventionally produced materials, a particular property can be improved at the expense of others, while the aim of non-conventional processing is to enhance a spectrum of specific properties. The research program is mainly focused on the TMP of polycrystalline systems, which undergo various microstructural transformations (from nano to mm scale) and lead to the presence of preferred crystal orientations, called crystallographic texture. It is shown that particular "genetic" crystallographic correlations could be found on macro, micro and nanoscale lengths in the metallic materials. Furthermore, a spectrum of properties could be varied during the TMP without changing the chemical composition in a material. By way of contrast to conventional processing, the innovative technologies are capable of providing entirely new nano, micro and crystallographic features in polycrystalline aggregates and thus a spectrum of mechanical properties could be enhanced.

2. Importance and major goals of the research

The combined generic and applied aspects of the innovative technologies might explore new approaches in conventional technological processing of materials, which will allow improving existing and developing entirely new processes, capable of supplying materials with significantly improved qualities. For instance, both the yield stress and ultimate strength can be increased relatively easily in conventionally produced Al-alloys, however, the deep drawing quality of these materials drops due to crystallographic texture evolved. A solution to this problem can be found in non-conventional processing [18s, 20s, 36-49].

A material subjected to thermomechanical processing undergoes various solid-state transformations, which may lead to the presence of preferred crystal orientations and hence will induce a specific texture that is characteristic for the particular process in the TMP chain. The evolution of preferred crystallographic orientations in the rolled materials accounts for plastic anisotropy that conditions the practical application of materials, especially in deep-drawing processes. Materials of various crystal structures exhibit a different plastic anisotropy. For instance, BCC metals (body centered cubic crystal structure) account for the better drawability compared to FCC (face centered cubic crystal structure) materials [50, 51]. The main reason for this difference is the diverse types of crystallographic textures developed during the processing chain. The conventional measure of anisotropy is the Lankford value (*r*-value or normal anisotropy) measured in a tensile test at various angles with respect to the rolling direction (RD) and averaged by a trapezoidal rule. The normal anisotropy is defined as the ratio of the logarithmic strain in the sheet transverse direction to the logarithmic strain in the sheet normal direction (ND). The planar anisotropy is evaluated based on the *r*-value profile in the plane of a rolled sheet. In order to ensure a minimum level of deep-drawability, the material should exceed a normal anisotropy of 1 while the in-plane anisotropy should be minimized in the ideal case to 0.

During thermomechanical processing, the evolution of texture starts with the hot rolling process. Depending on the hot rolling conditions, the hot band texture is dominated by deformation or recrystallization (RX) texture components (*texture is discussed in detail in the following section*) or a combination of both. BCC metals like ferritic steels are usually characterized by the γ-fibre texture which is favorable for drawability. This texture naturally appears in BCC materials after conventional rolling and subsequent annealing. The γ-fibre texture ensures a high normal anisotropy of ~2 or even higher. However, in conventional rolling of FCC materials like aluminum alloys, the so-called β-fibre characterizes the deformation texture. The evolution of the crystallographic texture during recrystallization annealing is determined by a variety of process parameters and the precise chemical composition of the alloy. The β-type rolling texture is retained during continuous recrystallization, whereas discontinuous recrystallization accounts for an annealing texture dominated by the fibres and components different from the deformation counterparts.

Many efforts have been made to obtain a favorable deep drawing texture in Al alloys by means of conventional thermomechanical processing, but no satisfactory result has been obtained so far. Hence, the manufacturing process should be modified so as to strengthen the shear-type texture in the final product via modified conventional and non-conventional techniques. The non-conventional methods extend the possibilities for microstructure and properties control in rolled sheet and hence deserve a special attention from the research community.

In view of the above, the following ***aims*** were defined:

1. Clarifying the evolution of deformation textures in FCC metals during conventional and innovative processing methods by means of experimental evidences and numerical approaches.

2. Introducing effective modeling strategies for simulation of deformation textures by combining basic principles of crystal plasticity theories.

3. Developing and employing computationally efficient and accurate numerical approaches, which are capable of predicting the deformation flow of metals and can ensure quantitatively reasonable texture simulation in combination with the well-established crystal plasticity models.

4. Resolving the diversity of annealing textures in Al alloys by experimental observations and modeling approaches.

5. Comparing the crystallographic features of conventionally and non-conventionally processed Al alloys.

6. Explaining the microstructural heterogeneities, which tend to emerge during both deformation and recrystallization.

7. Analyzing the major sources of plastic anisotropy in Al alloys and employing efficient computational approaches for simulation of both normal and planar anisotropy.

8. Assessment of plastic strain ratio in terms of microstructural features and definition of the representative volume element for successful simulation of Lankford profile.

3. Materials, experimental procedures, computational methods, and texture description

3.1 Materials, experimental and computational procedures

In the current work, the evolution of crystallographic texture was studied in Al alloys from 3xxx, 5xxx, and 6xxx series: 6016 (Al-(0.25-06)Mg-(1-1.5)Si), 5182 (Al–2.8Mg–0.21Mn–0.14Si) and 3003 (Al-1.1Mn-0.4Fe-0.2Cu). It should be mentioned here that both the exact sample preparation procedure and corresponding investigation methodology are presented in detail in references [2s-35s]. The investigated materials for symmetric and asymmetric rolling were selected after casting, hot rolling or cold rolling followed by recrystallization annealing. Both recrystallized (heat treated) and deformed (rolled) samples were subjected to the through-thickness textures measurements by means of electron backscattering diffraction (EBSD) technique. The orientation data were collected and analyzed by the commercial OIM-TSL® software.

Sample preparation for orientation imaging microscopy (OIM) was performed according to the standard procedure, which comprises mechanical grinding and polishing as well as electrolytic polishing. The mechanical polishing procedure was finished with the DiaDuo-2 Struers®-type 1 μm diamond paste. The electrolytic polishing, as a final step of sample preparation for EBSD, was conducted for ~1 min at a voltage ranging between 18V and 30V with A2 Struers® electrolyte, cooled to temperatures between -5 and 0°C.

The Hikari-type EBSD detector was attached to a scanning electron microscope (SEM). The OIM data of the investigated material with fully recrystallized microstructure were collected at the acceleration voltage of 20kV, whereas, in the cold rolled sample, to avoid overlapping of acquired pattern with ones originating from the deeper layers, the acquisition was performed at a comparatively low acceleration voltage of SEM. Application of 15kV guaranteed appropriate OIM data acquisition. During OIM measurements, the sample was 70° tilted with respect to the EBSD detector. The EBSD mapping was performed on a hexagonal scan grid in the plane perpendicular to the sample transverse direction (TD-plane) extending over the entire thickness of the investigated sample.

In some instances, cold rolling textures were determined by measuring X-ray pole figures in the back-reflection mode. From a set of four pole figures ({111}, {200}, {220}, {311}) the orientation distribution functions were calculated using the conventional series expansion method. The XRD texture was measured in the surface and sub-surface regions both from the top and the bottom sides and also in the mid-thickness section of the sheets. The through-thickness texture was calculated by integrating all the sub-layer textures into one average texture. The orientation data were post-processed with the MTM-FHM software developed by Paul Van Houtte ©.

To enable the simulations of texture evolution by the Taylor-type homogenization crystal plasticity (CP) approaches employed, the deformation history in a form of strain velocity gradients should be provided to the given CP model. Both two-dimensional finite element method (FEM) (Deform 2D®) and recently developed flow-line model (FLM) [12s], as well as simple geometric model (SGM) [4s], were employed in the calculation of deformation flow. These approximations are capable of capturing strain heterogeneities across the thickness of a cold rolled sheet. In the FLM and FEM simulations, the material subjected to rolling was considered as plastic and isotropic. In FEM, the strain hardening phenomenon was described with the stress-strain curve fitted by piecewise linear segments, whereas the rolls were considered as fully rigid objects. Contrarily to FEM, the FLM employed neglects the strain hardening effect. The extracted outputs were used as an input for CP calculations. Results obtained by FEM-CP, SGM-CP and FLM-CP simulations were compared to each other and likewise with the experimentally measured counterparts.

3.2 Brief review on texture in metals with a face-centered cubic crystal structure

The evolution of crystallographic orientations during the thermomechanical processing chain is not of random nature and strongly influences the final properties of polycrystalline systems. More specifically the crystallographic texture is a major source of planar anisotropy of numerous mechanical and physical properties. In general, it can be said that material properties that are anisotropic in the single crystal are texture dependent in the polycrystalline aggregate.

There are many ways to describe the crystallographic texture in materials. In metals, pole figures (PF) and orientation distribution function (ODF) are the most frequently used methods to reveal the crystallographic nature of these polycrystalline systems [50-52]. However, it should be underlined, that texture representation by pole figures is not fully complete, since the PF reveals the distribution of a single direction of crystallographic lattice plane normal and, therefore, it is not possible to gain complete information on orientation of individual grains. In view of this, it is more reasonable to analyze the texture in terms of ODF. The crystallographic orientation of particular volume element with orientation (*hkl*)[*uvw*] (*hkl* and *uvw* are Miller indices, which refer to plane and direction) can be described in terms of three Euler angles (φ_1, Φ and φ_2). The relation between Miller indices and Euler angles is defined by the following equations [52]:

$$h = \sin\Phi \sin\varphi_2 \tag{3.1}$$

$$k = \sin\Phi \cos\varphi_2 \tag{3.2}$$

$$l = \cos\Phi \tag{3.3}$$

$$u = \cos\varphi_1 \cos\varphi_2 - \sin\varphi_1 \sin\varphi_2 \cos\Phi \tag{3.4}$$

$$v = -\cos\varphi_1 \sin\varphi_2 - \sin\varphi_1 \cos\varphi_2 \cos\Phi \tag{3.5}$$

$$w = \sin\varphi_1 \sin\Phi \tag{3.6}$$

$$k/l = \cos\varphi_2 \tan\Phi \tag{3.7}$$

$$h/k = \tan\varphi_2 \tag{3.8}$$

$$lw/(ku-hv) = \tan\varphi_1 \cos\Phi \tag{3.9}$$

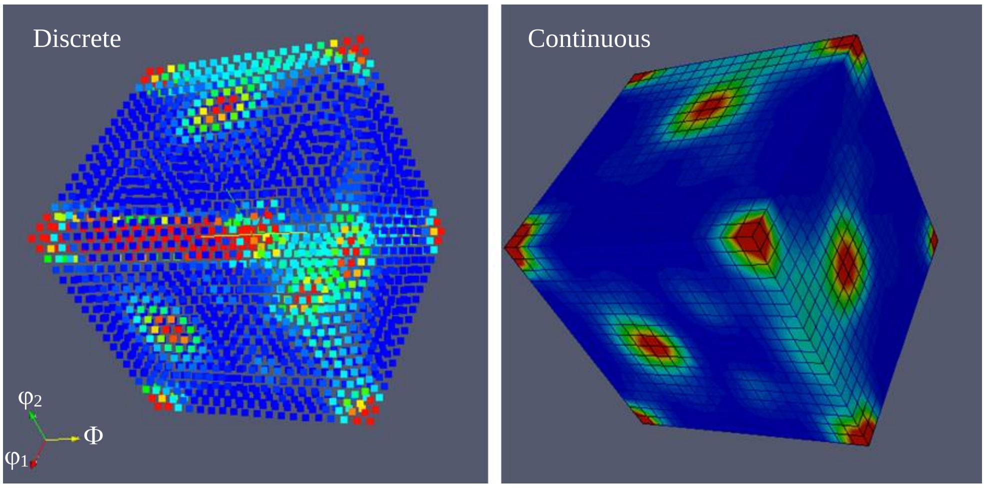

Fig. 3.1. Discrete dataset and continuous ODF in Euler space.

The ODF method was developed originally for flat materials with cubic crystal structures. The orientation distribution function is defined as a probability density function of given orientations. In the most general case, the ranges of the Euler angles are: $0 \leq \varphi_1, \varphi_2 \leq 360°$ and $0 \leq \Phi \leq 180°$; whereas for rolled materials with cubic crystal structure: $0 \leq \varphi_1, \varphi_2, \Phi \leq 90°$. It should be underlined here that if the orthotropic sample symmetry is broken (a typical example is asymmetric rolling), then the texture should be visualized in the following range: $0 \leq \varphi_1 \leq 360°$ while $0 \leq \varphi_2, \Phi \leq 90°$. Results of measurements, such as electron backscattering diffraction (EBSD), comprise data in discrete form and, hence, this dataset (see Fig. 3.1) needs to be transformed into a continuous function. Generally, this is done by employing spherical harmonic functions. The detailed mathematical algorithm, necessary to construct the ODF, is described by Bunge [52]. The interpretation of ODF, presented in 3D Euler space, is complicated and therefore the texture is usually shown as a series of sections in the form of contour maps taken through the 3D ODF space at φ_2 ranging from 0 to 90° (see Fig. 3.2).

During metal processing, a specific texture evolves during both hot and cold rolling of flat-rolled plates and sheets [17s, 51, 53-62]. The crystallographic changes involved in rolling are the consequence of the deformation mechanisms such as slip or twining. In turn, the dominant deformation mechanism depends on the stacking fault energy (SFE) of a material. In metals of medium and high SFE [51] (SFE > $0.25 \mathrm{mJm}^{-2}$), dislocation glide is dominant and the pre-rolling texture tends to rotate towards the α (⟨110⟩||ND) and β fibres (see Figs. 3.3-3.5). The α-fiber is usually dominated by the Goss ({110}⟨001⟩) and Brass ({110}⟨112⟩-B) orientations. The α and β-fibre textures are also known as pure metal textures. In metals of low SFE [51] (SFE<0.25mJ/m^2) such as Cu-Zn alloys (e.g. brass), the rolling texture is usually characterized by a strong {110}⟨112⟩ orientation and the γ-fibre (⟨111⟩||ND) texture components. This type of texture is also called the alloy-type texture since the alloying elements tend to reduce the SFE in metals.

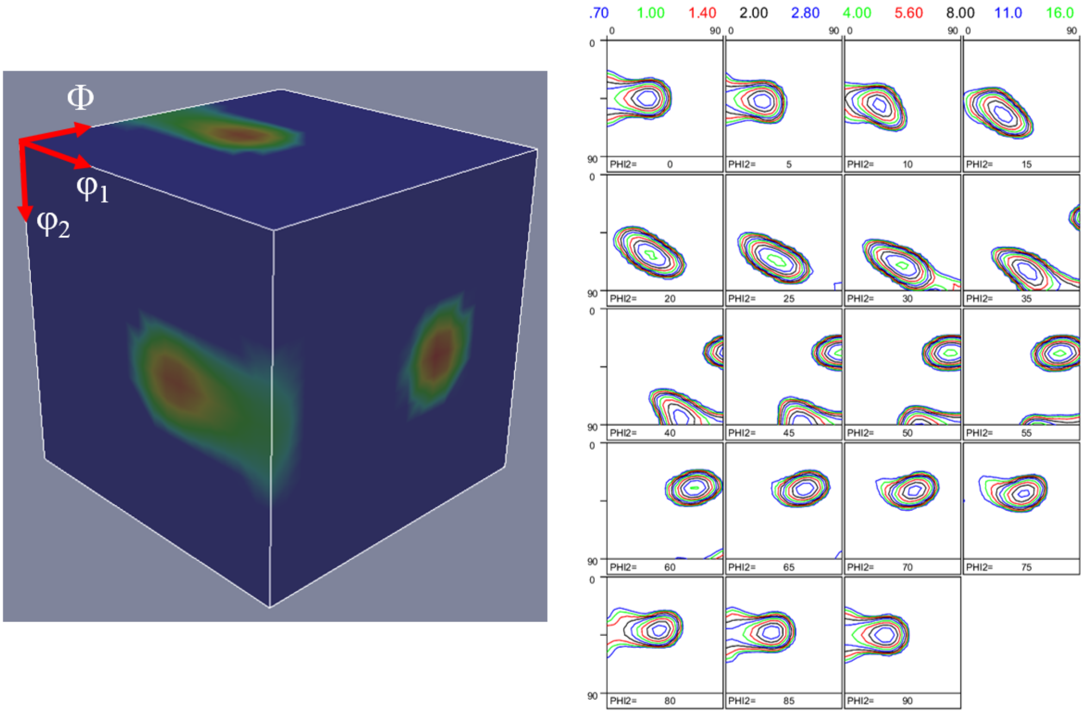

(a) (b)

Fig. 3.2. Continuous orientation distribution function in Euler space (a); and corresponding contour maps of the ODF (b).

The appearance of the θ-fibre (⟨100⟩||ND) orientations such as cube ({100}⟨001⟩) and the 45° rotated cube component ({100}⟨011⟩) in rolled material of high SFE is associated with the stability of the {100}⟨001⟩ orientation during rolling (due to the high symmetry of the cube orientation) and the occurrence of surface shear deformation, respectively [51]. A low-stacking fault energy austenitic Fe–Mn–C alloy (SFE ~ 20 to 40 mJ/m^2) exhibit both α and β-fibre orientations [58]. Similarly to brass, in the Fe–Mn–C alloy the intensity of orientations close to the {112}⟨111⟩ component (C or copper component) tends to fade. However, in brass the {112}⟨111⟩ is replaced by γ-fibre orientations whereas the Fe–Mn–C alloy reveals a consistent tube of orientations which extends from the C component towards the inverse brass component ({112}⟨110⟩) [58]. The appearance of a {110}⟨112⟩ dominated texture in low SFE materials is attributed to mechanical twinning and macroscopic shear bands [58-61].

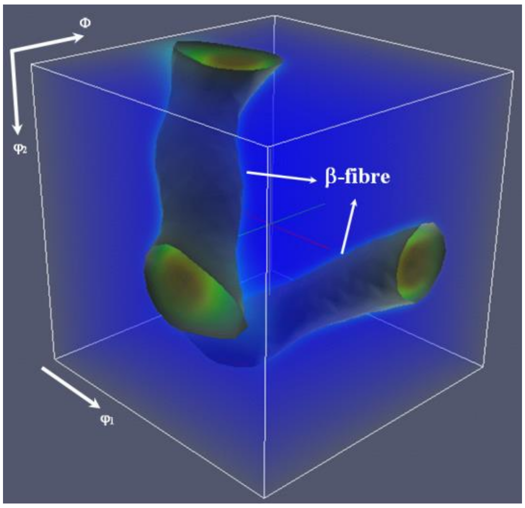

Fig. 3.3. Continuous orientation path (β-fibre) connecting the {112}⟨111⟩ and {101}⟨121⟩ orientations in Euler space.

Generally, the β-fibre is defined by a continuous orientation path in Euler space connecting a fibre of maximum intensity. Only a limited number of components along this fibre are described with low-index Miller indices [51-57, 62-68]. Different research groups have defined diverse stable orientations associated with deformation textures in FCC materials [51, 64, 65]. Hirsch and Lücke unified the deformation texture components into a fibre which connects the maxima in Euler space within a certain orientation spread [53]. Fig. 3.5 shows the position of these maxima along the β-fibre (running from the C to the B orientation in the first sub-space) observed in different materials [53-56]. It is obvious that the crystallographic position of the skeleton line varies from one material to another, depending on the SFE and the deformation mechanism. Significant differences are observed in the position of maxima between 70:30 brass (SFE ~20 mJ/m^2 [51]) and materials of higher SFE with a Cu-type texture. In brass, a consistent decrease in intensity is observed from {110}⟨112⟩ towards {123}⟨634⟩ (S), whereas the β-fibre tends to weaken or even totally vanishes in the vicinity of the {112}⟨111⟩ orientation [53].

Though the reported β-fibre textures, observed in both FCC and BCC structured metals, are described as an orientation tube or a skeleton line connecting the orientations {112}⟨111⟩ and {110}⟨112⟩ through the component {123}⟨634⟩ [51-57, 64-68], this description is far from complete as it leaves the precise position of the fibre skeleton subject to scatter of numerous experimental observations. A precise crystallographic description of the fibres is required in order to enable the analysis of the deformation textures. The planes and axes of the deformation fibres (α, γ, and θ) shown in Fig.3.4 are well defined, whereas the same cannot be said about the β-fibre. The proposed analytical description of the β-fibre by Sidor and Kestens [13s] reveals that copper and brass orientations are connected in the Euler space via the number of precisely defined components:

$$\{h,\quad 1,\quad h+1\}\left\langle \frac{h(h+1)}{3/4-h},\quad \frac{2h(h+1)}{1/2-h},\quad \frac{h^2}{h-3/4}+\frac{2h}{h-1/2} \right\rangle \tag{3.10}$$

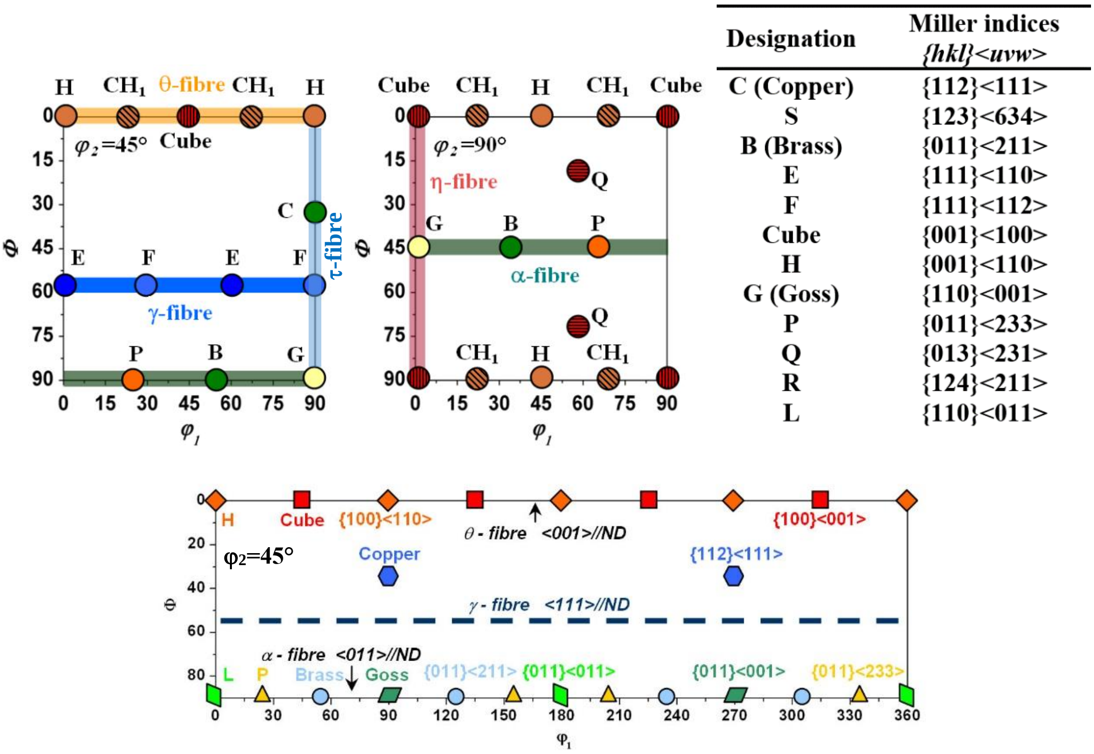

Designation	Miller indices *{hkl}<uvw>*
C (Copper)	{112}<111>
S	{123}<634>
B (Brass)	{011}<211>
E	{111}<110>
F	{111}<112>
Cube	{001}<100>
H	{001}<110>
G (Goss)	{110}<001>
P	{011}<233>
Q	{013}<231>
R	{124}<211>
L	{110}<011>

Fibre	Common axis of orientations
α	<011>//ND
β	$\{h,\quad 1,\quad h+1\}\left\langle \frac{h(h+1)}{3/4-h},\quad \frac{2h(h+1)}{1/2-h},\quad \frac{h^2}{h-3/4}+\frac{2h}{h-1/2} \right\rangle$
γ	<111>//ND
θ	<001>//ND
τ	<011>//TD
η	<001>//RD

Fig. 3.4. Main orientations and fibres which tend to appear in materials with FCC crystal structure [2s, 13s, 18s].

Formula 3.10 characterizes the following orientations along the β-fibre: *h*=1 - {112}⟨111⟩, *h*=1.5 - {325}⟨10 15 12⟩, *h*=2 - {213}⟨9 15 11⟩, *h*=3 - {314}⟨5 9 6⟩, *h*=7 - {718}⟨26 50 29⟩ etc and when *h*→∞ the formula reproduces the brass component {101}⟨121⟩. This analytical approximation of the β-fibre allows analyzing a deviation of specific texture components along this fibre with respect to its exact position (see Table 3.1 for details).

Table 3.1. The coordinates of β-fibre components in Euler space as predicted by formula 3.10.

φ_1	Φ	φ_2	{*hkl*}⟨*uvw*⟩
35.3	45.0	0.0	{101}⟨121⟩
33.6	47.7	5.0	
32.1	51.0	10.0	
31.1	54.7	15.0	
31.3	59.1	20.0	~{213}⟨9 15 11⟩
35.2	64.2	25.0	~{112}⟨111⟩
46.1	69.9	30.0	
49.5	76.2	35.0	~{213}⟨9 15 11⟩
51.8	83.0	40.0	
54.7	90.0	45.0	{101}⟨121⟩
90.0	35.3	45.0	{112}⟨111⟩
80.2	35.4	50.0	
73.0	35.7	55.0	~{325}⟨10 15 12⟩
66.9	36.2	60.0	
61.2	37.0	65.0	~{213}⟨9 15 11⟩
55.9	38.0	70.0	~{314}⟨5 9 6⟩
50.7	39.2	75.0	
45.6	40.8	80.0	~{718}⟨26 50 29⟩
40.5	42.7	85.0	
35.3	45.0	90.0	{101}⟨121⟩

Control of the deformed state is of key importance since it determines the initial structure for the subsequent recrystallization treatment. This is particularly true for texture as there is ample evidence that the cold rolling texture is of major importance for the ensuing recrystallization texture. Various combinations of the α and β deformation fibres produce a vast variety of recrystallization textures that strongly differ both qualitatively and quantitatively even though the metals under consideration have comparable values of SFE [1, 2s, 51, 54, 58]. For instance, although the deformation induced crystallographic patterns are qualitatively similar after diverse rolling reductions in various Al alloys (SFE≤162 mJ/m^2 [49]), the corresponding recrystallization textures, emerging after annealing, might show substantial differences [1, 54]. Generally, the ODF of conventionally cold rolled and recrystallized Al-Mg-Si alloys is typically characterized by the P, Goss and orientations scattered along the θ-fibre, while TMP of commercially pure Al triggers evolution of a single strong component from the θ-fibre, i.e. cube orientation [1, 2s]. Additionally, the qualitatively similar rolling textures, evolved in Al-Mg alloy after different straining levels, give rise to development of orientations characterized by different degrees of rotation along the θ-fibre [17s]. The differences in RX textures are attributed to various mechanisms of recrystallization [51, 62] which are affected by the deformed state, i.e. the deformed microstructure and associated deformation texture. In the most general case, it can be said that during discontinuous recrystallization, occurring at elevated temperatures, the deformation fibres of Al alloys transforms to the components located mainly along the θ-fibre mixed with the weaker α, γ and η-fibre orientations (see Fig.3.4).

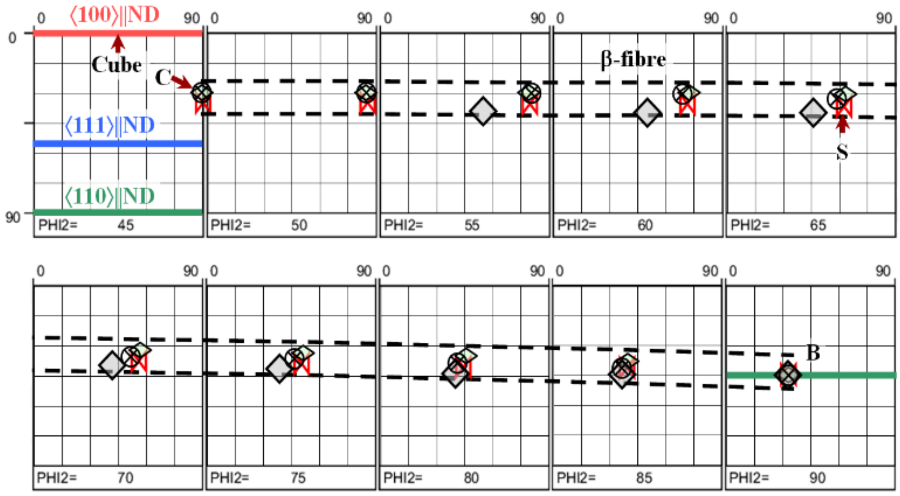

Fig. 3.5. Main fibres observed in rolled fcc materials [13s]. The points indicate maxima of orientations observed along the β-fibre in different materials: (◇) 70:30 brass after 75% rolling reduction [53]; (⊗) commercial purity Al (AA1145) after 95% cold rolling. [54] (◇) - Ni-5%W alloy after 95% cold rolling [55]; (⋈)- Ni-3%Al alloy after 80% thickness reduction [56].

4. Texture development during deformation: experimental evidences and numerical approaches

4.1 Concise description of modeling approaches employed in simulation of deformation textures

Metals are polycrystalline aggregates composed of numerous grains, which can be considered as perfect crystals if the material is fully recrystallized. In order to predict the behavior of polycrystalline materials subjected to macroscopic load, the relationship between microstructure and properties should be known, and therefore, the physically-based modeling is of key importance. The understanding of microstructural changes is particularly important in setting-up the thermomechanical processing route. In TMP, the as-cast microstructure is subjected to continuous microstructural transformation. In the case of flat-rolled products, this transformation is conditioned by both deformation and recrystallization phenomena, since after casting the material is subjected to hot rolling which is followed by cold rolling and finally the sheet is recrystallized during the final annealing process.

Various modeling approaches, which employ diverse length scales (Fig. 4.1), have been developed to reveal the behavior of materials during TMP [69]. It is a common practice to employ phenomenological models for the optimization of properties in a group of metals, which do not reveal substantial varieties in chemical composition [69, 70]. This strategy likewise works for tailoring a certain metal grade for a particular application. The main disadvantage of the phenomenological approximations is that the model parameters need to be re-calibrated in the case of a metal grade change or if the TMP quantitative indicators are varied in a wider range of processing window. In more advanced numerical formulations such as finite element models, materials are considered as continua, and thus, the mesoscopic phenomena, occurring on the grain levels, are not accounted for in this engineering length scale (Fig. 4.1). Nevertheless, FEM is successfully employed in many fields, especially when there is a need to simulate the response of a system, subjected to mechanical load. On the other end of the length-scale spectrum, the macroscopic properties are derived from the interatomic potentials and by engaging basic principles of molecular thermodynamics, which ensures generic information about relationships between the atomic arrangements and macroscopic properties, however, this formulation is applicable only for ideal systems. Application of atomistic length scale simulations to metals is restricted due to limitations in computational resources and also because of the fact that polycrystalline structures contain too many crystal defects even in the fully recrystallized state (typically 10^8 m^{-2}).

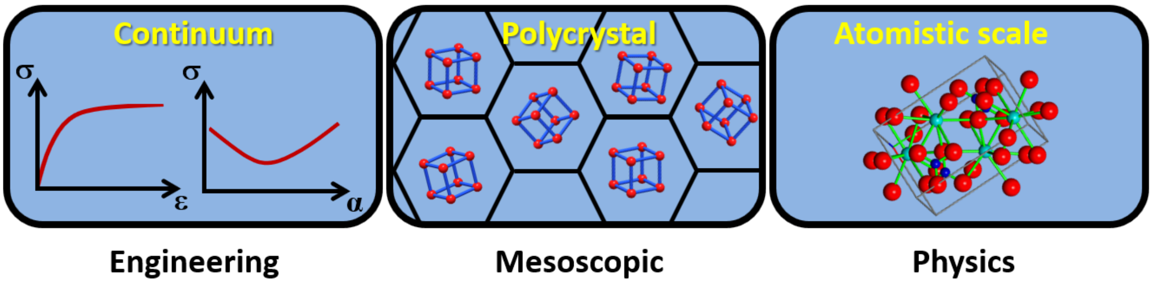

Fig. 4.1. Variety of length scales involved in modeling the microstructure-properties relationship [3s].

Since the 1 mm thick metallic sheet of A4 size (21cm×29.7cm) contains approximately 4 billion grains of various crystal orientations, assuming that the average grain size is 25 μm, it becomes clear that neither engineering (continuum) nor atomistic scales are not capable of revealing the true nature of mesoscopic transformation involved in TMP. To capture the essence of microstructural changes in industrially produced materials, both mean-field and full-field crystal plasticity models are employed [11s, 69, 71-76]. Either approach implements a certain homogenization scheme inasmuch as performing calculations for the above-mentioned 4 billion crystals, consisting of even smaller entities, would require enormous computational power. In CP, homogenization implies to the characteristic length scale (mesoscopic) represented by grains of polycrystalline aggregate, and these entities are treated as perfect crystals (the in-grain heterogeneities are usually not taken into account). The mesoscopic scale tends to fall between two ends of the characteristic length spectrum, and this level of order is important from a practical perspective as many of the known properties are controlled by the grain size and crystallographic texture. CP approaches treat the polycrystalline material as a continuum at the level of crystal because the grain size is the order of magnitudes larger compared to the size of molecular domains.

From mesoscopic perspective, the external work applied macroscopically to a material is transmitted to the individual grains, generating corresponding stresses-strain state in each grain of polycrystalline aggregate. This complex process can be captured by the full-field models [69, 71, 72], which allow analyzing not only the microscopic and macroscopic responses of material but also accounts for the evolution of heterogeneities at both levels. Although these methods give rise to a more comprehensive representation of a microstructure and provide detailed information on the deformation flow on the meso and macro length scales, their practical implementation is limited because of extensive computational time. By way of contrast, the mean-field models are more computationally efficient, but they have fewer degrees of freedom, compared to the full-field methods. For instance, in the mean-field approximations [11s, 73-76], each grain interacts with the neighboring one in a way defined by the homogenization scheme, the misorientation in the grain developed during deformation cannot be captured, and so on. Even though some microstructural features are ignored in the Taylor-type homogenization CP formulations such as visco plastic self-consistent (VPSC) [75], advanced Lamel (Alamel) [73, 74], Cluster V [11s] etc., simulations on mesoscopic scale are still capable of providing generic knowledge on the relationship between the structure, properties and performance of a polycrystalline aggregate. The main advantage of the mean-field approaches is that texture simulations can be completed within a time-frame of several minutes on a personal computer, while crystal plasticity full-field computation for the same straining level requires a couple of days on the far more powerful computer [23s]. The polycrystal models were successfully employed for simulating the evolution of texture in metals, subjected to diverse strain modes, calculating the plastic strain ratio as well as predicting the cup-earing [2s, 7s, 11s, 20s-22s, 73-76].

In order to make the application of crystal plasticity modeling practically attainable, the CP should be accoupled with the computationally effective approach, which is capable of accurate prediction of deformation flow in a material. When it comes to rolling, the simplest approximation is the plane strain compression, which disregards many aspects of the process. Because of its simplicity, this strain mode is often used in simulations and tends to provide a reasonable estimate of overall (bulk) texture evolution [11s, 20s, 73, 74, 77]. In FEM, the effect of many technological parameters on the deformation flow can be taken into account while the displacement history is accurately calculated for various materials at diverse temperatures, however, the model set-up and the calculation procedure are time-consuming. In view of this, deformation is often approximated by analytical solutions [12s, 78-83] such as flow-line models, which are capable of capturing many aspects of the process, however, the practical implementations of these computationally effective approaches are limited by fitting parameters, which have to be derived from the experimental data for each particular case.

Modeling the evolution of deformation texture in Al alloys, by combining basic principles of CP theories and models which are capable of predicting deformation flow, is vital since many crystallographic features evolved in deformation are directly linked to the evolution of recrystallization texture. The last determines the plastic anisotropy and limits the forming characteristics of a material.

There are many aspects of texture evolution during cold deformation, which are still not explained by existing models. In this view, this chapter describes the computationally efficient and accurate numerical approaches which can ensure quantitatively reasonable texture simulation. The well-established CP models were accoupled with various continuum mechanics-based models, enabling the simulation of material's flow during deformation.

4.1.1 Crystal plasticity models

Advances in crystal plasticity modeling have created a solid platform for understanding the texture evolution during processing [11s, 69, 71-76] and allowed a structure properties paradigm to be established. Development of crystallographic texture in polycrystalline materials, subjected to an arbitrary strain mode, is generally simulated by means of various CP approaches: the full constraints Taylor model (FCT) [73], the visco-plastic self-consistent (VPSC) model [75], the Alamel model [73, 74] and Cluster-V model [11s]. The common feature of CP models employed is that each particular grain is considered as a single crystal. However, these four approaches employ diverse grain interaction phenomena.

A reference theory of plastic strain in metals proposed by Taylor [73] became a platform for various crystal plasticity approaches, enabling to trace the crystallographic changes during deformation. The Taylor model enforces strain compatibility in a way that each particular grain/crystal experiences the same deformation as the sample. In this approach, the macroscopic strain velocity field L_{ij} and the microscopic strain velocity field of each crystal of the polycrystalline aggregate l_{ij} are identical. This approach is called a full constraints Taylor model as it maximizes the influence of geometrical constraints. In the FCT model, the deformation in each particular grain is accomplished by activation of five independent slip systems chosen by minimizing the dissipation energy P associated with this deformation. Apart from the FC approach, a short-range (Alamel) [73, 74], an intermediate-range (Cluster V) [11s] and a long-range (VPSC) [75] interaction models are employed for crystal plasticity calculations.

In multi-grain Taylor type interaction models such as Alamel or Cluster V the local interaction is assumed between a couple of grains or block of grains. In the multi-grain approaches, the global average of the strain rate tensors of the grains considered by the model is equal to the mean value of the prescribed strain rate of the polycrystal. However, the local strain rate of the individual crystal could deviate from the mean strain rate of the polycrystalline aggregate.

In the mean-field approach such as Alamel, the grain assembly is subdivided into a number of clusters (see Fig. 4.2), consisting of two grains, whereas the interaction inside the cluster is governed by the randomly chosen grain boundary orientation. Similarly to the above-mentioned Taylor-type models [11s, 73-75], the grain pair is subjected to a strain mode identical to the macroscopic one. The two grains in Fig. 4.2 represent the crystal orientations of two boundary layers at both sides of a segment of a grain boundary. The orientations of the grain boundary segments observed in the microstructure of materials are characterized by the grain boundary segments orientation distribution function. In this way, the model takes into account the microstructural features of the material subjected to deformation. The Alamel model is based on the following principles [73, 74]: (i) the local velocity gradient field l_{ij} is not uniform through a grain; as a result, the slip rates are not uniformly distributed either; (ii) stress equilibrium between regions 1 and 2 along the considered grain boundary segment must be satisfied; (iii) the average deformation along the considered grain boundary segment must be equal to the macroscopic deformation L; (iv) the set of crystallographic orientations which develop in various regions close to the grain boundaries can be considered as the contribution of the grain to the overall deformation texture of the polycrystal; (v) in the simulation, not all grain boundary segments are considered, but only a few thousand, selected randomly. The fact that the nature of relaxations is not related to the geometry of prescribed deformation makes the Alamel model applicable for any strain mode. It means that for instance in the case of rolling, the shear plane of two considered relaxations is not necessarily parallel to the rolling plane.

The visco-plastic self-consistent crystal plasticity models are much more complex than Taylor-type models. The formal theory and a comprehensive derivation of the algebraic and tensorial equations of the visco-plastic self-consistent formalism are explained in detail elsewhere [75]. This type of approach could be classified as generalized Relaxed Constraints (RC) models, in which the relaxations are determined on the basis of interaction between one particular grain and its surroundings (see Fig. 4.2). The VPSC model [75] assumes that the interaction of a grain with the surrounding matrix can be approximated by the interaction between the grain and a hypothetical homogeneous effective medium (HEM) which is characterized by an average constitutive behavior of the entire polycrystal aggregate. The VPSC deals with the ellipsoidal domain since the stress and strain rate are uniform within the inhomogeneous domain of ellipsoidal shape. In the model, the stress applied to the outer boundary of the HEM induces local deviations of strain rates in its vicinity. This problem is solved analytically by using the Eshelby inclusion formalism [75] which enables the calculation of the state of the considered grain without solving the local field outside the inclusion. The deviation of the strain rate in the grain with respect to the macroscopic average one is characterized by means of the interaction parameter n_{eff} in the constitutive low. Assumption of n_{eff} =0 accounts for a uniform strain-rate state in a polycrystalline aggregate that is known as Taylor or upper-bound approximation. Obviously, the secant formulation with $n_{eff} = 1$ is fairly stiff and resembles many features of the full constraints model. By way of contrast, the tangent approximation with $n_{eff} = 20$ leads to a relatively uniform stress state and when $n_{eff} \rightarrow \infty$ a stress deviation is zero (Sachs model) and therefore a lower-bound approximation is maintained. It is evident that the choice of a linearization scheme will affect the results of texture simulation. In this work, n_{eff} is considered to be 10, corresponding to an intermediate interaction between the secant and tangent confinements.

In the cluster V model [11s], the polycrystalline aggregate is subdivided into a number of clusters consisting of 5 grains, whereas each particular grain assembly is exposed to the Taylor type deformation. The grain interaction inside individual clusters is approximated by the VPSC linearization scheme with n_{eff} =10.

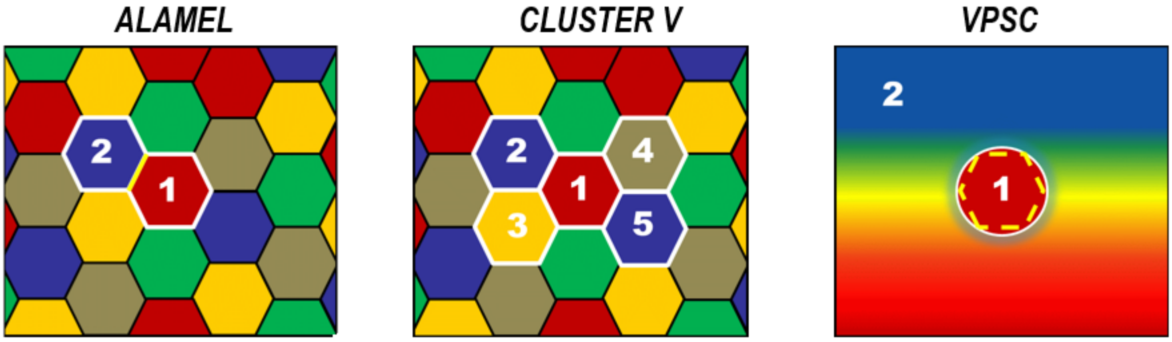

Fig. 4.2. Schematic representation of CP models.

The above-described models employ the rate-dependent and rigid-plastic Voce-type law for work hardening [84] in which the evolution of the threshold stress τ_a is correlated to the accumulated shear strain Γ:

$$\tau_a = \tau_0 + (\tau_1 + \Gamma\theta_1)(1 - \exp(-\Gamma\theta_0/\tau_1)) \qquad (4.1)$$

where τ_0, θ_0, θ_1, and $(\tau_0 + \tau_1)$ are: the initial threshold stress, the initial hardening rate, the asymptotic hardening rate and the back-extrapolated threshold stress, respectively.

It should be underlined here that preceding results of texture simulations [20s] with the mentioned work hardening framework, performed for 6xxx Al alloy, reveal that varying the values of strain hardening parameters has a negligible effect on the quality of texture prediction. However, it should be noted that this is not a case for polycrystals, which tend to deform by two various modes such as sleep and twinning. In these materials, first, the deformation is governed by one mechanism whereas exceeding a certain straining level induces another mechanism of deformation, and therefore, here the choice of right hardening parameters is of crucial importance. Material's behavior during deformation could be accurately captured with the strain-gradient formulations [85], multi-scale hierarchical approaches [86] or CP formulations based on fast Fourier transforms [72], however these modeling techniques are computationally intensive and not discussed in the frame of present work.

In the crystal plasticity formulations, the evolution of texture in FCC metals during cold deformation is related to the crystallographic slip on octahedral slip systems {111}<110>, whereas the macroscopic strain mode is approximated by various continuum mechanics-based full-field approaches.

4.1.2 Modeling the material's flow by continuum mechanics-based approaches

Geometrical Approaches

This section provides a summary of approaches described in [2s-4s, 12s]. The flow behavior of a material subjected to rolling can be described by various approaches with a diverse degree of accuracy. In many instances, rolling is considered as the plane strain compression (PSC) deformation, since this abstraction enables fast estimation of strain. PSC is the simplest geometrical approach, which is often used in approximating the rolling process. This analysis enables revealing the effect of an important technological parameter such as a normal strain on the change of material's shape. PSC is justified to a large extent due to the fact that the ratio between the compressive component of the strain velocity gradient tensor (L) and shear components L_{ij} ($i \neq j$) is large. In the case of PSC, the L tensor gains the following form:

$$L = \begin{bmatrix} L_{11} & 0 & 0 \\ 0 & 0 & 0 \\ 0 & 0 & L_{33} \end{bmatrix} \tag{4.2}$$

In this two-dimensional analysis, where $L_{12}=L_{21}=L_{23}=L_{32}=L_{13}=L_{31}=L_{22}=0$ (direction 1 is || to rolling direction, direction 2 is || to TD and direction 3 is || to ND), the L_{11} component might be approximated by the following formula:

$$L_{11}=\dot{\varepsilon}_{11}\approx\frac{1}{\Delta t}ln\left(\frac{h_i}{h_f}\right) \tag{4.3}$$

here h_i and h_f are the initial and final sheet thickness, whereas Δt is the time increment. This simple geometric approach accounts for a constant strain rate, which affects the results of simulations if the CP model is rate-dependent. In PSC the resulting strain rates are: $\dot{\varepsilon}_{11}=-\dot{\varepsilon}_{33}=L_{11}=-L_{33}$.

It should be underlined that equation 4.2 excludes the effect of (i) roll gap geometry (L_{31}), (ii) friction-induced shear component L_{13}, and (iii) strain heterogeneities, evolved across the thickness of a rolled sheet, whereas, the balance between the factors (i) and (ii) determines the evolution of the aspect (iii).

As rolling is not possible without friction, analyzing the effect of shear is of crucial importance. It was shown that the shear component, evolving due to the roll gap geometry, can be approximated by [88]:

$$\dot{\gamma}=\frac{\Delta h}{\Delta t(R\Delta h-(0.5\Delta h)^2)^{0.5}} \tag{4.4}$$

where R is a roll radius and $\Delta h = (h_i - h_f)$.

Both experimental and computational evidences [12s, 77, 88] claim that the L_{13} shear component is of positive sense at the entry of the rolling mill and becomes negative at the exit of the mill, while the roll gap geometry induced component L_{31} reveals an opposite tendency. As it was pointed out by Engler et al. [77], it is reasonable to adopt that both L_{13} and L_{31} follow an idealized sine-shaped profile. In the current geometric approach, it is assumed that L_{13} and L_{31} counterparts likewise follow a sine-shaped profile, while the compressive component ($L_{33}=-L_{11}$) evolves according to the half of the sine-profile during the rolling. In this case, the strain velocity gradient tensor gains the following form [3s, 4s]:

$$L=\begin{bmatrix}0.5\pi\dot{\varepsilon}_{11}\,sin(\pi\tau) & 0 & m^{-1}\pi\dot{\gamma}\,sin(2\pi\tau)\\ 0 & 0 & 0\\ -m\pi\dot{\gamma}\,sin(2\pi\tau) & 0 & -0.5\pi\dot{\varepsilon}_{11}\,sin(\pi\tau)\end{bmatrix} \tag{4.5}$$

Similarly to Eq. 4.3, the time increment is not explicit in this approximation and therefore the strain-rate dependent CP models will be sensitive to the choice of τ. In its simplest form, τ can be defined as a ratio of the instantaneous normal strain to its maximum value. The value of τ is ranging between 0 and 1, whereas $m>0$.

The m coefficient introduced in equation 4.5 ensures the balance between the friction-driven and geometry-induced shear components. The resulting shear $\dot{\varepsilon}_{13}$, which is the symmetric part of the strain velocity gradient tensor and calculated with the following expression $\dot{\varepsilon}_{13}=\dot{\varepsilon}_{31}=0.5(L_{13}+L_{31})$, depends on the value of m. As soon as m is larger than 1, the resulting shear $\dot{\varepsilon}_{13}$ becomes tilted toward the geometrical shear component L_{31} (see Fig. 4.3), which corresponds to rolling with (i) low friction coefficient μ (well-lubricated surfaces of both sheet and rolls), (ii) small thickness reduction and (iii) rolls of relatively small diameter. By way of contrast, rolling with large rolls under dry conditions (μ is relatively large) diminishes the effect of roll gap geometry and consequently the L_{13} component dominates over the L_{31}, which can be accounted for by setting $m<1$. It is apparent from equation 4.5 that as soon as $m=1$, the resulting shear $\dot{\varepsilon}_{13}$ is 0 since L_{13} and L_{31} cancel each other. By comparing strain rates of Fig. 4.3, computed for inversely proportional m values ($m=0.25$ and $m=4$), it appears that $\dot{\varepsilon}_{13}$ profile calculated with $m=4$ tends to mirror the counterpart calculated for $m=0.25$. The same stands for L_{13} and L_{31} profiles, which mirror each other at inversely proportional values of m. Independently of the choice of m, the integrated values of L_{13}, L_{31} and $\dot{\varepsilon}_{13}$ are equal to 0 because of the symmetry of sine-profiles, however, the instantaneous strain path strongly deviates from the plane strain compression.

A growing body of evidence claims that deformation across the thickness is inhomogeneous due to the unequal distribution of shear [12s, 77, 88-91]. Taking into consideration that shear strain γ is concentrated mainly within a thin sub-surface layer, it is reasonable to adopt an exponential character of shear distribution across the thickness:

$$\dot{\gamma}^{p} = \dot{\gamma}\, exp\left(\frac{s-1}{s}\right) \tag{4.6}$$

here, the superscript p indicates the position of a given layer with respect to the surface of a rolled sheet. In the equation, s varies between 0 and 1: $s=1$ for the surface, whereas if $s\rightarrow 0$, the friction-induced component becomes negligibly small, which is characteristic for the mid-thickness plane.

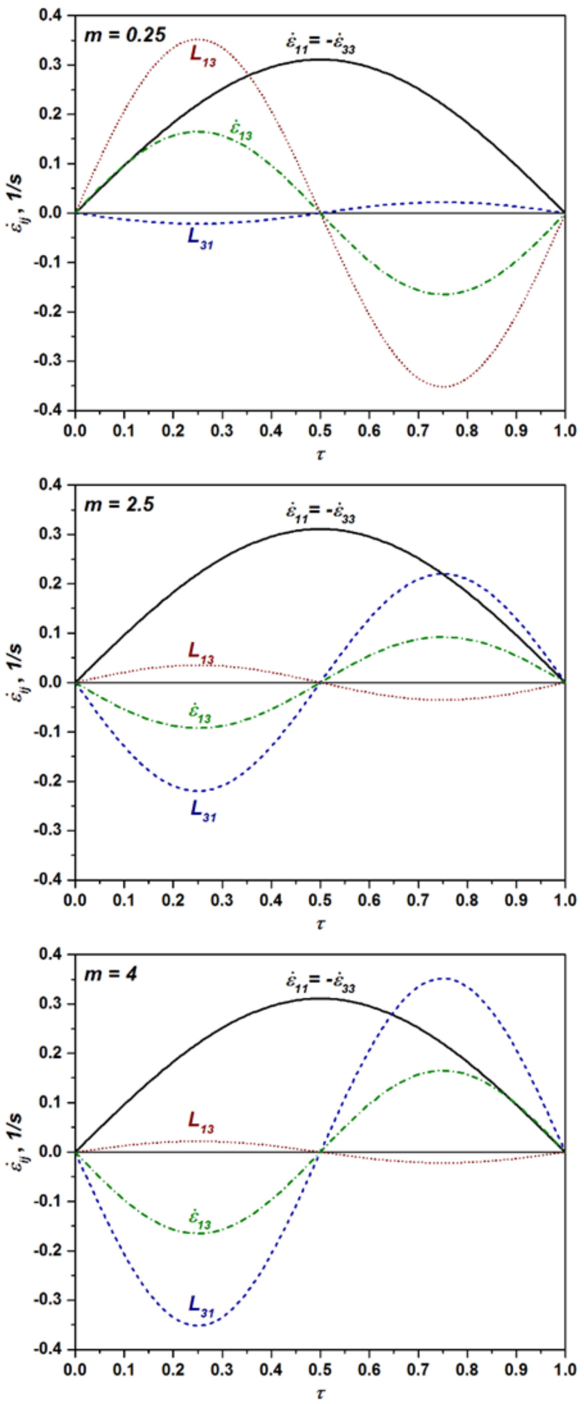

Fig. 4.3. Change of both friction (*L_{13}*) and roll gap geometry (*L_{31}*) induced shear components with model parameter *m*, employed in the geometric approach of Eq.4.5. The resulting shear $\dot{\varepsilon}_{13}$ and compressive $\dot{\varepsilon}_{33}$ strain rate components are calculated for 18% thickness reduction of 1.125 mm initially thick sheet, by employing rolls with a diameter of 129 mm [4s].

Combining equations 4.3-4.6 enables calculation of strain velocity gradient tensor L for various thickness layers (simple geometric model, SGM) [4s]:

$$L^p = \begin{bmatrix} 0.5\pi\dot{\varepsilon}_{11}\, sin(\pi\tau) & 0 & m^{-1}\pi\dot{\gamma}^p\, sin(2\pi\tau) \\ 0 & 0 & 0 \\ -m\pi\dot{\gamma}^p\, sin(2\pi\tau) & 0 & -0.5\pi\dot{\varepsilon}_{11}\, sin(\pi\tau) \end{bmatrix} \tag{4.7}$$

Inasmuch as laboratory rolling trials usually carried out with the small rolls under well-lubricated condition, it is rational to assume that m>1. Fig. 4.4 presents the evolution of stain rates for various through-thickness layers, calculated by equation 4.7 with m=5. Since in cold rolling the $\dot{\varepsilon}_{11}$ component is dominating over the $\dot{\varepsilon}_{13}$, the choice of m=5 is justified. As Fig. 4.4 reveals, the mid-thickness plane (s=0) experiences zero shear, while the amount of $\dot{\varepsilon}_{13}$ tends to increase in the sub-surface layers when $s \rightarrow 1$.

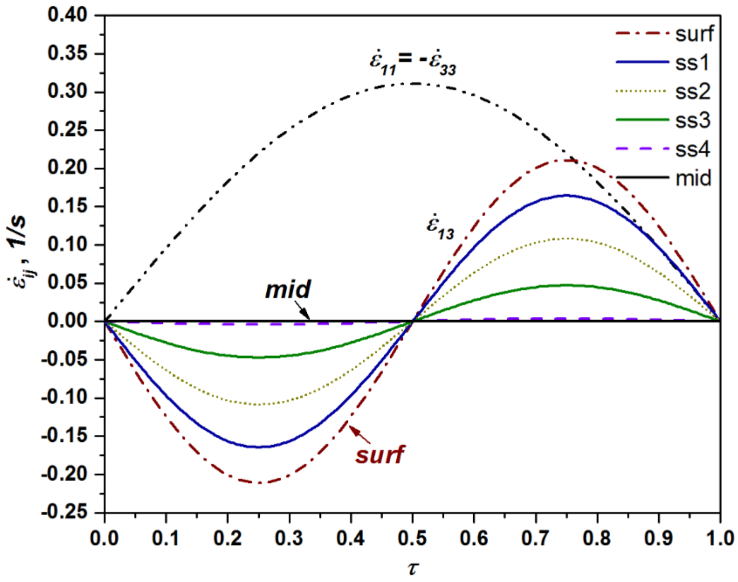

Fig. 4.4 Evolution of strain rates across the thickness of a rolled sheet, calculated by geometric approach (equation 4.7) with m=5 for: roll diameter of 129 mm, 18% thickness reduction, and initial sheet thickness of 1.125mm. On the graph, surf corresponds to s=1 (see equation 4.6 for details); ss1: s=0.8; ss2: s=0.6; ss3: s=0.4; ss4: s=0.2; mid: s=0. The $\dot{\varepsilon}_{33}$ is identical for all trough-thickness layers [4s].

Flow-line modeling approach

Numerous analytical approaches have been developed for accurate description of material's behavior in deformation and the main advantage of these models [12s, 78-80, 92-94] over other numerical approaches, such as finite element model [69], is their efficiency and accuracy. Flow-line models [12s, 78-80, 92-94] are analytical approaches, which are capable of describing the deformation stream under given boundary conditions for a particular process. These formulations were intensively employed for rolling force and torque calculations, design of asymmetric and vertical rolling processes [78-80, 92-94]. In the FLM employed (Fig. 4.5), the detailed mathematical description of which is described elsewhere [12s], a kinematically admissible displacement velocity field fulfills the following boundary conditions: (a) the entrance and the exit velocities of a rolled sheet are even across the thickness, (b) the incompressibility condition is fulfilled at all points, (c) material's flow occurs along the prescribed streamlines, (d) at the surface, the velocity field is conditioned by means of the model parameter α, which guarantees a difference between velocities of surface and mid-thickness layers, (e) the variation of the velocity across the thickness is conditioned by the second model parameter n, f) the approximation does not allow any displacement in transverse direction.

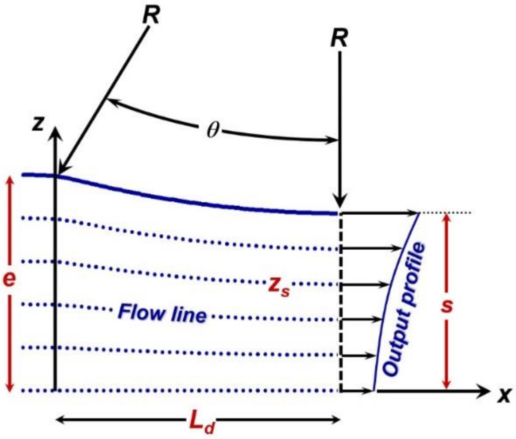

Fig. 4.5. Schematic illustration of a sheet geometry in the roll gap with the parameters of the flow-line model employed [3s].

In the FLM employed [12s], the material's flow occurs along the prescribed streamlines, determined by means of equation 4.8:

$$z_s = \phi(x,z) = z\varsigma(x) = \begin{cases} z\dfrac{1}{e}\left[1+\left(\dfrac{s}{e}+\left(1-\dfrac{s}{e}\right)\left(\dfrac{L_d-x}{L_d}\right)^{2.1}\right)^{-\Lambda}\right]^{\frac{1}{\Lambda}} & x \le L_d \\ z\dfrac{1}{e}\left[1+\left(\dfrac{s}{e}\right)^{-\Lambda}\right]^{\frac{1}{\Lambda}} & x > L_d \end{cases} \tag{4.8}$$

with the projected contact length L_d:

$$L_d = R\sin(\theta) \tag{4.9}$$

and

$$\theta = \cos^{-1}([R+s-e]/R) \tag{4.10}$$

where θ is a bite angle and R is a roll radius, e is the half-thickness of the sheet prior to rolling, s is the half-thickness of the sheet after rolling (see Fig. 4.5 for details), z_s corresponds to the position of the flow-line ($0 \le z_s \le 1$, $z_s=0$ for the mid-thickness and $z_s=1$ for the surface layer).

In this analytical approach, the value of Λ was set to 100 with the aim to ensure a continuous first and second derivate of $\varsigma(x)$ function in equation 4.8 at $x=0$. In the model developed by Decroos et al. the exponent of 2.1 (see equation 4.8) guarantees: (i) the quasi-parabolic shape of $\varsigma(x)$ in the deformation zone and (ii) continuous first and second derivative of this function when $x = L_d$. Both Λ and the exponent of 2.1 ensures various profiles for the streamlines z_s, depending on the roll gap geometry. If $z_s=0$, the deformation flow occurs along the straight streamline, while for $z_s=1$ the flow is conditioned by the roll radius.

Both the entry and the exit velocities of a rolled sheet are even across the thickness, however, the shape of the output profile (see Fig. 4.5) is controlled by two model parameters (α and n), which supposed to be positive float numbers. Within a deformation zone, the model parameter α guarantees a difference between the x-component velocity v_x of surface and mid-thickness layers. The variation of velocity across the thickness (z-component) is conditioned by the second model parameter n. As Fig. 4.6 reveals, for a given value of n, the v_x is identical for all layers with various z_s if $\alpha=0$, while the difference between the velocities along the flow-lines tends to rise when α follows upwards trend. Increasing the value of n in the FLM model, while α remains constant, tends to significantly enhance the velocity v_x of the sub-surface layers with respect to the mid-thickness planes. In the case when $\alpha>0$, the v_x of all through-thickness layers tends to converge to a single point at x corresponding to a neutral point *N*. From this point onward, the flow of the mid-layer is faster as compared to the top one. The position of the neutral point ϕ_n in rolling can be computed by the following equations [70]:

$$\phi_n = \sqrt{\frac{h_f}{R}} \tan\left(\sqrt{\frac{h_f}{R}} \frac{H_n}{2} \right) \tag{4.11}$$

$$H_n = 0.5\left(H_0 - \frac{1}{\mu} \ln\left(\frac{h_i}{h_f} \right) \right) \tag{4.12}$$

$$H_0 = 2\sqrt{\frac{R}{h_f}} \tan^{-1}\left(\sqrt{\frac{h_i - h_f}{h_f}} \right) \tag{4.13}$$

$$L_{dN} = L_d - R\phi_n, \tag{4.14}$$

where μ is a friction coefficient and L_{dN} is the *x* component of a neutral point.

Although v_x is identical for all z_s when α=0, the *z*-component of velocity (v_z) reveals significant deviations, implying that surface layers experience higher straining levels compared to the mid-thickness plane (z_s=0). It should be noted that even if α=0, the strain path of a rolled sheet is different from the plane strain compression due to displacement heterogeneities caused by various v_z across the thickness. For a given value of α, the effect of *n* on v_z seems to be negligibly small, however, the same cannot be said about the deformation patterns revealed in Fig. 4.7 (see cases for α=1.5, *n*=1.5 and α=1.5, *n*=2.5). It can be concluded from Figs. 4.6 and 4.7 that employing diverse α and *n* parameters allows reproducing a wide spectrum of deformation patterns, obtained under different thermomechanical processing conditions.

This computationally efficient model enables fast calculation of deformation velocity gradients, evolved across the thickness of a rolled sheet. If the correlation between the technological parameters (such as degree of reduction, roll diameter, material's initial thickness, and friction coefficient) and the model parameters will be determined, this two-dimensional FLM approach can enable efficient calculation of velocity gradient history, evolved across the thickness of a rolled sheet, which is needed for successful prediction of texture evolution performed by crystal plasticity models.

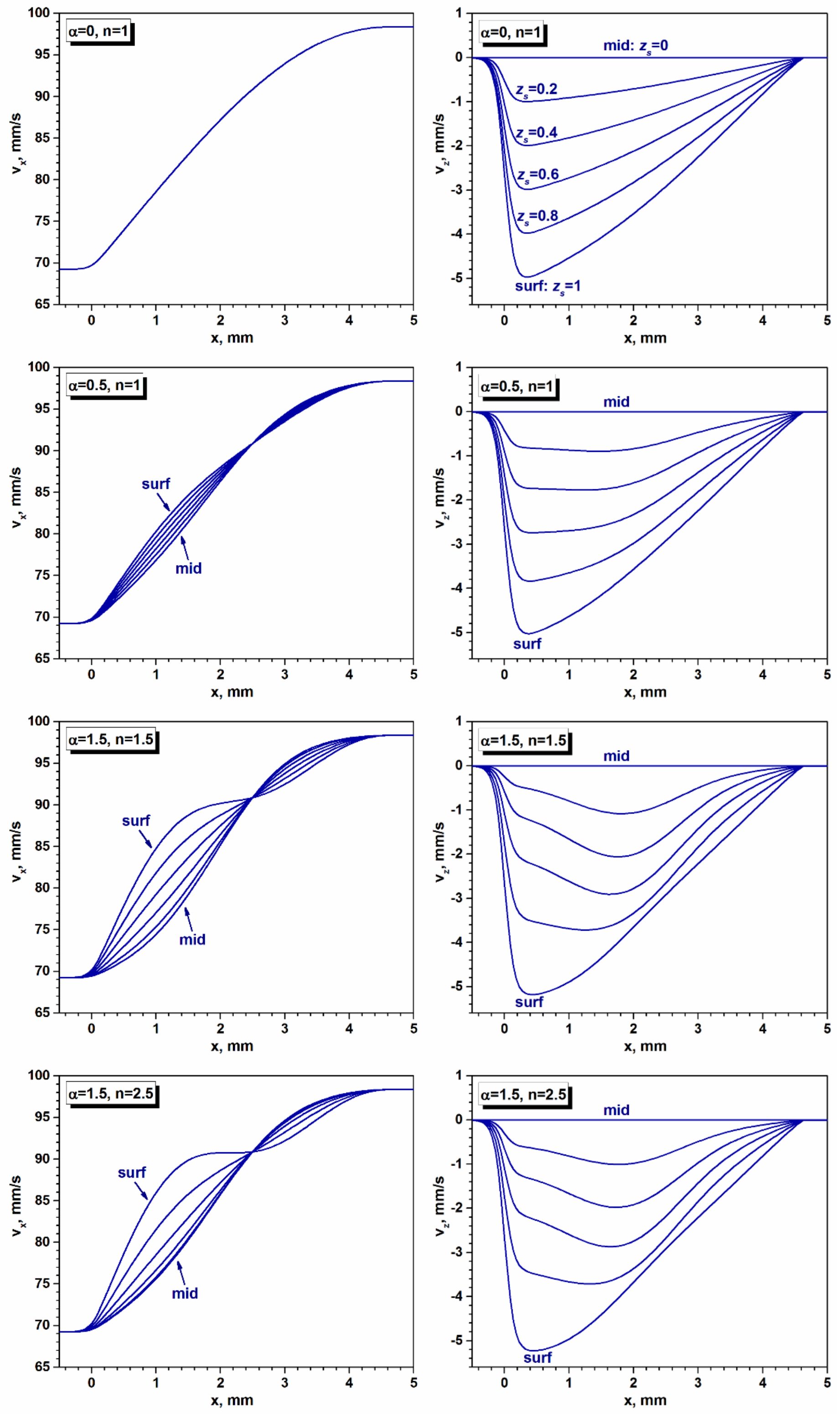

Fig. 4.6. Velocity components (v_x and v_z) calculated by the FLM employed for various model parameters along six flow-lines. The sheet of 1.125mm initial thickness was subjected to 29.6% reduction with a roll of R=64.5mm. The sequence of streamlines: z_s=1 (surface), z_s =0.8 (sub-surface 1), z_s =0.6 (sub-surface 2), z_s =0.4 (sub-surface 3), z_s =0.2 (sub-surface 4), z_s =0 (mid-plane) [3s].

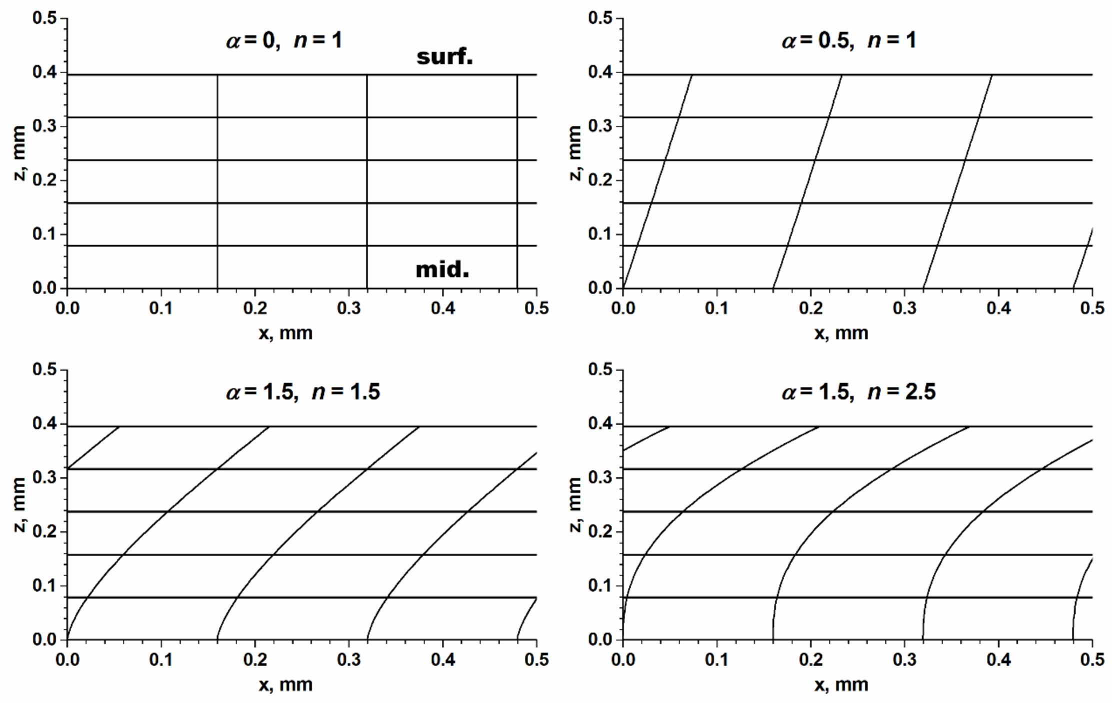

Fig. 4.7. Deformation patterns of the initially rectangular grid (half-thickness), emerged after 29.6% reduction (initial thickness = 1.125mm, R=64.5mm) as predicted by FLM for various model parameters. The sequence of streamlines: z_s=1 (surface), z_s =0.8 (sub-surface 1), z_s =0.6 (sub-surface 2), z_s =0.4 (sub-surface 3), z_s =0.2 (sub-surface 4), z_s =0 (mid-plane). In the FLM calculation, the position of a neutral point was identical for all cases, L_{dN}=2.5mm [3s].

In order to define a link between the FLM fitting parameters (α and n) and processing quantitative indicators, a series of finite element simulations were performed. Since the FLM approach does not account for anisotropy of properties, the behavior of an isotropic material was studied by FEM. In the first instance, the effect of friction on the deformation flow across the thickness of a rolled Al sheet was studied. The minimum value of friction coefficient necessary for rolling ($\mu_{\min}$) was approximated based on the roll gap geometry, as rolling of a material is not possible without an appropriate friction condition [95]:

$$\mu_{\min} = \frac{1}{2}\sqrt{\frac{h_f}{R}}\,\frac{\ln\left(\frac{h_i}{h_f}\right)+\frac{1}{4}\sqrt{\frac{h_i-h_f}{R}}}{\tan^{-1}\sqrt{\frac{h_i}{h_f}-1}} \tag{4.15}$$

In the FEM, the rolling trials were simulated with a constant Coulomb friction coefficient μ, which exceeds the value of $\mu_{\min}$ in order to avoid both convergence problems and remeshing during the calculation. As Fig. 4.8 reveals, the deformation flow is heterogeneous across the thickness even if the material is isotropic. The deformation patterns emerged in Fig. 4.8 testify that distortion of an initially rectangular grid is conditioned by the friction coefficient μ assumed. The distortion of initially orthogonal elements enables to reveal the nature of deformation process across the thickness. Both the surface and sub-surface elements (Figs. 4.8 a-d) are subjected to more severe shear distortion as compared to the mid-thickness layers. This phenomenon is revealed more explicitly while analyzing the distribution of von Mises strain e_{vM} across the thickness. Since the amount of shear is negligible in the mid-plane, the strain mode will be close to plane strain compression, while both a high value of e_{vM} (Figs. 4.8 a-d) and strongly sheared elements in the sub-surface region provide evidence for shear localization within the surface layers. It is also obvious from Figs. 4.8 a-d that the amount of shear is majorly localized in the sub-surface region and tends to decline in the direction of the mid-thickness plane independently of friction assumed, whereas increasing the value of μ tends to enhance the level of accumulated strain in the material.

In order to capture the strain gradients in rolling with reasonable accuracy, the finite element calculations were performed with the mesh containing 10 elements across the thickness (5 elements for the half-thickness). It is believed that this number of elements is capable of ensuring meaningful simulation precision. Increasing the number of elements might improve the accuracy, however, taking into account that a large number of FEM simulations had to be performed within a rational time-bounded frame, the decision was made to work with the fixed number of elements for all roll gap geometries.

While defining the flow-line model parameters, it should be stressed that in a cold rolling process, the flow of a sheet is conditioned by the roll gap geometry, straining level, and friction condition. Fig. 4.8 clearly demonstrates the effect of the friction coefficient on the through-thickness strain heterogeneity as predicted by FEM. Corresponding calculations (Fig. 4.9) were likewise performed for the identical rolling path by the FLM [12s], where each combination of α and n parameters was set as to resemble the deformation patterns of Fig. 4.8. For a meaningful comparison, first, the strain velocity gradient tensor components (L_{ij}) were calculated by both FEM and FLM [12s] and afterward the corresponding strains for the time increment Δt were calculated as $\Delta\varepsilon_{ij}=0.5(L_{ij}+L_{ji})\Delta t$. Since in two-dimensional analysis $L_{22}=L_{12}=L_{21}=L_{23}=L_{32}=0$, the von-Mises strain was calculated by means of the total accumulated strain components ε_{11} and ε_{13} as:

$$e_{vM}=\frac{2}{\sqrt{3}}\sqrt{\varepsilon_{11}^{2}+\varepsilon_{13}^{2}} \tag{4.16}$$

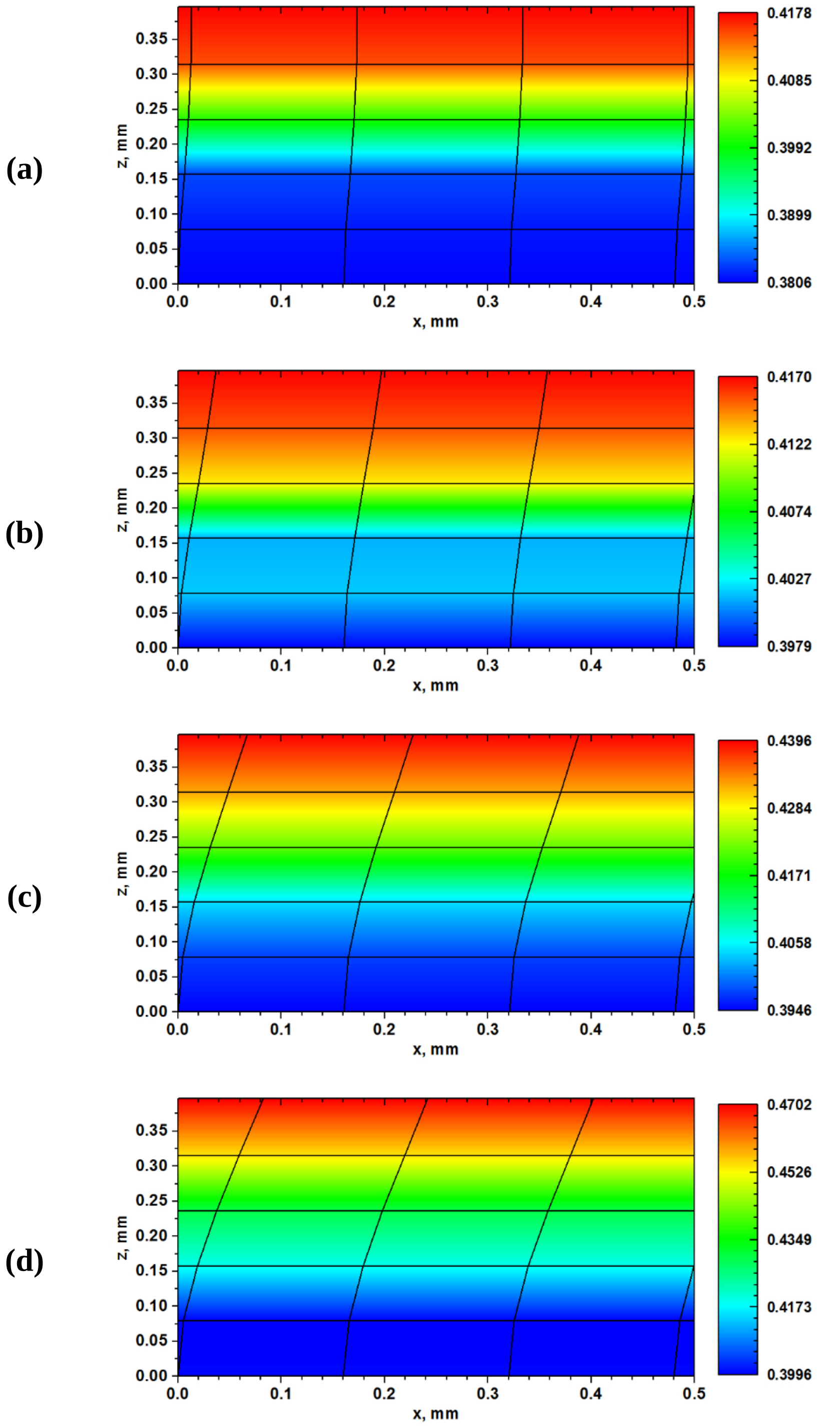

Fig. 4.8. Deformation patterns and Von Mises strain distribution across the thickness of a rolled Al sheet, subjected to 29.6% thickness reduction (initial thickness = 1.125mm, *R*=64.5mm), as predicted by finite element modeling (with Deform 2D®) for various friction coefficients: a) μ=0.05; b) μ=0.1; c) μ=0.15; d) μ=0.2. The grid was rectangular prior to deformation [3s].

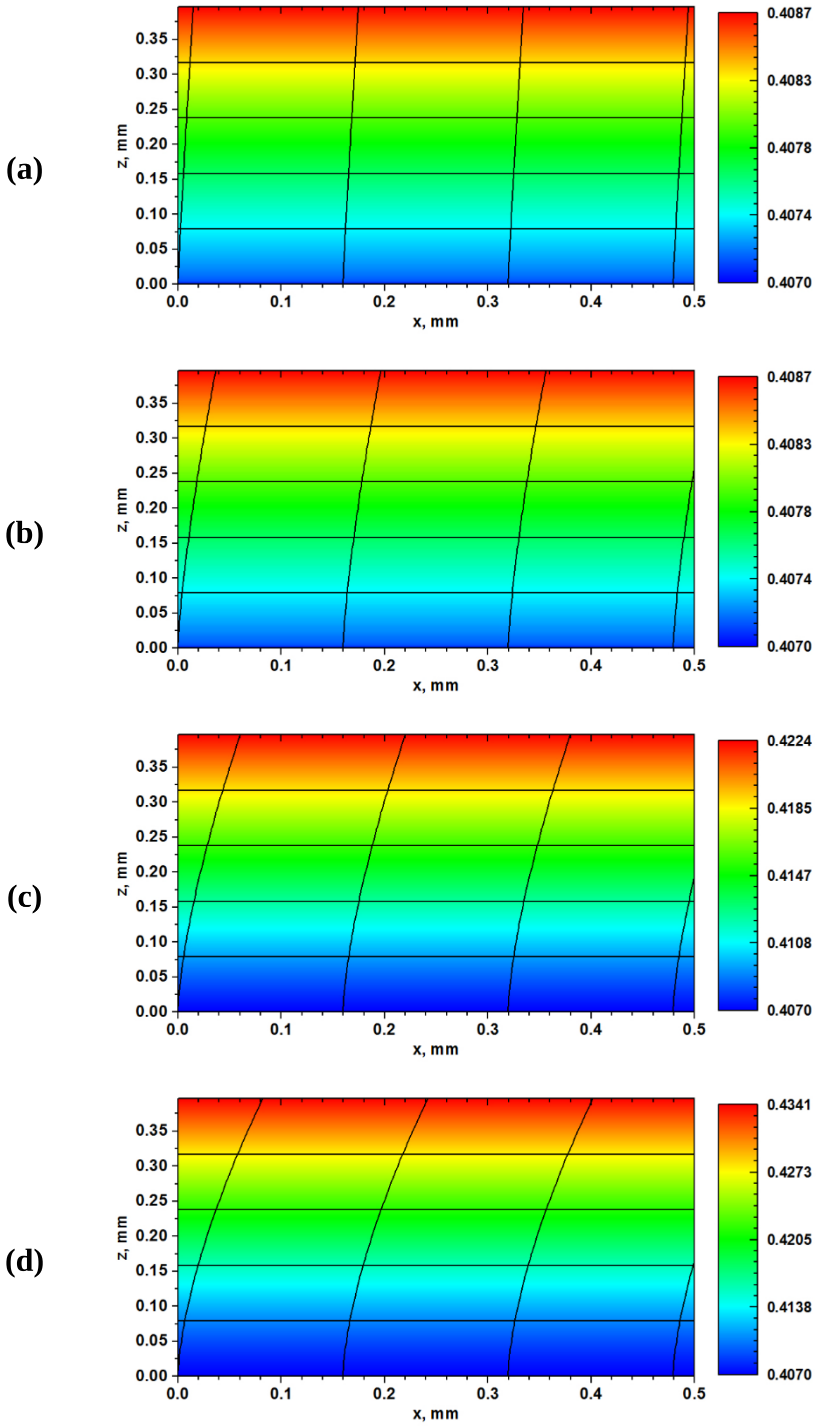

Fig. 4.9. Deformation patterns and von Mises strain distribution across the thickness of a rolled Al sheet, subjected to 29.6% thickness reduction (initial thickness = 1.125mm, R=64.5mm), as predicted by flow-line model employed [12s] with the following model parameters: a) $\alpha=6.12\times10^{-2}$, $n=1.11$; b) $\alpha=1.55\times10^{-1}$, $n=1.38$; c) $\alpha=2.69\times10^{-1}$, $n=1.52$; d) $\alpha=3.84\times10^{-1}$, $n=1.6$. The grid was rectangular prior to deformation. Each set of FLM fitting parameters ensures the best fit for the corresponding FEM output shown in Figs. 4.8 a-d [3s].

By comparing Figs. 4.8 and 4.9 it turns out that FLM is capable of reproducing both the corresponding FEM deformation patterns and strain distribution across the thickness with reasonable accuracy by employing an appropriate pair of model parameters. Figures 4.8 and 4.9 reveal meaningful qualitative agreement whereas the quantitative differences in the von Mises maps might be explained by simplifications made in the FLM model. The type of von Mises strain distribution patterns shown in Figs. 4.8 and 4.9 is characteristic for the rolling process, where the high e_{vM} values are attributed to the concentration of shear strain due to friction between the roll and the surface of a sheet.

It should be underlined here that the main advantage of the FLM-type approaches is their efficiency since the deformation history can be simulated within a fraction of a second, which cannot be done with FEM approach even if the grid is composed of a limited number of elements. The major drawback of practical implementation of the flow-line computations is the determination of α and n, which have to be fitted for each particular case. Therefore, it is of key importance to correlate the TMP quantitative indicators with the FLM model parameters by employing FEM results. In the FEM simulations, performed for a wide range of processing conditions, the coefficient of friction was varied between the μ_{min} (equation 4.15) and 0.3, which corresponds to wet and dry rolling conditions, respectively. The roll radii in FEM calculations were changed from 64.46 mm to 450 mm, which has led to a spectrum of projected contact lengths (L_d) ranging between 3.61 mm and 21.91 mm, whereas the initial thickness of the sheet subjected to cold rolling was changed between 1 and 6 mm. The following material parameters were used in FEM simulations for isotropic aluminum matrix: E = 68.9 GPa (Young’s Modulus), $\nu = 0.33$ (Poisson’s ratio) and $\sigma_y = 80$ MPa (yield stress). These boundary conditions cover the rolling trials performed with both intermediate and large draughts, which account for a variation in the contact length to mean thickness ratio (L_d/h) between 2.88 and 12.77.

After careful analysis of both FEM and FLM outputs, the following expressions were developed for the determination of α and n [3s]:

$$\alpha = A\psi + B\psi^2 + C\psi^3 + D\psi^4 + E\left(\frac{h_i - h_f}{2L}\right), \tag{4.17}$$

with

$$\psi = \mu^{f}\left(\frac{h_i}{R}\right)^{g}\left(\frac{R}{h_i - h_f}\right)^{k}\left(\frac{R}{h_f}\right)^{l}, \tag{4.18}$$

where $A=21{,}332$, $B=-2.250\times10^{2}$, $C=-1.841\times10^{2}$, $D=1.242\times10^{4}$, $E=4.833\times10^{-1}$, $f=1.833$, $g=7.892\times10^{-1}$, $k=2.293\times10^{-1}$, $l=2.283\times10^{-1}$.

$$n = M\mu^{r}\left(\frac{h_i}{R}\right)^{s} + N\mu^{t}\left(\frac{L}{L_{dN}}\right)^{u} + O\mu^{v}\left(\frac{h_i + h_f}{R}\right)^{w} + P\mu^{x}\left(\frac{L}{h_i + h_f}\right)^{y} + Q, \tag{4.19}$$

where $M=19.369$, $N=9.463$, $O=-18.606$, $P=-9.086$, $Q=3.201\times10^{-2}$, $r=9.882\times10^{-2}$, $s=5.120\times10^{-3}$, $t=-1.869\times10^{-1}$, $u=6.414\times10^{-2}$, $v=-1.045\times10^{-1}$, $w=-5.860\times10^{-3}$, $x=2.441\times10^{-1}$, $y=-1.620\times10^{-1}$.

Expressions 4.17-4.19 clearly indicate that both α and n are functions of the roll gap geometry and friction coefficient μ. Figure 4.10 reveals the distortion of the initially rectangular grid (only the vertical line is shown for each case) predicted for various roll gap geometries by the FEM and FLM employed [12s] with the model parameters calculated by equations 4.17-4.19. Analyzing the results of simulations presented in Fig. 4.10, it becomes obvious that both models predict similar distortion patterns for either extreme of the friction coefficient spectrum. By virtue of assumptions made in the FLM employed, this model is capable of reproducing the parabolic-type displacement profiles, while FEM results reveal more complex displacement shapes for certain boundary conditions (see Fig. 4.10 [3s]). This is particularly true for low values of both L_d/h and μ. For the roll gap geometries with the $L_d/h \leq 4$ and friction coefficients below 0.1, the FLM somewhat overestimates the amount of shear in the surface and slightly underestimates the shear contribution within the sub-surface layers, however, these inconsistencies tend to vanish when the value of L_d/h becomes higher than 4.

It is clear from Fig. 4.10 that the roll gap geometry has a strong impact on the evolution of deformation across the thickness. The effect of rolling conditions on the deformation distribution across the thickness can be analyzed by means of the FLM approach since the values of α and n parameters, calculated by equations 4.17-4.19, tend to resemble the FEM deformation patterns with reasonable accuracy. In the case of materials (Figs. 4.11 a and b) rolled with the thickness reduction of 29.6% and friction coefficient of 0.1, an increase of roll radius accounts for more extensive RD-ND displacement and therefore more severe shear strain evolution will evolve in both surface and subsurface regions.

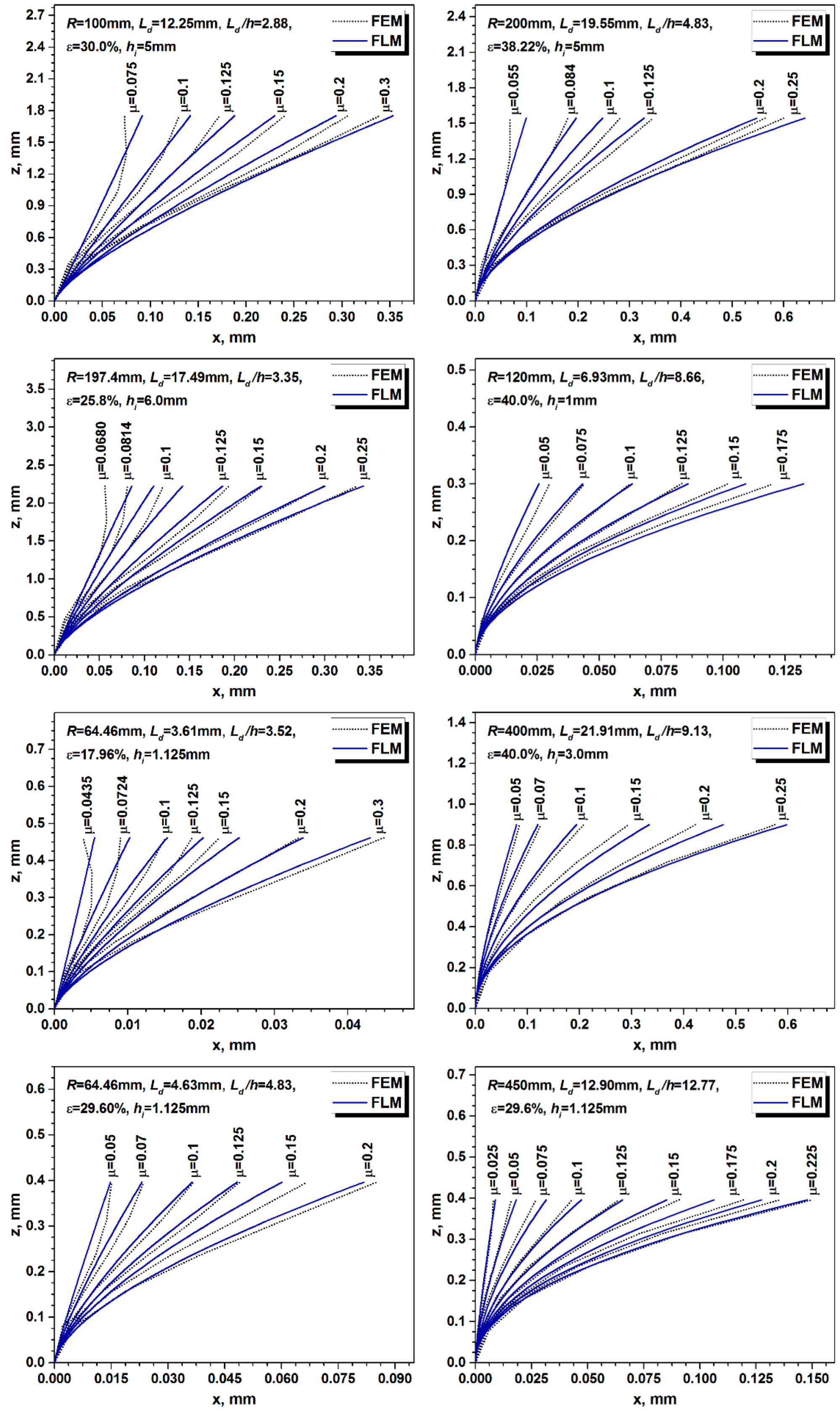

Fig. 4.10. Grid distortions predicted for various roll gap geometries [3s] by the FLM employed and FEM. The FLM model parameters were calculated by eqs. 4.17-4.19 .

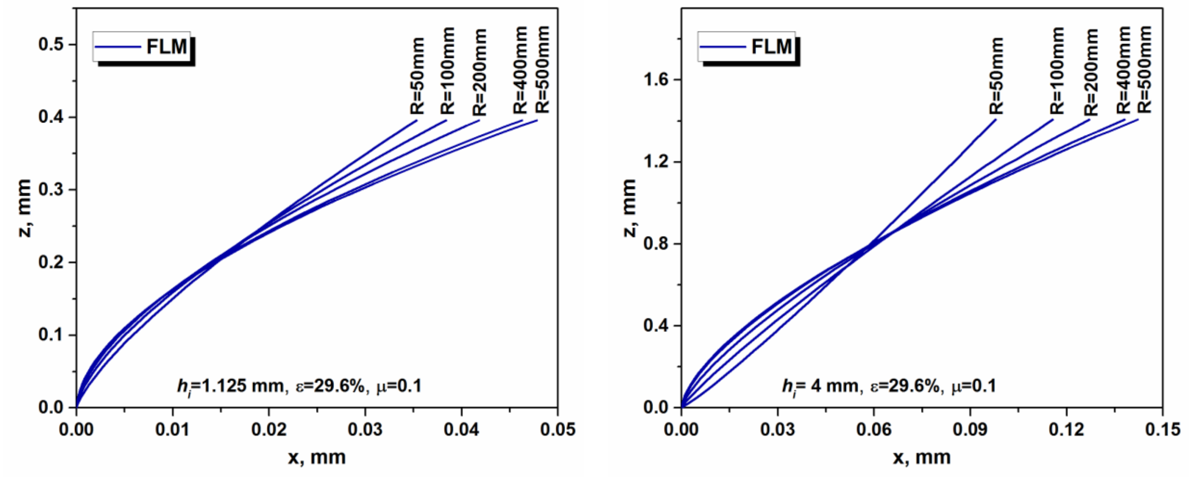

(**a**) (**b**)

Fig. 4.11. Deformation patterns predicted for identical rolling reductions and various initial thicknesses by the FLM [12s]: a) initial thickness =1.125 mm; b) initial thickness =4.0 mm [3s].

It should be underlined that the applicability of the FLM approach [12s] is not restricted exclusively to cold rolling, however, the correlation (eqs. 4.17-4.19) between the FLM model parameters and the process quantitative indicators is limited to the analysis of cold deformation trials of Al alloys. Defining both α and n by equations 4.17-4.19 excludes the effect of temperature, which might be a critical issue while simulating the behavior of materials during hot rolling.

In addition to the above-mentioned issues, there are many pros and cons regarding the implementation of analytical models, though, to make the application of FLM approaches more practically attainable, both the upper and lower bounds of implementation should be determined. This investigation majorly focuses on the Al alloys with the yield point comparable to 80 MPa, however, even in the frame of a particular series the yield stress may vary in the range of ~100 MPa. This change in the flow stress will significantly affect the stress state of materials during the rolling, which is not accounted for in the FLM [12s]. In order to determine the applicability limits of the FLM employed, the deformation flow was analyzed at the two ends of L_d/h spectrum (L_d/h=2.88 and L_d/h=12.77) in materials with σ_y=80 MPa and σ_y=200 MPa. Results of FEM simulations presented in Fig. 4.12 suggest that an increase of yield stress from 80MPa to 200 MPa triggers some varieties in the displacements across the thickness at low values of the contact length to mean thickness ratio (L_d/h =2.88), whereas this deviation tends to vanish when the rolling is performed with the large draughts (L_d/h =12.77). Analyzing

Figs. 4.10, and 4.12, it turns out that the deformation flow in materials, as predicted by both FEM and FLM simulations, is majorly controlled by the roll gap geometry and friction condition, while the hardening phenomena seem to have a smaller effect on the corresponding displacement profiles. The inconsistencies shown in Fig. 4.12 will not cause significant both qualitative and quantitative texture changes since minor strain path variations do not affect the evolution of texture drastically. This implies that the FLM [12s] can be employed for texture simulations in Al alloys from diverse series, nevertheless, it should be pointed out that, if the material properties or processing limits significantly deviate from the above-mentioned bounds, the results should be treated with particular care.

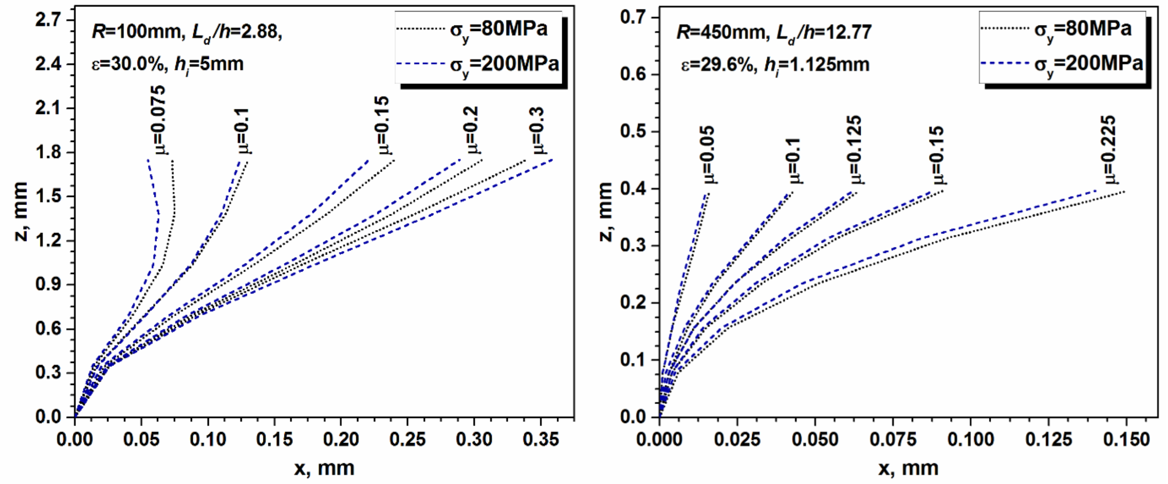

Fig. 4.12. Deformation patterns predicted by FEM for materials with various yield stresses [3s].

4.2 Symmetric rolling: experimental evidences and simulation procedures

4.2.1 Crystallographic aspect of microstructure evolution in Al alloys during symmetric rolling

Conventional rolling, also known as symmetric rolling, is widely used for flat product manufacturing. Comprehensive through-process texture control requires not only precise control of thermomechanical tuning parameters such as rolling temperature, rolling reduction, strain mode, and strain rate but also entails a detailed understanding of how the texture is affected by these process parameters. This section summarizes the crystallographic aspect of microstructure evolution in Al alloys described in detail in Refs. [2s-4s, 7s-11s, 15s, 17s, 20s, 35s].

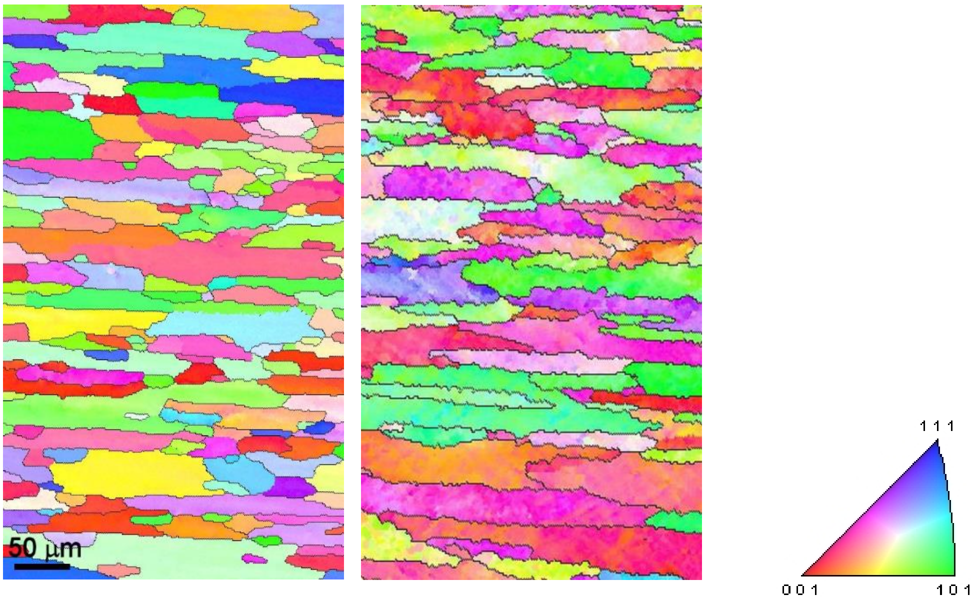

(a) (b)

Fig. 4.13. Inverse pole figure map of cold rolled 6016 Al alloy (TD-plane, the scale bar is || to RD): a) pre-rolling microstructure; b) cold rolled sheet with 20 % thickness reduction [2s].

The pre-rolling microstructure changes its morphology during cold rolling. The microstructural features of the deformed grains depend on both the material's chemistry and numerous technological parameters such as the roll configuration, strain level, friction condition, number of rolling passes e.t.c. The roll configuration and friction conditions affect the macroscopic strain mode which leads to diverse morphologies of the deformed microstructure [2s-4s, 7s-11s, 20s].

Fig. 4.13 shows recrystallized material prior to rolling and deformed microstructures after conventional cold rolling process conducted with a roll diameter of 400 mm under wet (lubricated) lubrication condition. The inverse pole figure (IPF) maps of Fig. 4.13 b reveal in-grain misorientations resulting from a heterogeneous strain distribution within particular grains dependent on the local and macroscopic strain in the rolled materials. Both the grain interaction and stress incompatibilities on the boundary of neighboring grains with different crystallographic orientations could promote in-grain stress/strain gradients leading to the observed orientation gradients. It is also obvious that the high angle grain boundaries (HAGB) are aligned with the rolling direction creating a lamellar structure irrespective of the initial grain shape.

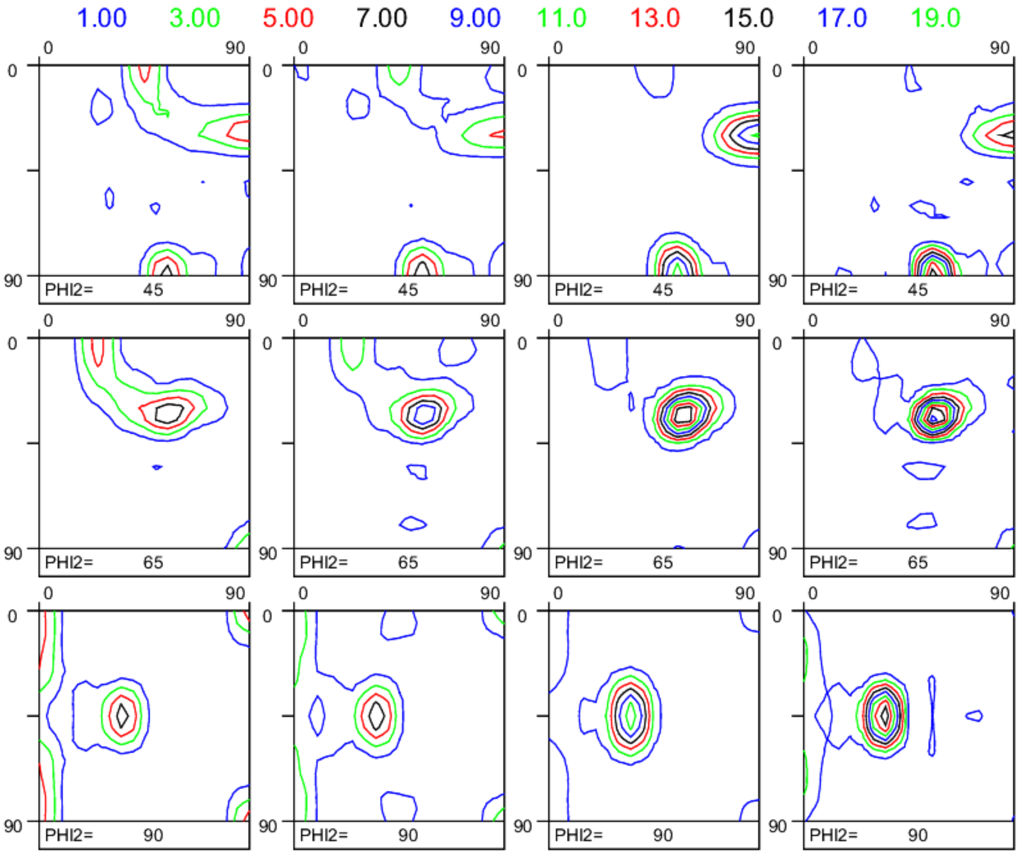

(a) (b) (c) (d)

Fig. 4.14. Texture evolution in conventionally cold rolled 6016 Al alloy: a) pre-rolling texture (hot band); b) 40 % thickness reduction; c) 83% reduction; d) 87% reduction [2s].

The thickness reduction applied in conventional cold-rolling practice might vary from 40 to 85%, depending on whether the intermediate annealing is applied or not. Typical hot-band textures transform to the β-fiber after symmetric cold rolling. The orientation distribution functions of conventionally rolled Al alloys (see Fig. 4.14) subjected to diverse reductions are represented by the same group of crystallographic orientations as material deformed by plane strain compression. The developed textures of Fig. 4.14 reveal qualitative consistency, i.e., they exhibit maxima at identical components, whilst the quantitative diversities are related to the level of reduction. Cold reduction increases the sharpness of the rolling texture components, which preexist in the hot band, but even 87% thickness reduction is not enough to completely get rid of the initial cube texture in 6016 alloy.

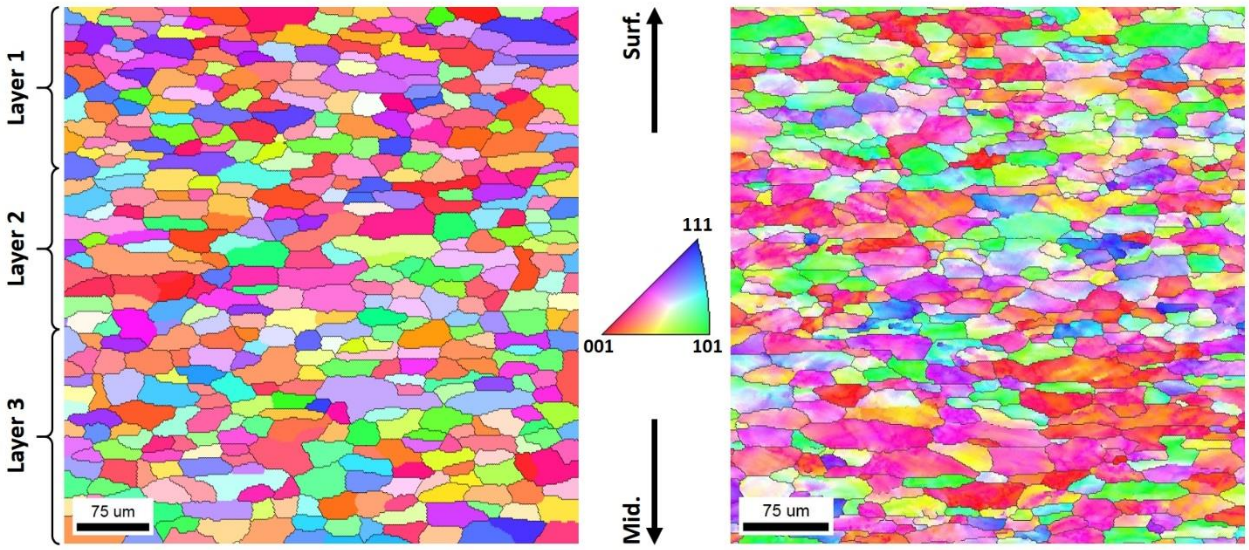

(a) (b)

Fig. 4.15. IPF maps with HAGBs of 6016 Al alloy (TD-plane, the scale bar is || to RD): a) prior to rolling; b) after 18% cold rolling reduction. The half-thickness sections are revealed [4s].

Another example of microstructure and texture evolution across the thickness prior and after rolling with a roll diameter of 129 mm is shown in Figs. 4.15 and 4.16. The fully recrystallized material of Fig.4.15a transforms to a deformed state after 18% thickness reduction (Fig.4.15b). Even such a small thickness reduction accounts for pronounced misoriented structures within each grain. The crystallographic textures of the initial and deformed materials, presented in Fig. 4.16, were calculated for three different layers, which are shown in Fig. 4.15. The first layer extends from the surface towards the 3/10 of the half-thickness, the second layer covers the area between the 3/10 and 3/5 of the half-thickness while the third layer is ranging between the 3/5 and the half-thickness of a sheet. The ODFs of Fig. 4.16 computed for layers 1-3 are qualitatively identical whereas some quantitative deviations are observed across the thickness of the investigated material. Prior to cold rolling, annealing process has ensured recrystallization texture (Fig. 4.16a), consisting of a strongly developed cube component {100}<001> as well as weak traces of Goss {110}<001> and γ-fibre <111>//ND orientations. The intensity of the cube texture gradually declines form the mid-thickness layers towards the surface and this tendency is equally observed in the deformed state, where the RX texture components tend to transform to the β-fiber.

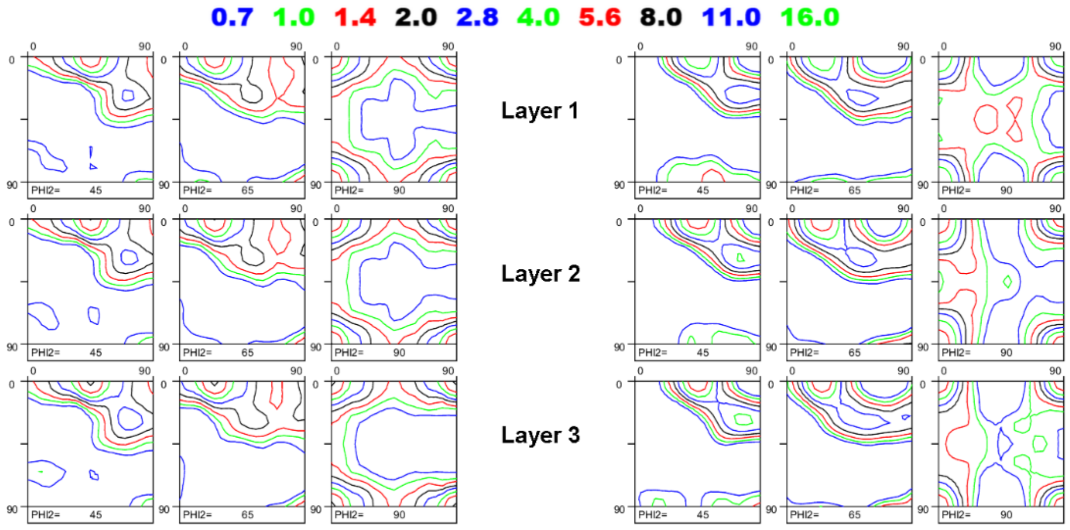

(a) (b)

Fig. 4.16. Evolution of texture across the thickness in 6016 Al alloy (TD-plane): a) pre-rolling texture; b) rolling texture after 18% thickness reduction [4s].

4.2.2 Modeling the averaged through-thickness textures

Figure 4.17 presents both the experimentally observed (after 18% rolling reduction) and simulated ODFs in 6016 Al alloy. The CP simulations were performed for six layers and afterward, the average through-thickness texture was calculated by merging individual ODFs [4s]. It is shown that during cold rolling, the RX texture evolved (Fig. 4.17a) tends to transform to the β-fiber (Fig.4.17b).

The reference components of β-fibre (Figs. 4.17 b-f) calculated by means of Eq.3.10, allow comparing the experimentally evolved deformation texture with the modeled counterparts. It is evident from Fig. 4.17b that the measured β-fibre components are slightly shifted compared to the reference orientations (bold dots on the dashed line of Fig. 4.17). In experimental ODF, a ~5° deviation is observed along the τ-fibre (⟨110⟩//TD), and this deviation persists towards the tail of the β-fibre. The β-fibre orientations of Fig.4.17b are well distinguished in the first part of the skeleton line (between the Copper {112}⟨111⟩ and {314}⟨596⟩) while towards the tail of the β-fibre (running from the {314}⟨596⟩ to Brass {101}⟨121⟩) the individual β-fibre components tend to vanish. This phenomenon is also observed on the simulated ODFs presented in Figs. 4.17 c-f.

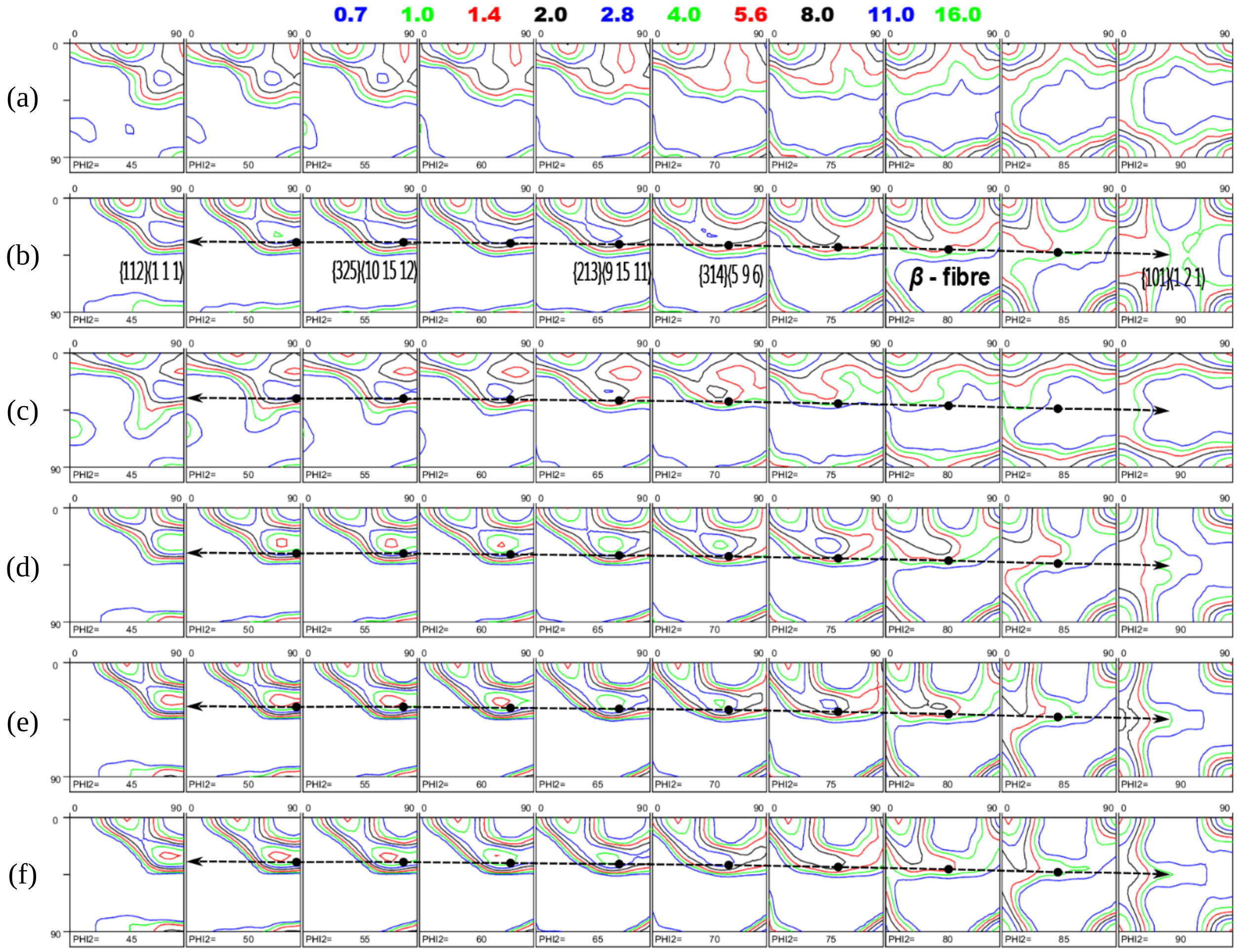

Fig. 4.17. Experimentally measured pre-rolling (a) and rolling (b) through-thickness textures (EBSD measurements cover the entire thickness of the investigated material) in 6016 Al after 18% thickness reduction. ODFs calculated with various crystal plasticity approaches by approximating rolling with plane strain compression: c) FC Taylor (ID_N =0.111); d) Alamel (ID_N =0.06); e) Cluster V (ID_N =0.116); f) VPSC (ID_N =0.102). The dashed line in figures (b-f) shows the ideal position of β-fibre components [4s].

As Fig. 4.17 suggests, an approximation of rolling by PSC provides a meaningful texture prediction, however diverse CP approaches provide qualitatively distinctive ODFs. The quality of texture prediction is assessed by means of the normalized texture index. The texture index *ID* of the difference between ODFs is calculated as follows:

$$ID = \int \left[f_1(g) - f_2(g) \right]^2 dg \tag{4.20}$$

where $f_1(g)$ and $f_2(g)$ are experimental and simulated ODFs, respectively.

The integral is taken over the entire orientation space. Lower values of *ID* correspond to better prediction and for identical textures the *ID*=0. In order to compare the results of simulations for textures of various intensities, the *ID* index is normalized with respect to the texture index (*TI*) of experimentally measured ODF:

$$TI = \int \left[f_1(g) \right]^2 dg \tag{4.21}$$

$$ID_N = \frac{ID}{TI} = \frac{\int \left[f_1(g) - f_2(g) \right]^2 dg}{\int \left[f_1(g) \right]^2 dg} \tag{4.22}$$

Results of CP simulations presented in Fig. 4.17 reveal that implementation of grain interaction phenomena improves the quality of texture prediction since the ID_N numbers for the Alamel (ID_N=0.06) and VPSC (ID_N =0.102) model are lower than one calculated for the FC Taylor approach (ID_N =0.111). Though the ID_N number calculated for Cluster V (ID_N=0.116) is slightly higher as compared to FC Taylor simulation, the Cluster V model provides qualitatively more accurate texture prediction. The Taylor model predicts weak γ-fiber components which are not observed experimentally. The major quantitative differences are observed in the first part of the β-fiber between the experimental texture and modeled ODFs. The CP approaches employed predict textures which tend to develop more intensively and, therefore, are sharper compared to the experimental one. The texture differences emerged during CP simulation might be attributed to the fact that PSC ignores the heterogeneity of deformation across the thickness.

The heterogeneity of displacement fields across the thickness of a rolled sheet is particularly accounted for in the simple geometric model expressed by equation 4.7, where the sense of balance between the geometric and friction-induced shear components is ensured by the model parameter *m*. Accoupling this simplified geometric model (eq.4.7) with different CP approaches allows revealing the nature of rolling. The effect of model parameter *m* on the quality of texture prediction is presented in Fig. 4.18. Although $m=0.25$ and $m=4$ are inversely proportional to each other, implying that $\dot{\varepsilon}_{13}$ profile computed for $m=0.25$ tent to mirror it’s counterparts calculated for $m=4$, the local strain path changes have a strong influence on the texture evolution, which is reflected by the variety of corresponding ID_N numbers (see Fig. 4.18). The

CP models implemented produce textures with ID_N minima at $m>1$, suggesting that in the current rolling trial the resulting shear $\dot{\varepsilon}_{13}$ is induced by the friction-driven L_{13} component. Since for the majority of CP approaches employed the ID_N minima are observed in the vicinity of $m\approx5$ (Fig. 4.18), Fig. 4.19 shows the simulated textures with the deformation history of Fig. 4.4, calculated by equation 4.7 with $m=5$. Comparison of ID_N numbers presented in Figs. 4.17 and 4.19 points toward the conclusion that even a simplified geometric model, which accounts for strain heterogeneities, is capable of improving the quality of texture simulation.

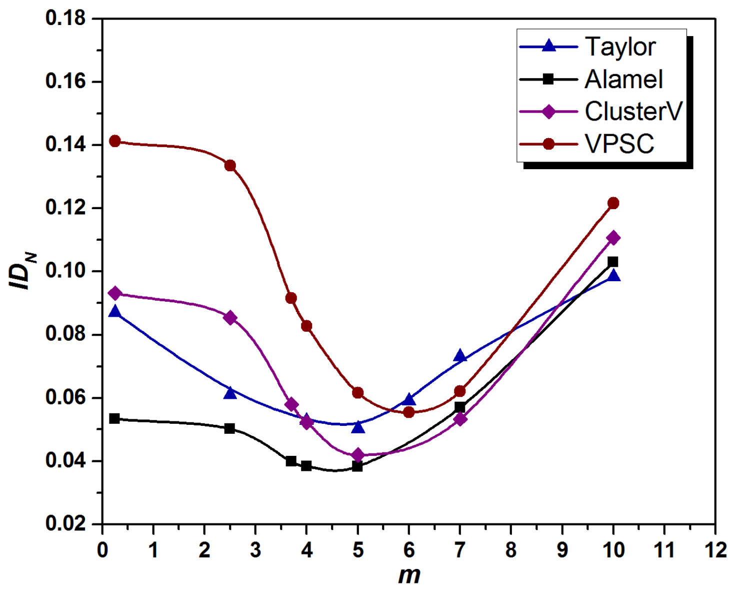

Fig. 4.18. Effect of SGM model parameter *m* (see equation 4.7 for details) on the quality of texture prediction [4s].

It is evident that since the deformation history calculated by FEM is dependent on the friction condition assumed, the corresponding texture simulation will also be. A clear example of this is seen in Fig.4.20. Feeding the strain velocity gradients, computed with FEM, to various CP models serves to produce physically sound texture simulations. Independently of the CP approach used, the simulated textures manifest lowest *IDs* for $\mu=0.0435$ (see Fig.4.20) suggesting that rolling was carried out with the friction coefficient exceeding the minimum value necessary for rolling ($\mu=1.5\mu_{\min}$). The computed ODFs corresponding to the lowest ID_N numbers are shown in Fig. 4.21, which manifests that a proper approximation of deformation history (Fig. 4.22) in combination with the grain interaction CP model gives rise to an accurate texture prediction.

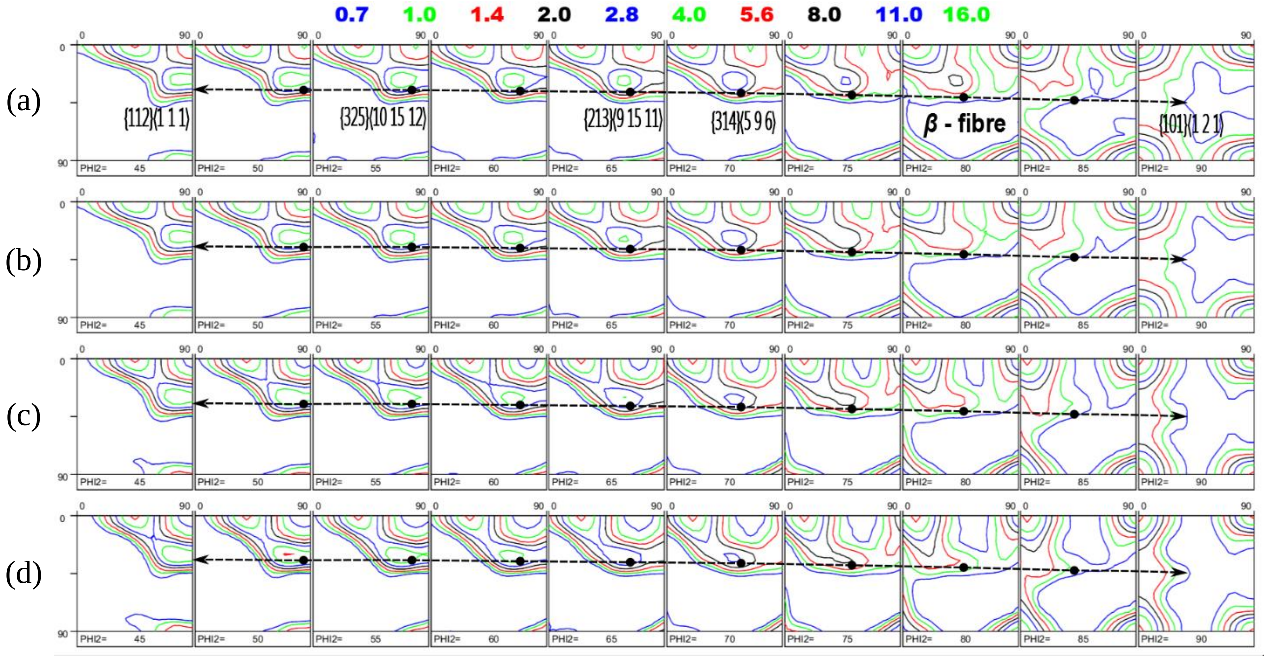

Fig. 4.19. ODFs simulated with various crystal plasticity approaches by approximating rolling with the SGM (see eq. 4.7 for details) and model parameter m=5: a) FC Taylor (ID_N=0.05); b) Alamel (ID_N=0.038); c) Cluster V (ID_N=0.042); d) VPSC (ID_N=0.062). The corresponding evolution of strain rate components are shown in Fig.4.4 [4s].

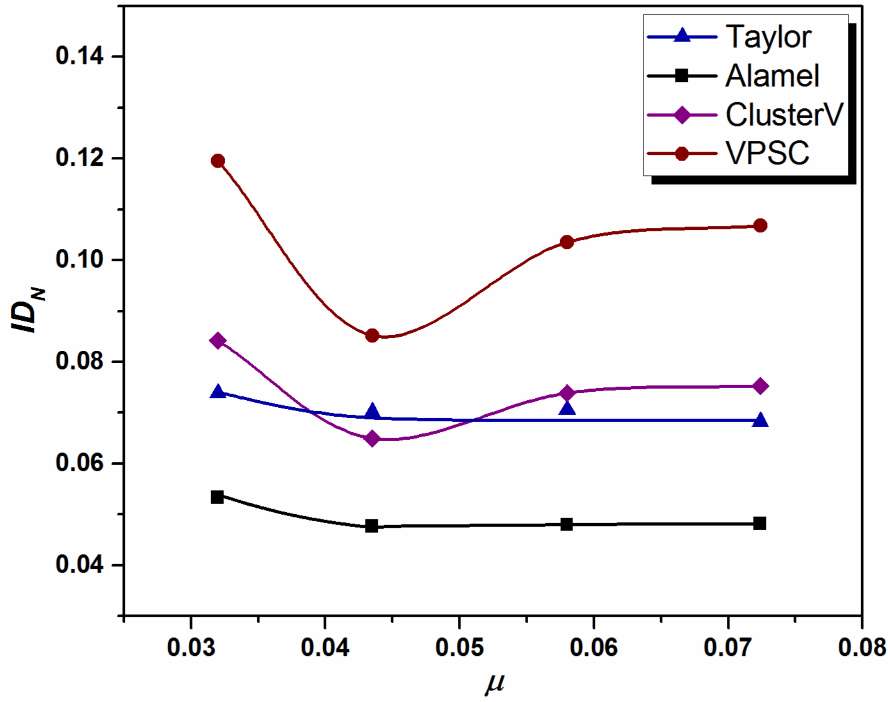

Fig. 4.20. Effect of friction condition, employed in FEM simulations, on the quality of texture prediction [4s].

Fig. 4.23 exhibits CP simulations of texture evolution by considering outputs of the FLM [12s]. The model parameters α and n, computed by means of equations 4.17-4.19, tend to produce a deformation history, comparable to one computed by FEM with μ=0.0435 (see Figs. 4.22 and 4.24). Analyzing the ID_N numbers obtained (see Fig. 4.23), it turned out that this computationally efficient approach combined with a particular CP model is capable of providing texture prediction nearly equal to one simulated with the deformation history obtained from the finite element model (see Figs. 4.21 and 4.23).

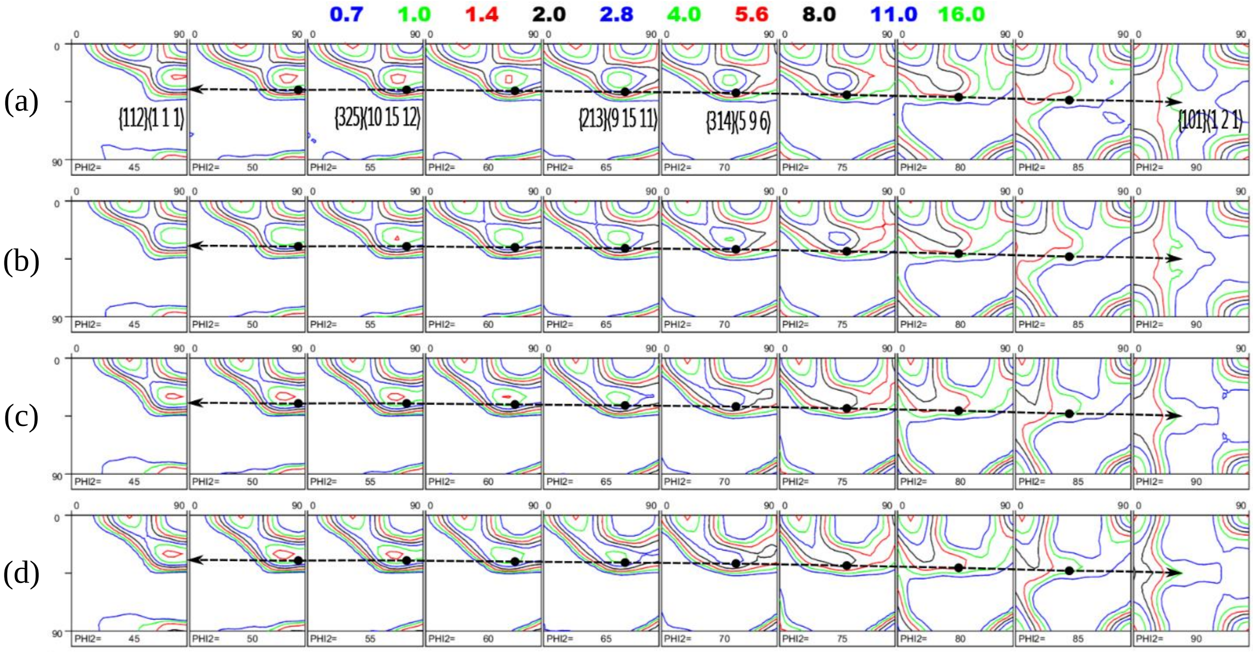

Fig. 4.21. Simulated deformation textures by diverse CP models and strain velocity gradients computed by FEM with μ=0.0435: a) FC Taylor (ID_N=0.07); b) Alamel (ID_N=0.048); c) Cluster V (ID_N=0.065); d) VPSC (ID_N=0.085) [4s].

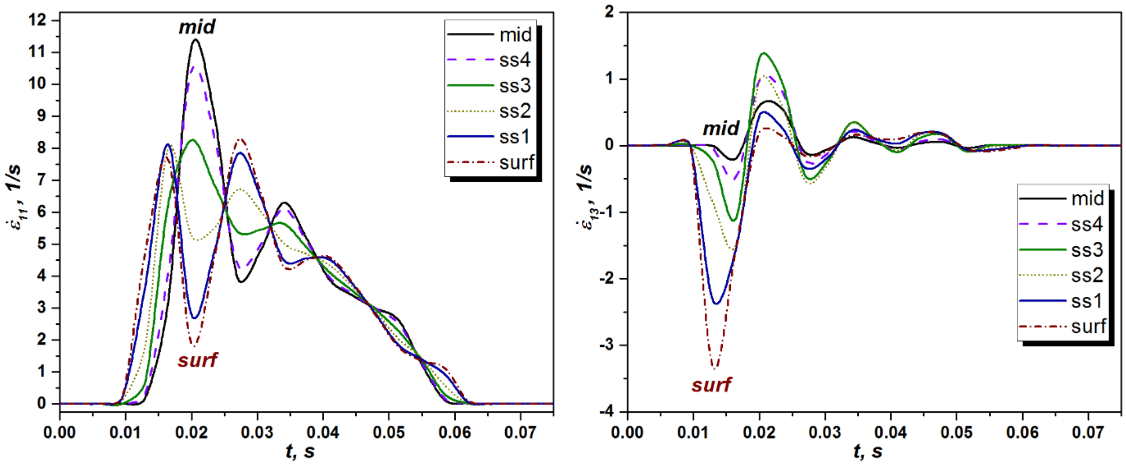

Fig. 4.22. Evolution of strain rate components with time across the thickness of a rolled sheet calculated with FEM for: roll diameter of 129 mm, thickness reduction 18% and μ=0.0435. On the graphs, surf: s=1; ss1: s=0.8; ss2: s=0.6; ss3: s=0.4; ss4: s=0.2; mid: s=0 [4s].

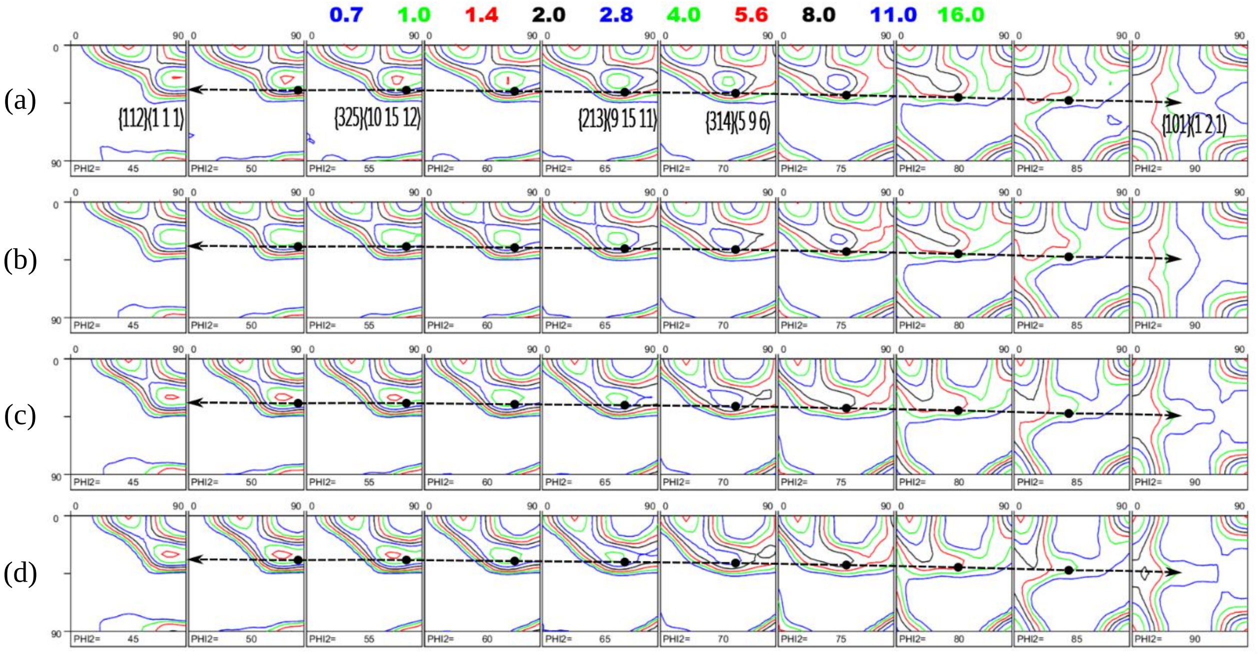

Fig. 4.23. CP simulations of texture evolution in 6016 Al alloy after 18% reduction by considering strain velocity gradients computed by FLM (see Fig.4.24): a) FC Taylor (*ID*=0.069); b) Alamel (ID_N=0.041); c) Cluster V (ID_N=0.064); d) VPSC (ID_N=0.088) [4s].

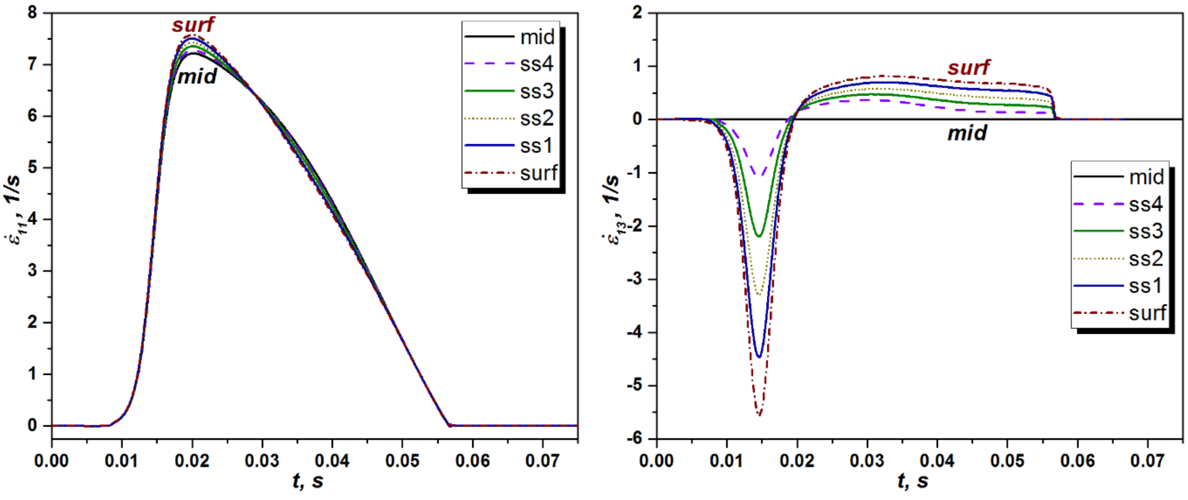

Fig. 4.24. Evolution of strain rates with time across the thickness of a rolled sheet calculated by flow-line model [12s] with α and *n* (computed by means of eqs. 4.17-4.19) for: roll diameter of 129 mm and 18% thickness reduction [4s].

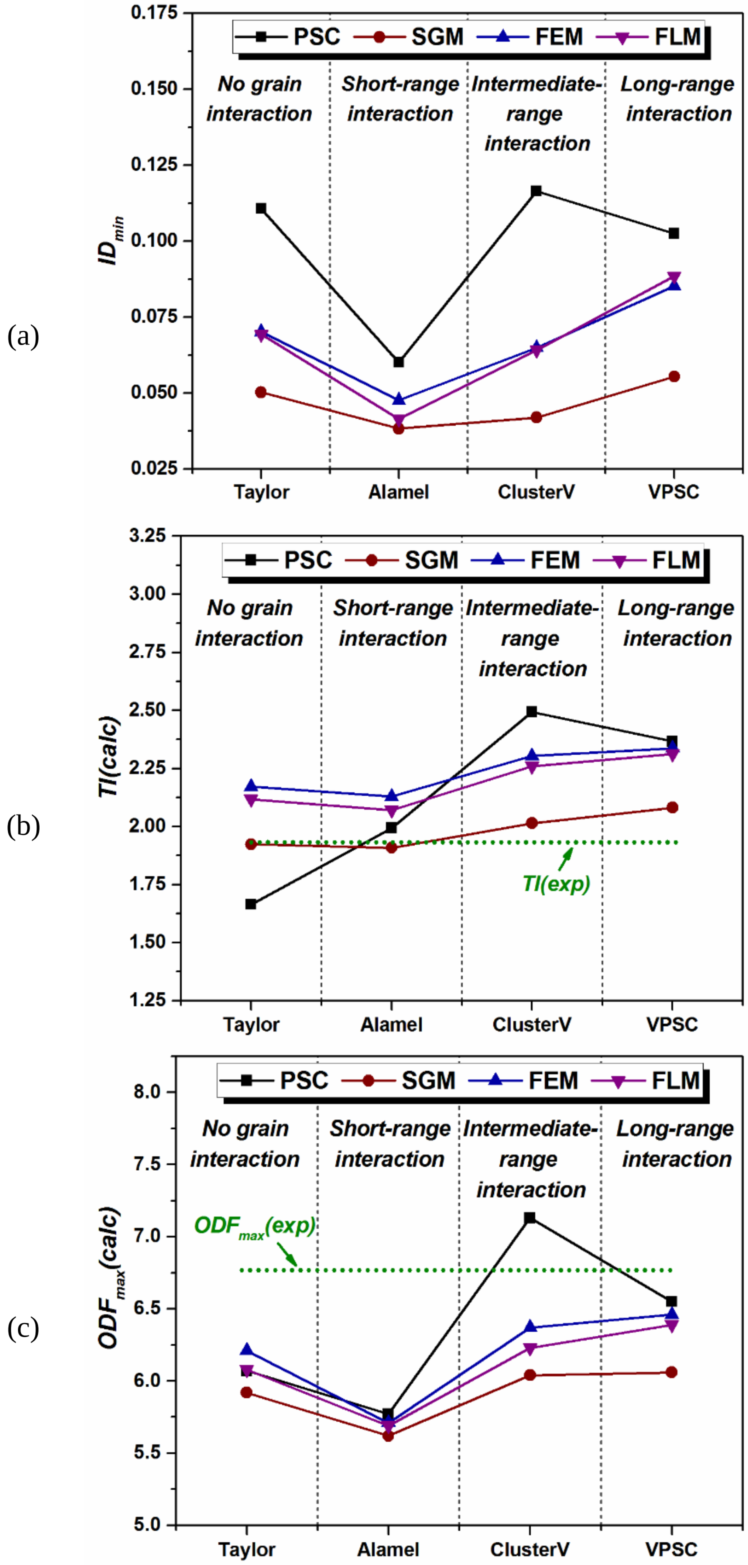

Fig. 4.25. Variation of the quality of texture prediction with the strain mode approximation and grain interaction schemes, employed by the corresponding CP model. Texture quantitative indicators: a) texture index difference, ID_{min} (the model parameters in eq. 4.7, FEM and FLM were set as to ensure the lowest ID_N number for a given CP simulation); b) texture index TI; c) ODF maximum value, ODF_{max} [4s].

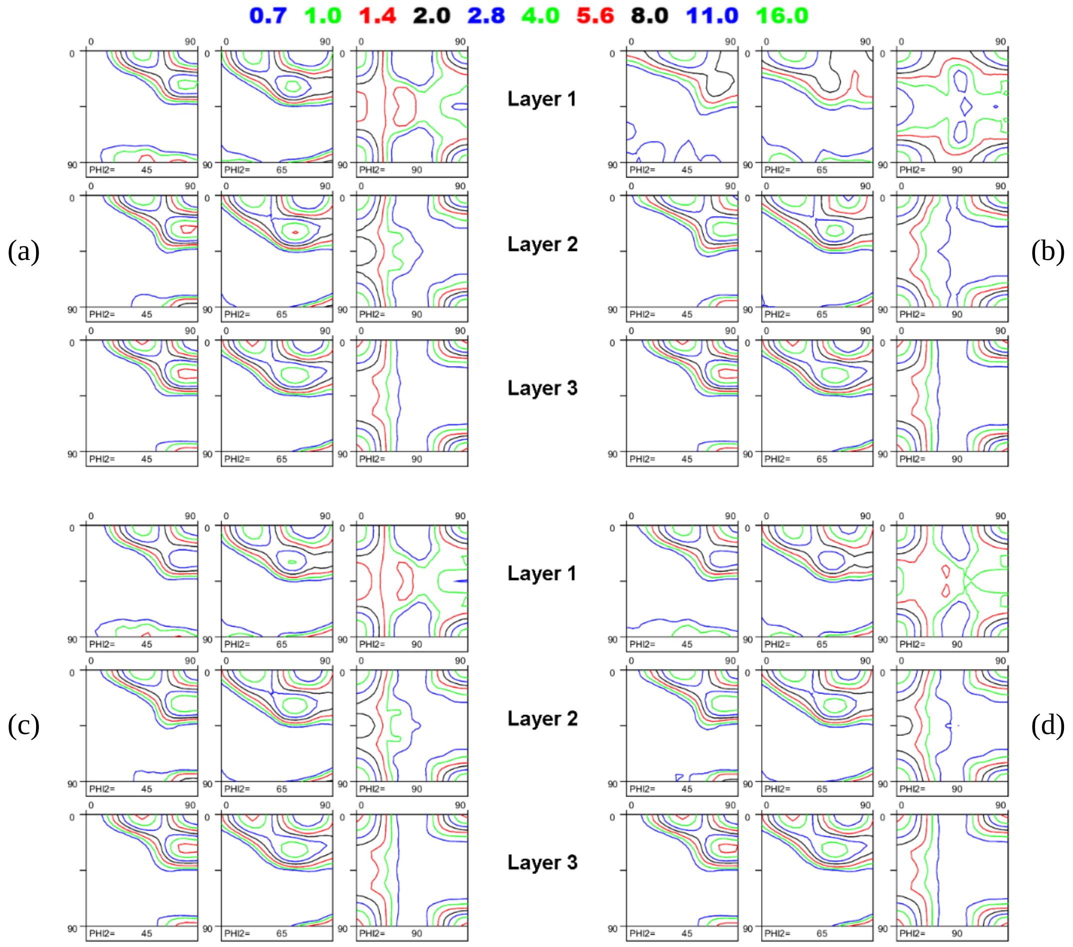

Fig. 4.26. Through-thickness textures simulated with the Alamel model for 6016 Al alloy shown in Fig. 4.15 (the experimental ODF is presented in Fig. 4.16): a) the strain velocity gradient is approximated by PSC; b) the *L* is calculated by SGM with *m*=5; c) the *L* is computed by FEM with μ=0.0435; c) the *L* is computed by FLM with α and *n*, approximated by equations 4.17-4.19 [4s].

4.2.3 Modeling the texture heterogeneities across the thickness

Both qualitative and quantitative through-thickness texture varieties, observed in the initial material of Fig.4.16 a, can be attributed to the heterogeneity of the deformation flow across the thickness during hot and cold rolling processes. As a result, the subsequent annealing texture is likewise heterogeneous [4s]. Even after relatively small rolling reduction (18%), the deformation textures observed in various thickness layers (Fig. 4.16 b) reveal noticeable quantitative and minor qualitative diversity. This is attributed to (i) unequal deformation flow across the thickness (see Fig. 4.22) and (ii) heterogeneous pre-rolling texture (Fig. 4.16 a). The same evolutionary pattern of texture heterogeneity was observed in 6016 Al alloy subjected to 30% rolling reduction [3s]. Since the Alamel model provides the lowest ID_N numbers and texture indexes, which are closest to the experimental one, for most strain mode approximations employed (see Fig. 4.25), Fig.4.26 reveals the texture evolution simulated with this CP theory and displacement fields computed by various approaches. An increase of intensity of the cube component from the surface towards the mid-thickness plane is computed with reasonable accuracy, independently of the strain velocity gradient used (see Figs. 4.16 b and 4.26 a-d). Regarding the individual β-fiber components, it is obvious that the intensities of the Copper and {213}⟨9 15 11⟩ orientation are captured quite well whereas the simulated evolution of the {101}⟨121⟩ orientation across the thickness is less accurate.

4.2.4 Remarks on texture modeling

In addition to published results [72-77, 87-91], the current crystal plasticity calculations (explained in great detail in [3s, 4s]) show how the accuracy of texture prediction is affected by the approximation of strain mode and grain interaction phenomena, employed by the corresponding CP model. Analyzing the results of texture simulations presented in Figs. 4.17, 4.19, 4.21, and 4.23 it can be noticed that independently of the technique employed for computation of strain history (PSC, SGM, FLM or FEM), implementation of Taylor model for texture simulation provides a qualitatively reasonable prediction. The full constraints approach produces sharper textures with respect to the experimental counterpart of Fig. 4.17b, since in this model each crystal (grain) tends to deform independently, neglecting any kind of interaction, whereas this scenario does not seem to be actual in real materials. This might explain why the textures modeled by CP approaches, considering either short or intermediate-range grain interaction phenomena (Alamel and Cluster V), reveal better quantitative characteristics compared to ones computed with the Taylor theory (Fig. 4.25). In the current case, the employed long-range grain interaction (VPSC) seems to be less successful in term of ID_{min} numbers as compared to the Cluster V or Alamel (see Fig. 4.25 a), however, the texture indexes *TI* (see Fig.4.25 b), calculated for a particular CP model and diverse strain modes (SGM, FEM or FLM), do not reveal substantial differences. Furthermore, the ODF maximum values are better captured by the VPSC and Cluster V (see Fig.4.25 c), compared to Alamel predictions. It should also be mentioned here that both VPSC and Cluster V models are capable of accurate texture prediction in the case of the larger straining levels [7s], where the application of these grain interaction CP approaches assures *ID* numbers nearly identical to the Alamel model (see Fig. 4.27).

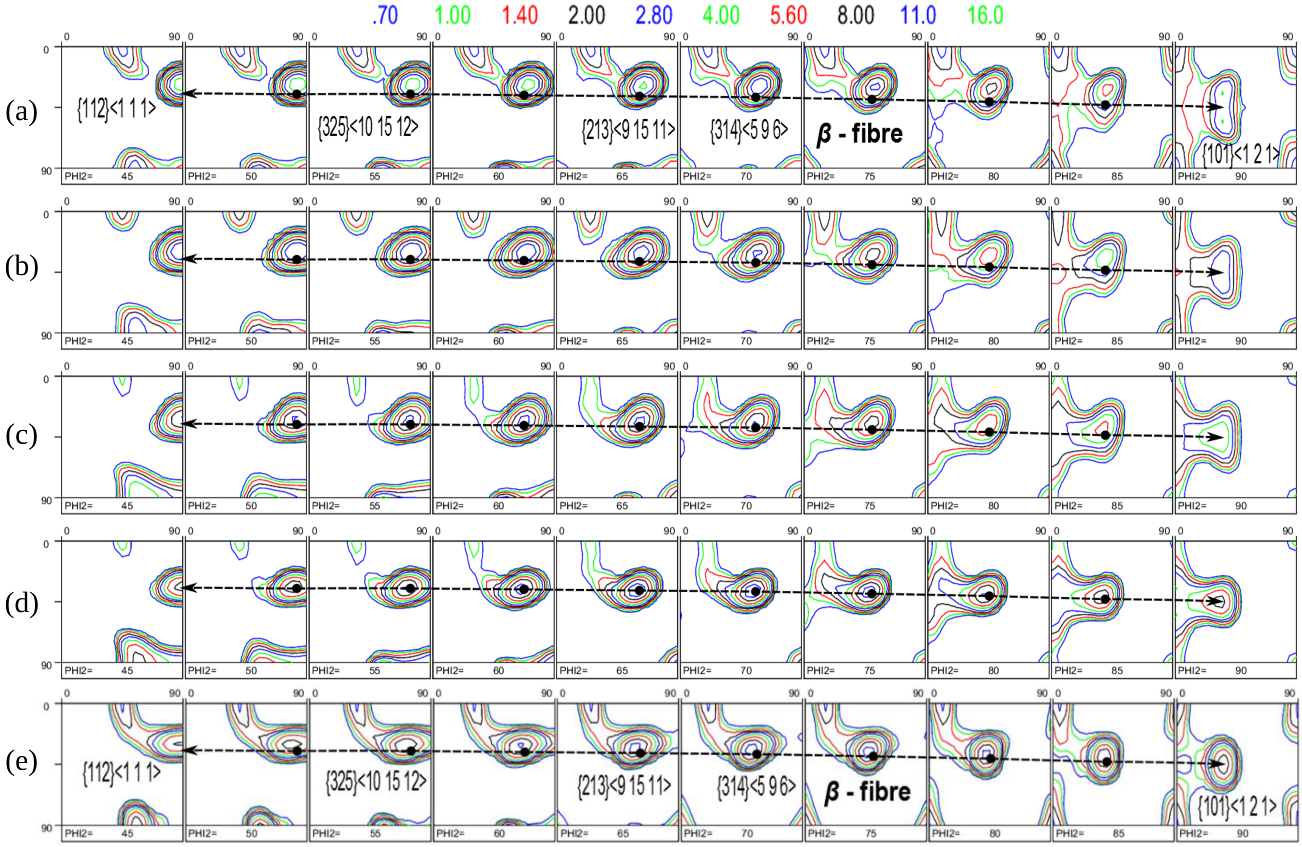

Fig. 4.27. Calculated deformation textures in 6016 Al alloy after 86% multi-pass rolling: a) texture simulated with the FC Taylor model, ID_N=0.49; b) texture simulated with the Alamel model, ID_N=0.26; c) texture simulated with the Cluster V model, ID_N=0.21; d) texture simulated with the VPSC model, ID_N=0.24; e) experimentally observed ODF. The deformation history for 12 consequent passes was computed by FEM [7s].

As it is shown in Fig. 4.27 [7s], the cluster V model with an intermediate range of grain interaction produces a somewhat stronger Brass component, compared to the Alamel model, whereas the ID_N number (ID_N= 0.21) is comparable with the ones calculated for the Alamel and VPSC approaches. Texture calculation carried out with the VPSC model, which employs a long-range grain interaction, closely resembles the Cluster V simulation. Identically to the employed grain interaction models, the ID_N number produced with the VPSC approach tends to drop significantly compared to the full constrained Taylor theory (see Fig. 4.28).

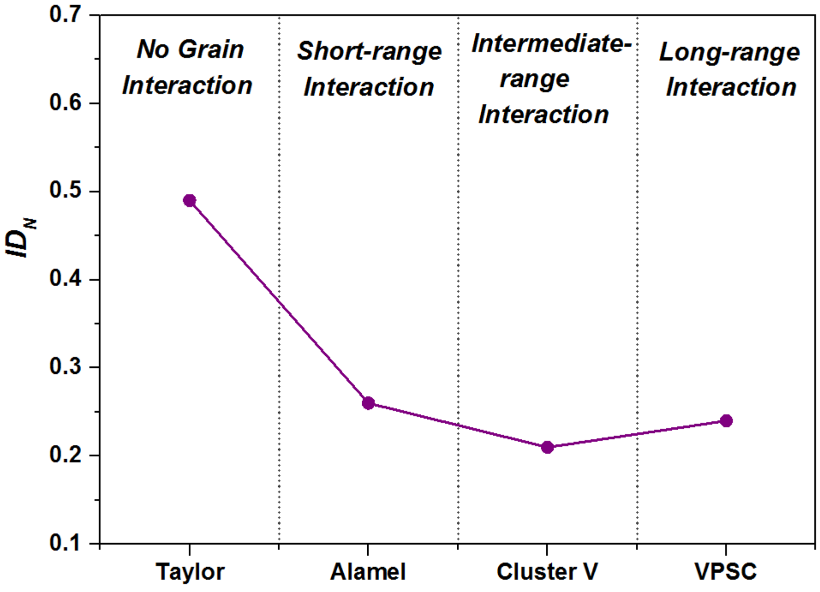

Fig. 4.28. Effect of grain interaction scheme, employed by the corresponding CP model, on the quality of texture prediction, performed for 86% multi-pass rolling [7s].

Even though FLM neglects the strain hardening phenomena while materials experience hardening during deformation in FEM, the result of CP simulations performed with both FEM and FLM outputs reveal minor differences (Figs. 4.21 and 4.23). This implies that strain hardening parameters have a slight effect on the quality of texture prediction. Furthermore, approximating the rolling process with simplified geometric models equally provides a reasonable estimate of overall texture evolution. Although Taylor type homogenization models employ strain hardening, varying the values of hardening model parameters for metallic systems, in which the deformation is governed by a single-mode (such a slip), has a negligible effect on the quality of texture prediction.

Summarizing the effect of grain interaction schemes on the quality of texture prediction (see Figs. 4.25 and 4.28), it becomes obvious that more accurate texture simulations should be tilted towards (i) implementation of strain heterogeneity, involved in the deformation process, and (ii) considering a particular grain interaction scheme for moderate and high straining levels.

While Fig. 4.25 suggests that the most accurate overall texture simulation might be carried out by employing a simple geometric approach (eq. 4.7), the same cannot be said about the accuracy of texture calculations across the thickness of a material. Comparing both the experimentally observed and simulated through-thickness textures (Figs. 4.16 b and 4.26), it becomes obvious that the geometric approach is not capable of capturing the texture evolution across the thickness with a high degree of accuracy. The largest discrepancy between the modeled and measured ODFs is observed in the surface layer (Layer 1), where the simulated evolution of brass and copper components deviates from the experimentally observed counterparts.

The modeled textures of Figs. 4.17, 4.19, 4.21, and 4.23 with CP approaches, which employ various grain interaction schemes, reveal comparable evolutionary patterns. Though a short-range grain interaction of the Alamel model ensures the most accurate global/average through-thickness texture prediction (Fig. 4.25), nevertheless, the importance of interaction mechanisms on other mesoscopic scales such as the intermediate or long-range cannot be neglected. Domination of a particular interaction scheme over the other ones might be determined by carrying out texture simulations for a wide spectrum of straining levels. Further analysis of the lowest ID_N numbers, obtained for various boundary conditions (Fig. 4.25), suggests that considering strain heterogeneities across the thickness plays an important role in CP simulations. Although the qualitative characteristics of texture simulations tend to improve by application of both geometrical approach, based on eq. 4.7, and the FLM [12s], the main drawback of their practical implementation is the determination of model parameters. It should be mentioned that the fitting parameters of the SGM and FLM reveal a clear correlation with both the roll gap geometry and friction coefficient. The model parameter m in the SGM, described by eq. 4.7, allows revealing the nature of deformation for a given roll gap geometry. Results of FEM calculations claim that in rolling trial with 18% thickness reduction, first the roll gap geometry-induced shear component dominates over the friction-induced counterpart, whereas afterward this process reveals an opposite tendency (see Fig. 4.22). This phenomenon can be reproduced to a certain extent with the simple geometric approach employed (eq. 4.7). Fig. 4.18 suggests that the most accurate CP calculations with the SGM outputs are ensured by assuming $3.5<m<6$, pointing towards the strain history qualitatively comparable with the one computed by FEM (see Figs.4.18 and 4.22). In rolling trials with relatively high friction coefficient (dry, warm or hot rolling), first, the friction-induced shear will dominate over the roll gap geometry-induced component and afterward this tendency will be reversed. In this case, it is reasonable to set m below 1, since the higher μ is expected to be more rationally reproduced by the smaller m value. The approximate value of m might be computed as:

$$m = \frac{1}{5\mu} \tag{4.23}$$

For wet rolling (using various lubricants, which decrease the friction between the roll cylinder and the surface of a sheet), it is reasonable to assume that the process is performed with μ, which slightly exceeds the friction coefficient (μ_{min}), which is necessary for rolling. In this case, the m might be calculated by a more accurate quantitative correlation between the m and $\mu_{\min}$:

$$m = \frac{1}{2\pi\mu_{\min}} \quad (4.24)$$

where μ_{min} is defined by equation 4.15.

As to model parameters α and n in the FLM employed, it was pointed out by Decroos et al. [12s], that a link between the model parameters and the μ, could be determined by correlating both the FEM and FLM deformation patterns. As the starting point of a first approximation, the rough value of μ for wet rolling might be computed by equation 4.15, whereas Fig. 4.20 suggests that the ID_{min}, ensuring the most accurate texture simulation, converges at μ slightly exceeding the minimum value of μ necessary for rolling. Once the value of friction coefficient is estimated, the FLM model parameters α and n can be determined for a given rolling trial by equations 4.17-4.19 [3s], enabling fast and efficient texture simulations.

4.3 Asymmetric rolling

In conventional rolling, the deformation mode is symmetric with respect to a mid-thickness plane. The asymmetry in the rolling gap could be induced by various factors which are summarized in Table 4.1. The ASR process could be subdivided into two groups: unidirectional and reverse methods. In the unidirectional ASR processes, the difference in friction conditions or circumferential velocity between the upper and lower rolls produces an extensive shear deformation [18s, 20s, 36-49] which is not typical for conventional rolling. The reverse ASR process causes a drastic change of the strain path as the direction of shear is reversed either by reversing the rolling direction or rotating the sheet by 180° around the transverse direction. This section summarizes the research activities presented in Refs. [2s, 16s, 18s, 20s, 21s, 30s, 33s, 34s].

Table 4.1. Methods inducing asymmetry during rolling. In the table: R_1, R_2, ω_1, ω_2 are radii and angular velocities of top and bottom rolls, respectively. μ_1 and μ_2 are the friction coefficients between the sheet and the top and bottom rolls, respectively [2s].

Unidirectional rolling				**Type of rolling**	**Reason for asymmetry**
1	$R_1=R_2$	$\omega_1=\omega_2$	$\mu_1=\mu_2$	SR	-
2	$R_1>R_2$	$\omega_1=\omega_2$	$\mu_1=\mu_2$	ASR	Difference in circumferential velocities of top and bottom rolls
3	$R_1=R_2$	$\omega_1>\omega_2$	$\mu_1=\mu_2$	ASR	
4	$R_1=R_2$	$\omega_1=\omega_2$	$\mu_1>\mu_2$	ASR	Different friction conditions
5	$R_1>R_2$	$\omega_1=\omega_2$	$\mu_1>\mu_2$	ASR	Different roll diameters and various friction conditions
6	$R_1=R_2$	ω_2 *is free*	$\mu_1=\mu_2$	ASR	Idol roll
7	$R_1>R_2$	ω_2 *is free*	$\mu_1=\mu_2$	ASR	Idol roll and different roll diameters
8	$R_1=R_2$	$V_1=V_2$	$\mu_1=\mu_2$	ASR	Rolling with dead block. The material of the dead block is hard to deform.
Reverse Asymmetric Rolling					
1	Single-side ASR (The rolling direction is reversed after each pass by rotating the rolled sheet by 180° around normal direction.)				Processes 2-8 are applicable to reverse ASR
2	Double-side ASR (The top and bottom sides are reversed after each pass, i.e. the rolled sheet is rotated by 180° around transverse direction)				

Asymmetric rolling (ASR), in which the circumferential velocities or diameters of working rolls are different, imposes shear deformation and in turn shear deformation textures to the deforming sheets [2s, 16s, 18s, 20s, 21s, 36-46]. The typical shear texture for FCC alloys is a 45° rotated cube orientation combined with a {111}//ND fibre texture which is known to improve the plastic strain ratios of aluminum. The deformation process of sheets under asymmetric rolling conditions can be approximated by a two-dimensional strain state of compressive strain along the normal direction (ε_{zz} and $\varepsilon_{zz}=-\varepsilon_{xx}$) together with simple shear strain along the rolling direction (ε_{xz}). More detailed information on the ASR process, induced by various roll diameters could be found in Refs. [2s, 16s, 18s, 20s, 21s].

The IPF maps of Fig. 4.29 [2s] reveal microstructural changes involved in ASR process. Unlike the conventional rolling, which is to a large extent characterized by a monotonic strain path, the strain mode in the asymmetric rolling is complex and can be decomposed in various simple strain modes. In asymmetric rolling process, the combination of compressive strain along the normal direction and shear strain parallel to the rolling direction results in the rotation of high angle grain boundaries around the transverse direction as it is shown in Fig. 4.29. The appearance of sheared grains in the asymmetrically rolled sheet can be attributed both to the specific strain mode and the high friction between the rolls and the sheet surface.

The crystal plasticity models work quite satisfactorily for monotonic strain modes such as plane strain compression, which is often used as an approximation for conventional cold rolling. However, in the case of asymmetric rolling, an extensive shear strain is imposed on the deforming sheet in addition to the compression strain component. Different roll diameter ratios account for various strain modes that have a great impact on texture development because the texture evolution is strongly dependent on the precise combination of plane strain compression and shear strain which could be obtained in the ASR process.

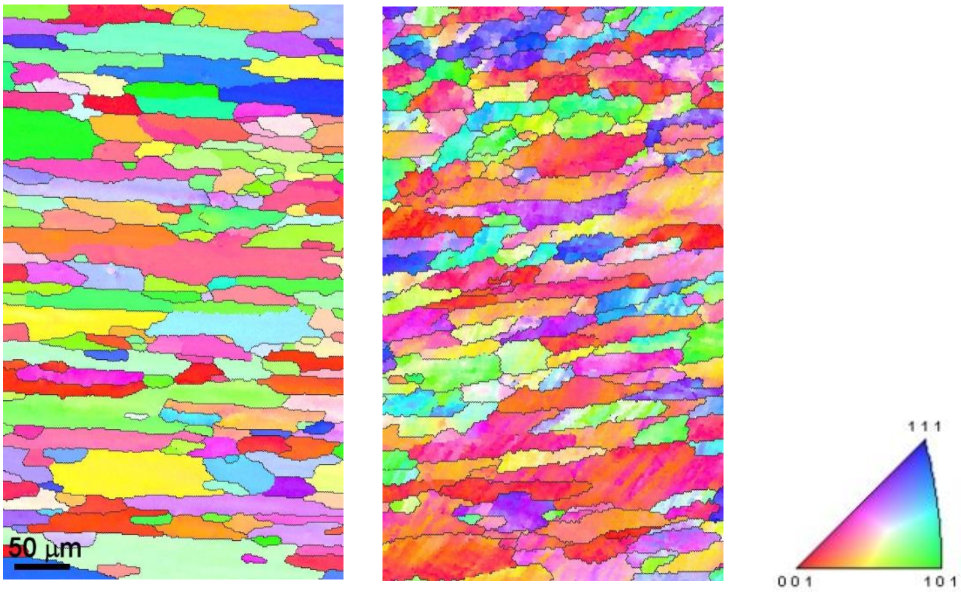

(a) (b)

Fig. 4.29. IPF map with HAGBs of cold rolled 6016 Al alloy (TD-plane, the scale bar is || to RD): a) pre-rolling microstructure; b) asymmetrically rolled sheet with 20 % thickness reduction and roll diameter ratio of 1.5. The larger roll contacts the top surface of the sheet [2s].

It is of key importance to evaluate the amount of shear imposed in ASR process (see Fig. 4.30). The value of shear could be approximated by the calculations reported by S-B Kang et al. [96]:

$$\gamma_{xz} = \frac{2}{e+s}\left[R_1 \cos^{-1}\left(\frac{R_1+s-e)}{R_1}\right) - R_2 \cos^{-1}\left(\frac{R_2+s-e)}{R_2}\right)\right] \tag{4.25}$$

where R_1 and R_2 are the top and the bottom roll radii, while other parameters are shown in Fig. 4.30.

A combination of simple shear ε_{xz} with compressive strain ε_{zz} makes the process geometrically nonlinear. In such a process the equivalent strain cannot be calculated based on the linear integration of the infinitesimal strains. An alternative equation obtained from the literature [97, 98] is employed to estimate the equivalent strain ε_{eq}:

$$\varepsilon_{eq} = \frac{2}{\sqrt{3}}\phi \ln\frac{1}{\alpha} \tag{4.26}$$

$$\phi = \left[1 + \left(\frac{\alpha^2}{1-\alpha^2}\tan\psi\right)^2\right]^{1/2} \tag{4.27}$$

where ψ is the apparent shear angle with respect to the normal direction and α is a degree of thickness reduction.

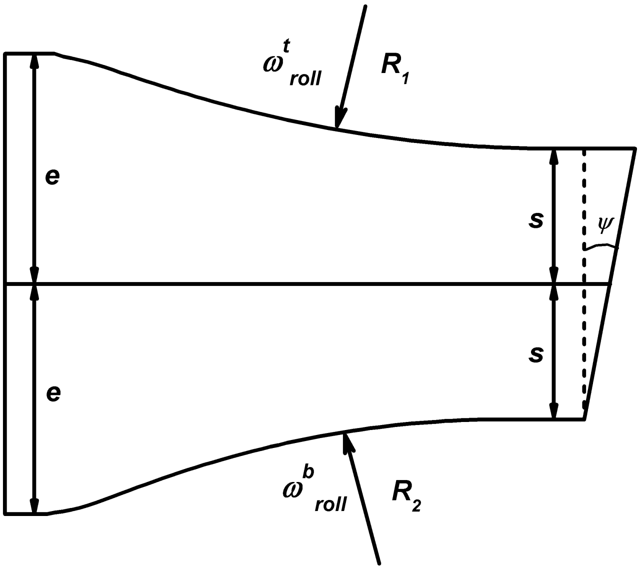

Fig. 4.30. Schematic illustration of the roll gap in ASR [2s].

The apparent angle of shearing is estimated from a difference between the RD-ND shear distances introduced by the upper and lower rolls of radii R_1 and R_2, respectively. The shear distance S_x for a particular roll of diameter R_x is approximated as the arc length between the contact of the sheet with the roll and the point of release [96]. For simplicity, it is assumed that the release occurs at the point of a minimum distance between the rolls while the contact point is determined as the point of intersection between the plane of the sheet surface and the arc of the roll. Under these assumptions, the S_x is expressed as [2s, 18s]:

$$S_x = R_x \cos^{-1}\left(\frac{R_x + s - e}{R_x}\right) \tag{4.28}$$

Consequently, the shear angle ψ (c.f. Fig. 4.30) could be expressed as [2s, 18s]:

$$\psi = \tan^{-1}\left(\frac{S_2 - S_1}{2s}\right) \tag{4.29}$$

where S_2 and S_1 are the shear distances associated with the large and small rolls, respectively.

An equation allowing to approximate the shear strain induced by the differential speed ASR process, in which two rolls of identical radii R rotating with different angular velocities, could be derived in analogy to equation 4.25 [2s]:

$$\gamma_{xz} = \frac{2R}{e+s}\left[\frac{\omega_{roll}^{t}}{\omega_{roll}^{b}}\cos^{-1}\left(\frac{R - \omega_{roll}^{b}(e-s)/\omega_{roll}^{t}}{R}\right) - \cos^{-1}\left(\frac{R+s-e}{R}\right)\right] \tag{4.30}$$

where ω_{roll}^{t} and ω_{roll}^{b} are the angular velocities associated with the top and bottom rolls, respectively.

In the manner of an analogy to equation 4.29, the shear angle in the differential speed ASR process could be computed as [2s]:

$$\psi = \tan^{-1}\left(\frac{R}{2s}\left[\frac{\omega_{roll}^{t}}{\omega_{roll}^{b}}\cos^{-1}\left(\frac{R - \omega_{roll}^{b}(e-s)/\omega_{roll}^{t}}{R}\right) - \cos^{-1}\left(\frac{R+s-e}{R}\right)\right]\right) \tag{4.31}$$

The deformation expressed by equations 4.25-4.31 disregards both the strain path changes in a rolling gap and the contribution of a redundant shear strain due to high friction between the sheet surface and the roll.

In order to investigate the crystallographic aspects of the asymmetric rolling process, the texture evolution is modeled with the VPSC model as a function of different combinations of plane strain compression and simple shear, which could be obtained in this rolling condition. The VPSC model was chosen because of high qualitative accuracy and fast computational time. Fig. 4.31 presents the results of texture calculations for 50% thickness reduction schedules with a gradually increasing shear coefficient K (ratio of shear to normal strain) assuming a random distribution of orientations as an initial texture.

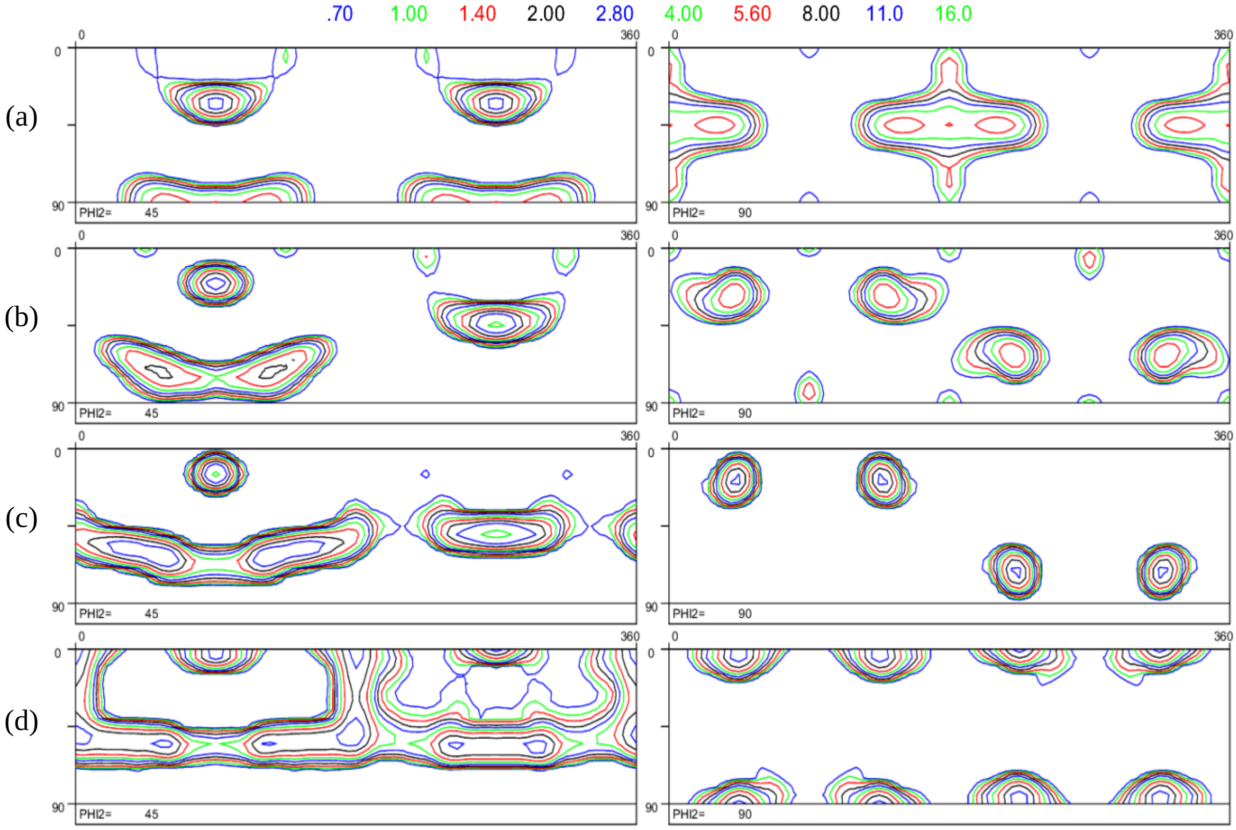

Fig. 4.31. Results of texture simulation with the VPSC model (n_{eff}=10) for 50% thickness reduction ($\varepsilon_{xx}=const$) with various amount of shear γ_{xz}: a) plane strain compression, K=0; b) K=2; c) K=5; d) simple shear, ε_{xx}=0, $1/K$=0. Initial texture is random.

The calculated ODF in Fig. 4.31a ($K=0$) corresponds to the conventional rolling texture of FCC materials. The calculated texture reveals three-fold axis symmetry. As a consequence of the simple shear strain along the rolling direction ($K=2$), the orthorhombic symmetry is broken and the Copper component splits up into two orientations which move in opposite directions along the <011>//TD fibre (τ-fibre) whereas the Brass component rotates towards the γ - fibre ({111}//ND), as it is shown in Fig. 4.31b. The intensity of the newly created texture is significantly higher compared to the case of pure plane strain compression. A further increase of the shear ratio ($K=5$) results in the formation of somewhat bended γ - fibre texture components while the Copper orientation further moves towards a 45° rotated cube component (H orientation), as shown in Fig. 4.31c. Figure 4.31d reveals the ODF sections of the simulated deformation texture produced by simple shear only ($1/K=0$). It can be noticed that all the components rotate towards the ideal shear deformation components consisting of the 45°

rotated cube orientation and the γ- fibre. The presented calculations express the main features of texture development during cold rolling process with different amounts of simple shear strain along the rolling direction.

Fig. 4.31 concludes that combinations of plane strain compression and simple shear, as a result of different circumferential velocities of the upper and the lower rolls, result in rotation of the rolling texture towards the shear texture components, while both the intensity and sharpness of the developed orientations depend on the amount of shear imposed during the process.

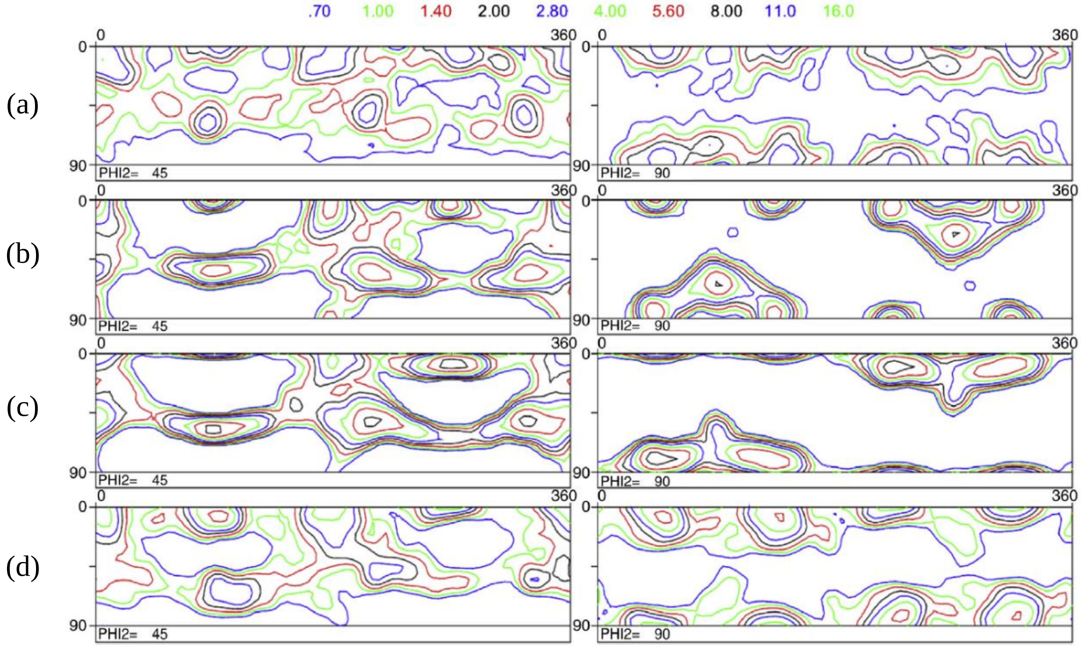

Fig. 4.32. Calculated and measured through-thickness textures in 6016 Al alloy for unidirectional asymmetric rolling with 18% thickness reduction and roll radii ratio of R_1/R_2 =1.5: (a) experimentally measured texture; (b) FCT model, ID_N =0.83; (c) VPSC model ID_N =1.21; and (d) Alamel model, ID_N =0.52 [2s]. The amount of shear imposed in ASR is approximated by equation 4.25.

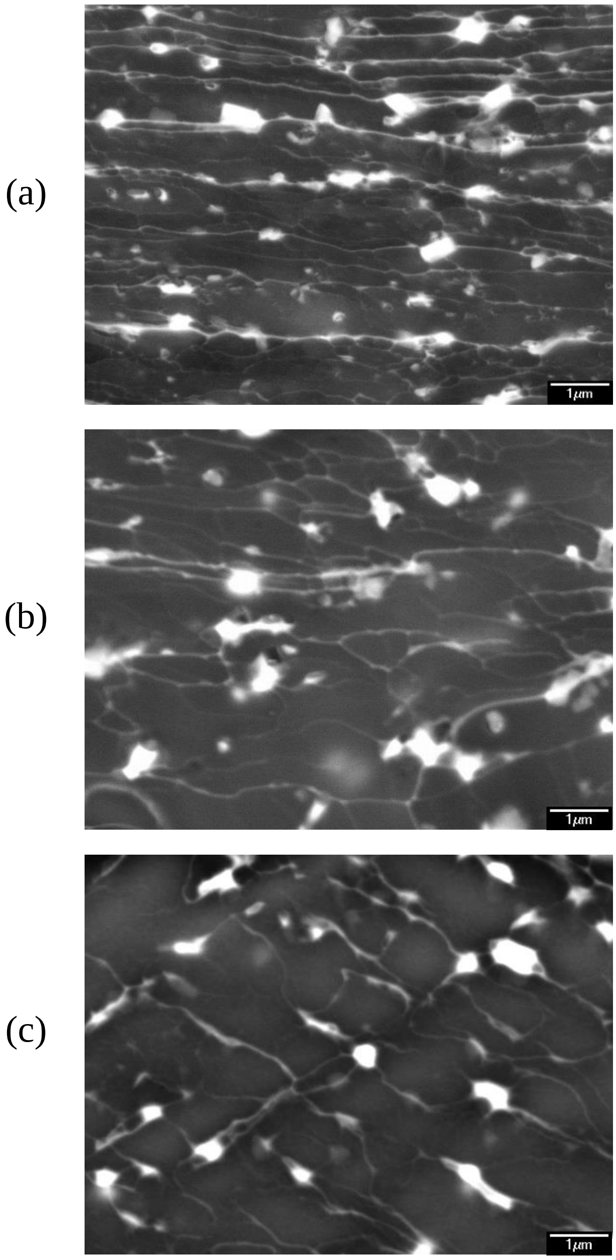

Fig.4.33. Sub-structure development in 6016 Al alloy subjected to various rolling schedules, observed by scanning electron microscope: a) symmetrically rolled material with 87% thickness reduction, b) symmetrically rolled material with 20% thickness reduction, a) asymmetrically rolled material with 20% thickness reduction and roll diameter ratio of 1.5. All figures reveal the TD-plane and the scale bar is parallel to RD [18s].

Analysing the results of texture simulations performed for ASR process (Fig. 4.32), it can be concluded that both the Taylor and VPSC models give reasonable qualitative texture predictions, whereas the Alamel model is most successful among the applied CP approaches. It is obvious that grain interaction phenomena have to be taken into account during the CP modeling of ASR process.

Fig. 4.33 shows the sub-structural arrangements after different rolling schedules. In case of symmetric rolling, the substructure follows the same evolutionary pattern as the high angle grain boundaries, that is, the low angle grain boundaries are arranged along the rolling direction irrespective of the thickness reduction (Fig. 4.33 a and b). Fig. 4.33 c shows an inclined sub-wall arrangement in the asymmetrically rolled material. In contrast to conventional rolling, the dislocation walls seem to be aligned along the in-grain shear patterns, as a result of complex strain mode imposed by the ASR.

4.4 Accumulative roll bonding

Accumulative roll bonding (ARB) process (Fig. 4.34) is one of severe plastic deformation (SPD) methods. During the ARB process, the thickness of the sheet changes between imposed limits, and by repeating the procedure very high strains can be accumulated in the material, and thus significant structural refinement can be achieved. The ARB involves rolling of a stack of metal sheets. Generally, the material is subjected to 50% reduction in one pass and in this way the process can be repeated endlessly. This innovative technology, which was developed by the group of Tsuji [99-101], tends to ensure very fine-grained microstructures (~1μm or even finer) due to grain fragmentation during severe plastic deformation. Apart from deformation phenomena involved in SPD, ARB ensures strong bonding of deformed layers. In the current investigation [22s], the grain fragmentation was observed in AA3003 alloy until the sixth cycle (e_{vM}<4.8) during which both the grain thickness and length gradually decreased before approaching to constant values of 400 nm and 1.3μm, respectively. Accumulative roll bonding seems to be very effective in terms of breaking up thin lamellar grains [22s, 101-103], however, it should be mentioned that the investigated Al alloy contains high amounts of Mn (1.1 wt%), Fe (0.4wt%), and Si (0.18%) elements which lead to the formation of relatively high volume fraction of second phase particles (~5%) with sizes ranging between 1 and 5 μm. These large inclusions induced an increase of local misorientations and tended to produce new high angle grain boundaries [22s]. The morphology of ultrafine grains is important nonetheless there are also other mesoscopic features of severely deformed metals, such as crystallographic structure.

In this view, orientation imaging microscopy is a powerful tool to investigate the microstructural and sub-structural evolution of plastically deformed materials because it provides information on the fragmentation behavior of grains and texture evolution. The fundamental question is how the crystallographic texture tends to evolve during this inventive SPD method.

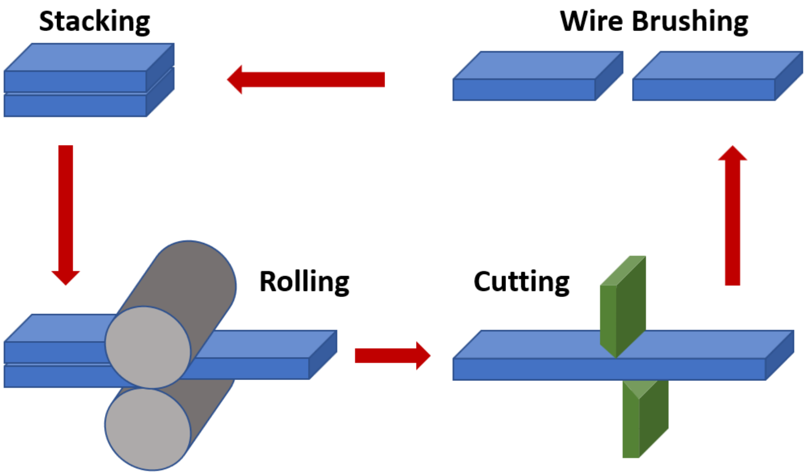

Fig.4.34. Representative scheme of ARB process.

The orientation distribution functions of the samples processed by different ARB cycles (2, 4, 6 and 8) are shown in Fig. 4.35 [22s]. It is obvious that with increasing the number of cycles, the overall texture intensity and the concentration of the contour lines steadily increases (it should be noted that the amount of strain imposed in one pass is 0.8). The maximum level of contour lines increased from 11 in the second cycle to 18 in the eighth cycle. This indicates that by ARB processing a very strong texture tends to develop with sharp components. The evolution of a strong texture with very sharp components during deformation leads to the formation of a band-like structure and prevents the full grain refinement to a submicron scale.

With increasing the number of cycles during ARB, the intensity of the α-fiber decreased while the intensities of the β and τ-fibers show an opposite tendency. Analyzing the α-fiber, which runs from the Goss component towards brass orientation, allows investigating the behavior of the brass component during ARB. It was also shown [22s] that during ARB cycles the intensity of Goss component evolved is negligibly small. Fig. 4.35 suggests that in the early stages of the ARB process the intensity distribution along the first half of the β-fiber is nearly homogeneous, however with increasing the number of cycles the intensity of the copper component tends to grow at the expense of other components [22s].

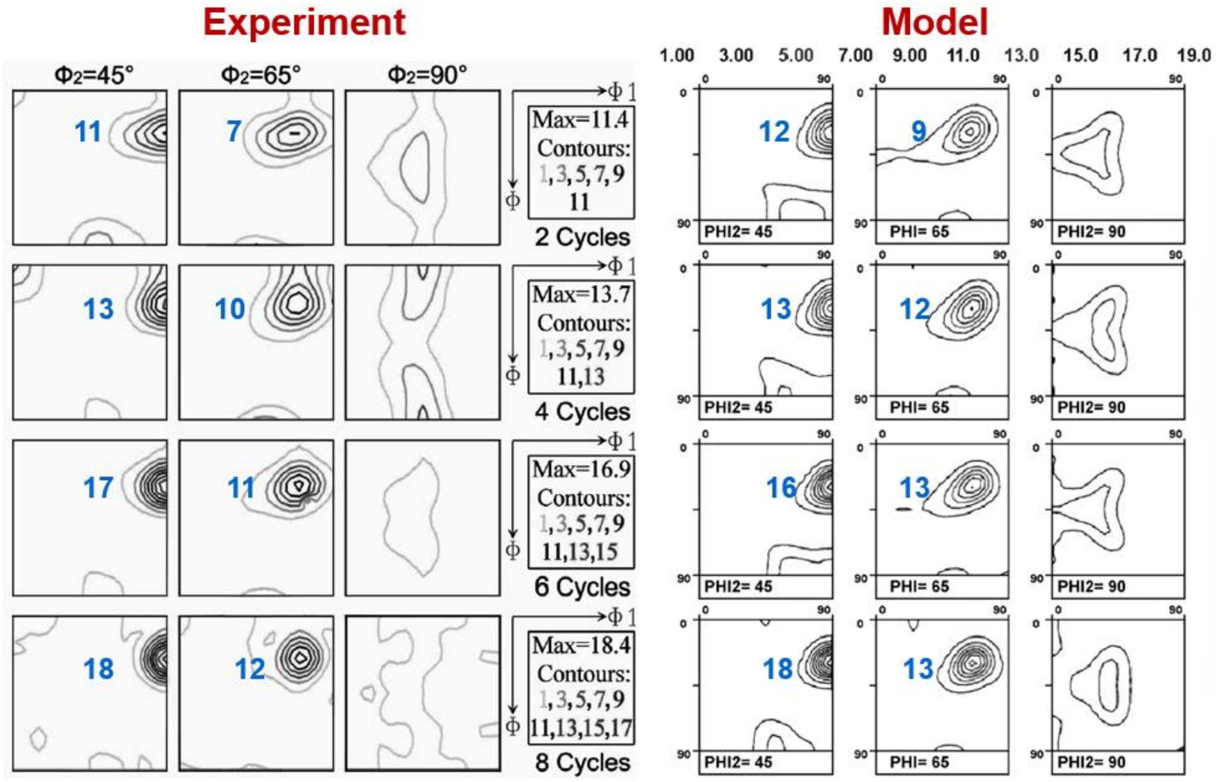

Fig.4.35. Comparison between the experimentally observed ODFs in AA3003 alloy after different ARB cycles and textures calculated with the ALAMEL model [22s].

In order to explain the evolution of specific ODFs, shown in Fig.4.35, the evolution of texture was simulated by means of crystal plasticity theory. In crystal plasticity calculations, the deformation during ARB processing is approximated by a two-dimensional velocity gradient tensor which is composed of a compressive strain added with a simple shear strain [22s]. Taking into account the specific nature of the ARB process, the texture simulations have been performed with the ALAMEL model for different strain modes with various ratios of the simple shear component to the plane strain compression components. The amount of shear in the process is characterized by the shear coefficient *K*. The CP simulation for the subsurface layer was performed with a large value of *K* (*K* = 2.4) due to the localization of shear deformation in this region. The simulation of texture evolution in the mid-thickness region was performed with *K* = 0.1, which implies that even in the mid-thickness layers there will still be a small amount of frictional shear as the accumulative roll bonding trials were carried out without lubrication (in totally dry conditions). Considering the specific stack-and-roll geometry of the ARB process, the subsurface texture after the first ARB pass appears in the central layer of the composite sample in the second ARB pass. Hence, in order to simulate the texture evolution in the middle layer in the ARB pass n_i the Alamel model was applied on the subsurface from previous pass $n_{(i-1)}$ with a deformation mode that was characterized by a small $K=0.1$. The calculated textures are in very good qualitative and quantitative agreement with the experimentally measured ODFs. As shown in Fig. 4.35, the model calculation has produced the textures, which exhibit a strong β-fiber with a maximum at copper/Dillamor component whereas the intensity gradually drops while moving towards the brass orientation. Similar texture evolutionary patterns were reported by Kim et al. [101] and Heason and Prangnell [102].

4.5 Severely deformed sheets by conventional rolling

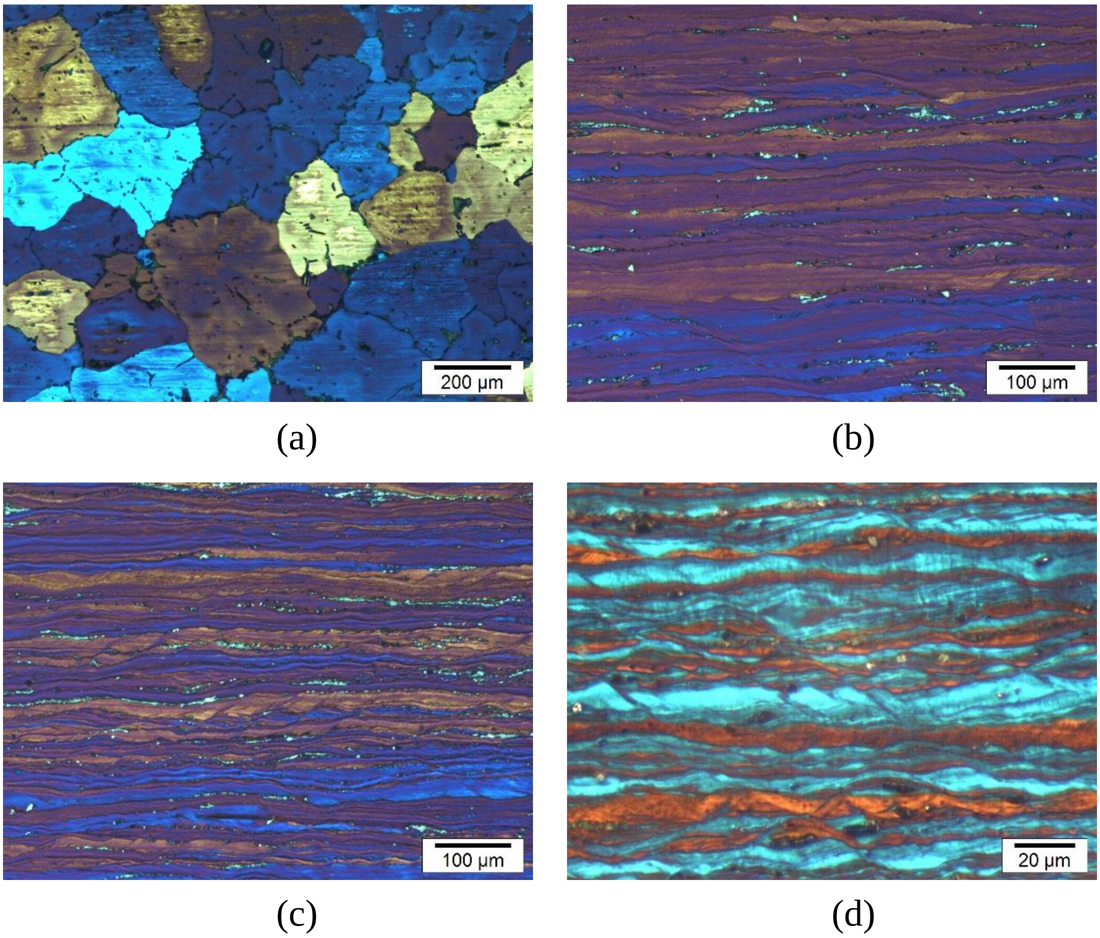

(a) (b)

(c) (d)

Fig. 4.36. Microstructure evolution in particle containing Al-2.8Mg alloy (TD-plane): a) as-cast material; b) 85 % cold rolling reduction; c) 91% reduction; d) 98% reduction [17s].

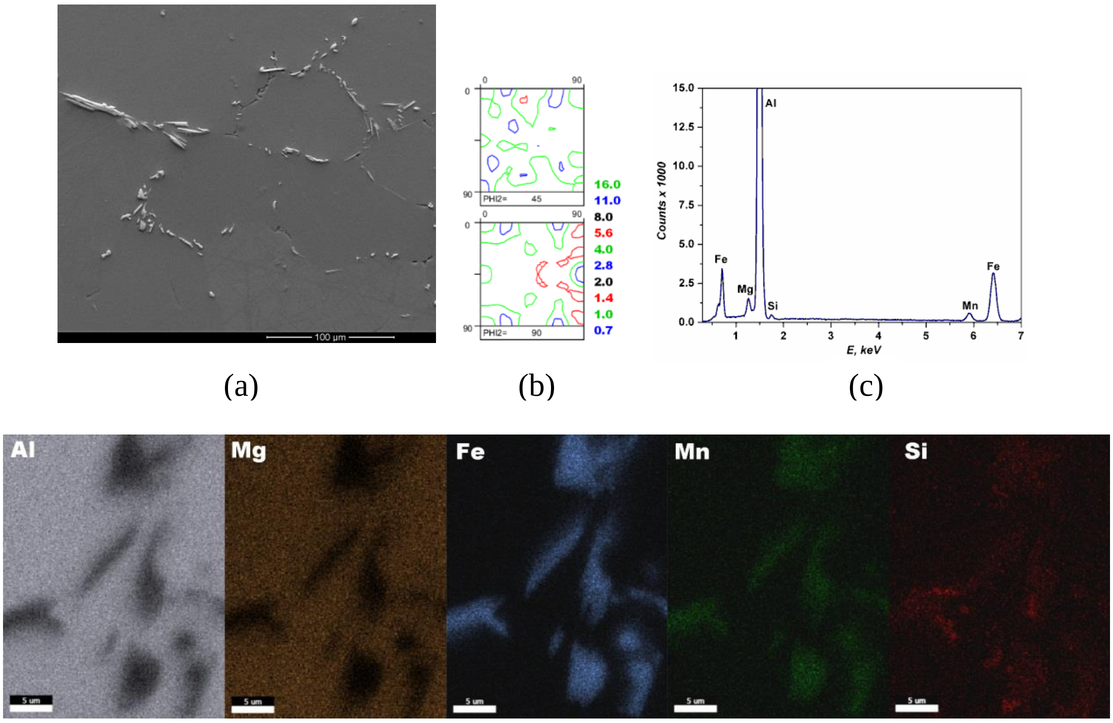

(a) (b) (c)

(d)

Fig. 4.37. As-cast material: a) SEM microstructure; b) texture of the as-cast material; c) typical EDX spectrum of constituent particles located on grain boundaries; d) EDX elemental maps collected from the constituent particles and surrounding Al matrix. The black color on figure (d) is associated with very low (or zero) concentration of particular element [9s].

The chemical composition of the material controls the formation of the large non-deformable particles whilst the magnitude of strain conditions the deformation flow around these hard inclusions. Generally, the as-cast structure is homogenized and hot rolled which gives rise to partial dissolution of the large constituent phases. The as-cast Al-2.8 Mg alloy presented in Figs. 4.36 and 4.37 [17s] was cold rolled to various final thicknesses without heat treatment with the aim to reveal the effect of large second phases on the microstructure and texture evolution. As shown, the deformation lamellas are distorted by the presence of the large particles whereas the level of distortion becomes more pronounced with increasing the rolling reduction which eventually gives rise to fragmentation of the lamellas at high reduction levels. At the higher strains, the lamellar spacing decreases while the in-grain misorientation significantly increases accounting for grain sub-division. Finally, a high angle grain boundary is created when the misorientation exceeds the limit misorientation that still can be accommodated by a specific configuration of dislocations. Thus, it is concluded here that the grain fragmentation could occur due to crystallographic grain sub-division and by the presence of large non-deformable constituents.

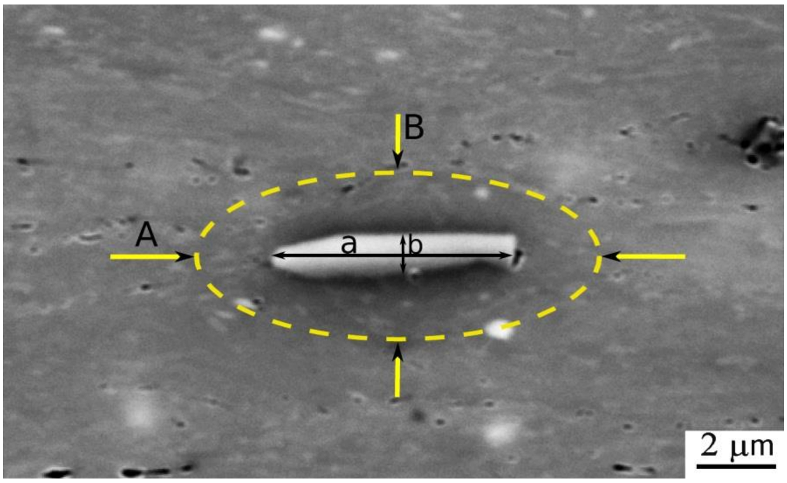

Fig.4.38. Typical example of a large constituent particle with the corresponding particle affected deformation zone (TD-plane, the scale bar is || to RD), observed in Al alloys [9s].

As it was shown by Ashby [104, 105], the presence of non-deformable particles in commercially produced aluminum alloys triggers additional strain hardening due to the gradients of deformation proportional to the particle spacing. The strain heterogeneity [105] during deformation in the vicinity of large hard inclusions (larger than 1μm) gives rise to the creation of a particle affected deformation zone (PADZ). In the PADZ (see Fig.4.38), the lattice is substantially misoriented with respect to the particle-free matrix. The magnitude of the rotation is related to the shear strain, the particle diameter, and the radius of the rotated zone [106, 107], whereas the misorientation in the PADZ follows a declining trend with increasing distance from the particle [108]. This implies that the deformation texture in the PADZ deviates significantly from the texture of the particle-free matrix, which is usually aligned along the β-fibre. Apart from the particle size and strain magnitude, the local lattice rotation depends on the macroscopic strain mode and the particle shape. Humphreys [108] has reported lattice rotation about ⟨111⟩, ⟨101⟩ and ⟨121⟩ axes in tension whereas Engler [109] has observed matrix rotation around ⟨121⟩ axes and the transverse direction (TD) in cold rolled particle-containing Al alloys. Significant local distortions of the deformed microstructure in the PADZ are reported by Liu et al. [110]. It is claimed that a symmetric pattern of TD-rotations of the alternating sign is found in the PADZ while the largest lattice rotations occur at the tip of elongated particles. Extensive TD rotation is also observed in particle-containing ferritic steel [111], whereas the results of an investigation with electron backscattering diffraction suggest that the crystal lattice rotation around TD is independent of the initial crystal orientation which is additionally confirmed by the work of Humphreys and Ardakani [112].

Fig.4.39 reveals a distribution of constituent particles in the material after various degrees of rolling reduction [9s]. The large constituents tend to get aligned along the rolling direction while the average distance between the particles along the normal direction is reduced as a result of high deformation levels involved in the cold rolling. It is evident from Fig.4.39 that the large constituent particles cannot resist high strains and fragment with increasing rolling reduction. The fragmentation results in a decrease of the aspect ratio of particles. For instance, sample A reveals ~10% of particles with an aspect ratio larger than 3.5 and sample B shows only ~2% of inclusions with comparable geometry, whereas after 96% reduction the amount of particles with aspect ratio > 3.5 is negligibly small. Additionally, it can be noticed that at reductions ≥ 96%, as a result of fragmentation: (i) the majority of non-deformable inclusions is characterized by an aspect ratio smaller than 1.5 and (ii) the fraction of small particles with area ≤5 μm^2 drastically increases.

In FCC materials with high and medium stacking fault energies, the deformation texture components develop homogeneously along the α and β fibres at relatively low rolling reductions (below 70%). At higher strain levels, individual texture components of the β-fibre tend to intensify, whereas the position of maximum intensity depends on both the degree of rolling reduction and the initial texture. It was shown [9s, 17s, 27s, 29s] that in large non-deformable particle-containing Al alloys the α-fibre reveals a tube of orientations running from the $\{101\}\langle 121\rangle$ towards the $\{110\}\langle 001\rangle$ component, while at the higher thickness reduction, such as 99%, the α-fibre is characterized by a single maximum around the Brass orientation, i.e. all components are distributed along the β-fibre. Conversely, the β-fibre in the particle-containing Al alloys exhibits a relatively homogeneous distribution even after the most severe thickness reductions (see Fig. 4.40). The analytical approximation of the β-fibre allows analyzing a deviation of the evolved deformation texture with respect to the analytically described one. It was shown (Fig. 4.40) [9s] that the measured β-fibre components are slightly shifted compared to the analytically predicted orientations.

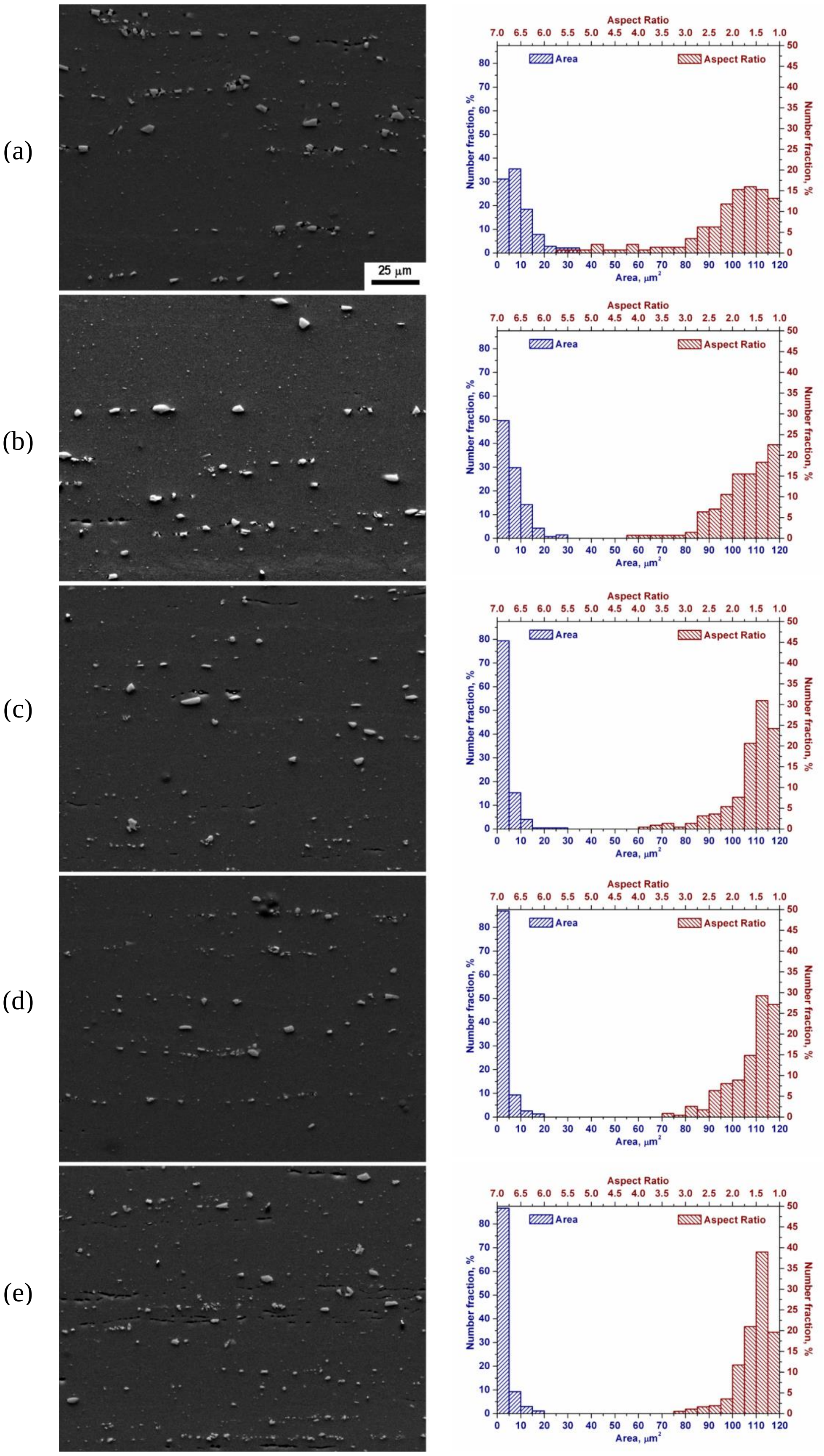

Fig.4.39. Constituents after various rolling reductions with corresponding distributions of area and aspect ratio of the particles in the transverse direction plane: a) 74% reduction; b) 85% reduction, c) 96% reduction; d) 97% reduction, e) 99.1% reduction [9s].

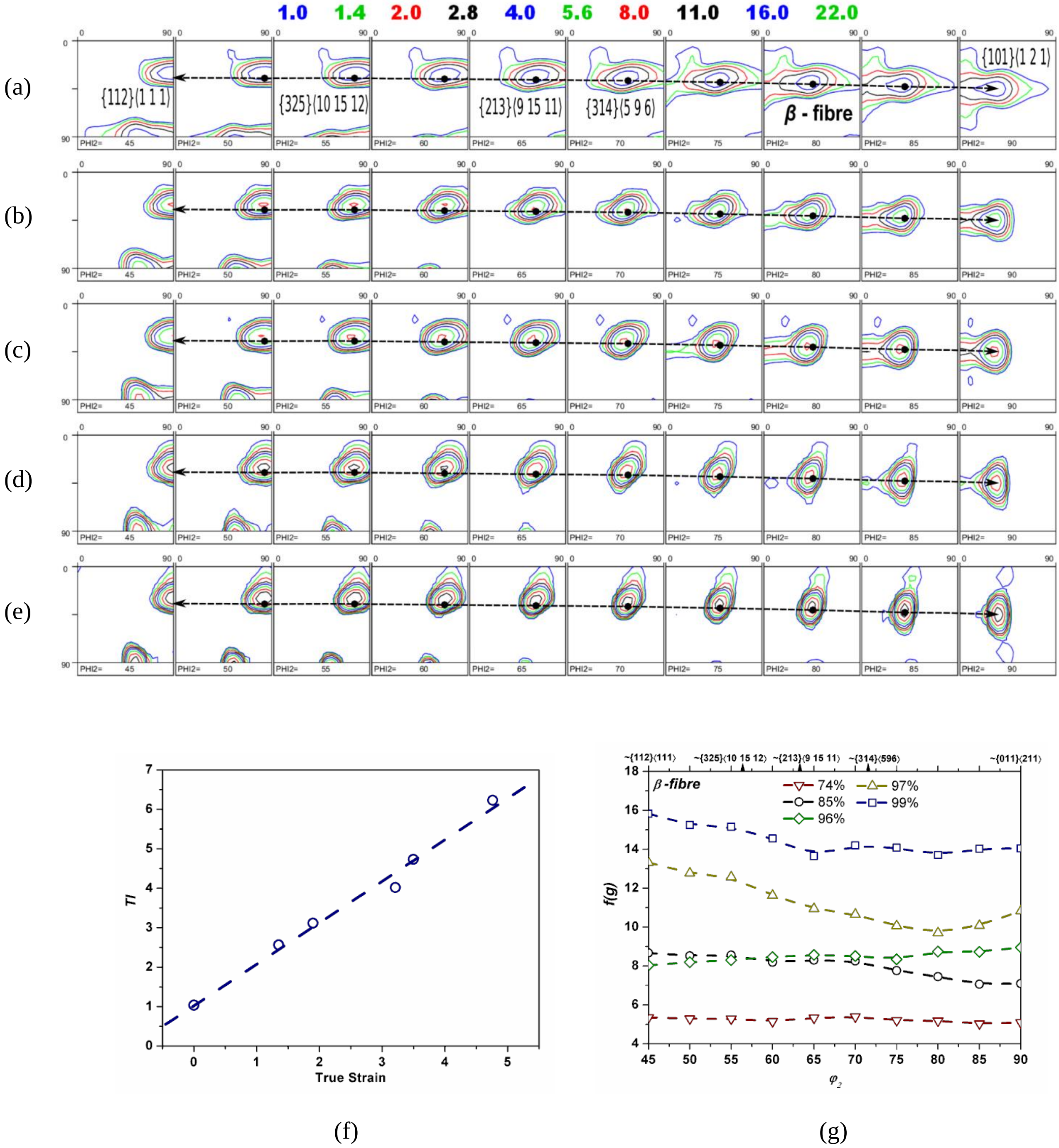

Fig. 4.40. Evolution of deformation texture in the investigated material after various rolling reductions [9s]: a) 74%; b) 85%; c) 96%; d) 97%; e) 99%; f) dependence of texture index (*TI*) on the amount of deformation; g) distribution of orientation intensity along the β-fibre. The dashed line shows the position of β-fibre orientations calculated by equation 3.10. The β-fibre is shown from φ_2=45° toward φ_2=90° with a step $\Delta\varphi_2$= 5°.

As Fig. 4.40 shows, a ~5° deviation was observed along the τ-fibre (⟨110⟩//TD) and this deviation persists in the first part of the skeleton line (between {112}⟨111⟩ and {213}⟨9 15 11⟩) while towards the tail of the β-fibre running from {314}⟨596⟩ to {101}⟨121⟩ the difference tends to vanish. The quantitative texture analysis, presented in Fig.4.40, reveals that the texture index of the deformed materials increases linearly with the imposed strain [9s].

In rolling processes performed under well-lubricated conditions, the shear deformation is mainly concentrated within a thin surface layer and thus the rolling could be approximated by PSC [9s]. Figs.4.41 a-e reveal von Mises strain maps of the particle-containing matrix subjected to PSC. Both single and multi-particle cases are considered which were subjected to 30% deformation with the aim to obtain an indication of the qualitative and quantitative evolution of strain fields in the vicinity of particles. As revealed in Fig.4.41a, the presence of a non-deformable inclusion triggers strain localization and gives rise to the development of a particle affected deformation zone (see Fig.4.41b). In the PADZ, the localized strains exceed significantly the value of the macroscopic one. A strong strain gradient can be observed in the close vicinity of the particle along the rolling direction. Figs. 4.41 c-e show various spatial distributions of particles of different aspect ratios. In the current FEM study, the particles were aligned along the RD considering different hypothetical spatial configurations, which could occur in rolled materials as it is shown in Fig. 4.41. Contrarily to a particle-matrix system, where the strain is concentrated around one single elastic inclusion (Fig.4.41 a), in a multi-particle-matrix case the strain fields around the individual particles tend to interact (Figs. 4.41 c-e) leading to the evolution of highly strained zones (HSZ). Depending on the spatial distribution of particles and their aspect ratio, the localized strain in the HSZ exceeds 2 to 3 times the value of the macroscopic strain (Figs. 4.41 c and d). It could also be noticed that the particles with a small aspect ratio (Fig.4.41 e) account for a minor strain gradient compared to the particles of a larger aspect ratio (Fig.4.41 d). However, the high strain concentration is observed along the normal direction between the neighboring particles of Fig.4.41 e. In addition, the strain localization at the curved edges of the quasi-spherical particles (Fig.4.41 e) is less pronounced compared to the highly elongated inclusions despite the fact that both groups of particles have identical curvature of the edges.

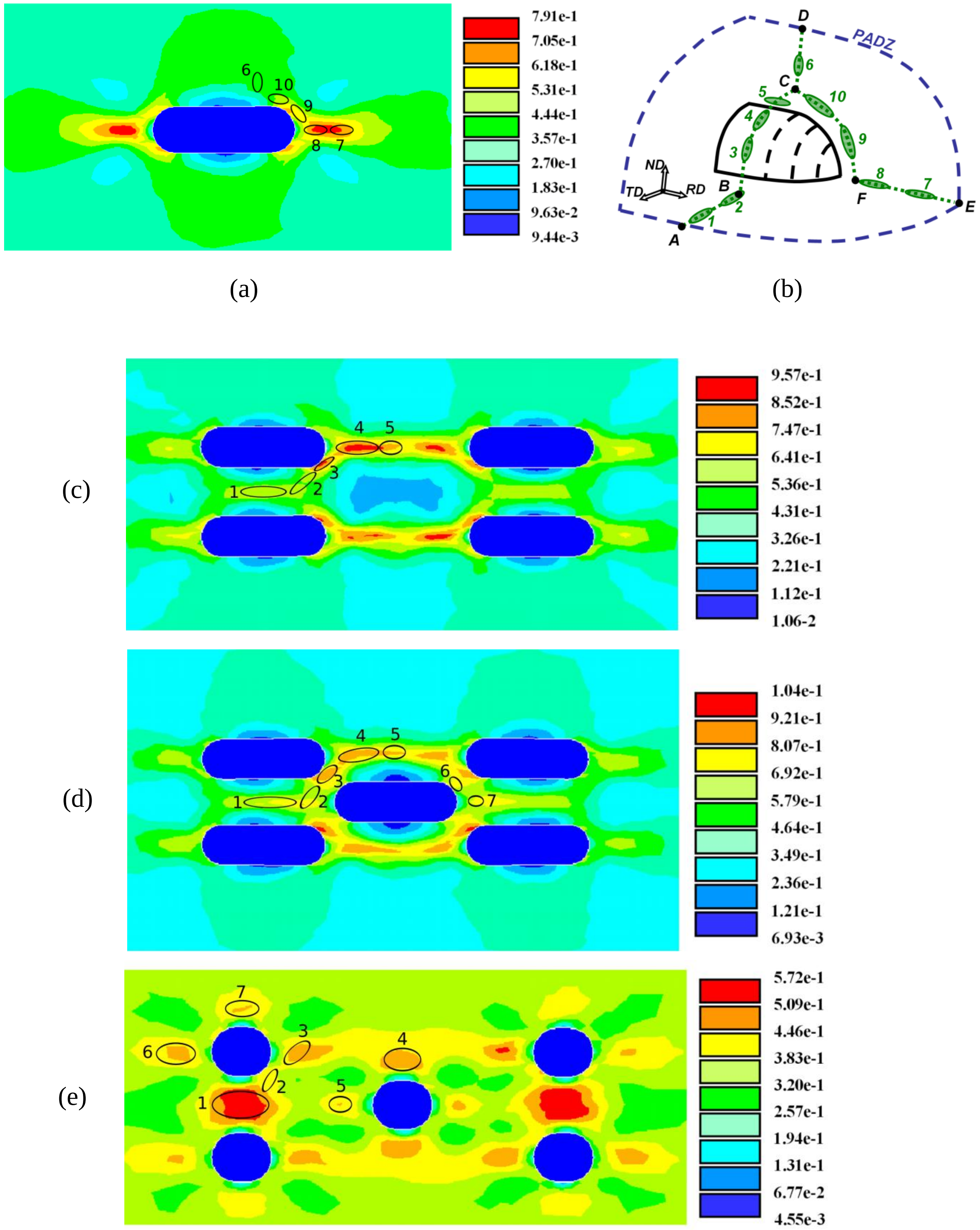

(a) (b)

Fig.4.41. 3D FEM calculations of strain distribution around non-deformable inclusions, performed by ANSYS® software: a) single elongated particle of aspect ratio of ~3; b) schematic illustration of ¼ of single particle with characteristic areas along radial and longitudinal directions (areas 6-10 are shown in figure (a); c) four elongated particles of aspect ratio of ~ 3; d) five elongated particles of aspect ratio of ~ 3; e) five quasi-spherical particles of aspect ratio of ~ 1.2 [9s]. Figures reveal the TD plane.

Table 4.2. True strains observed in characteristic regions of particle affected deformation zone (the strains are normalized with respect to the maximum strain value) [9s].

Figure	**Region**	**e_{11}**	**e_{22}**	**e_{33}**	**e_{12}**	**e_{13}**	**e_{23}**
4.41b	1	0.7±0.2	0.3±0.2	-1	0	0	0
	2	0.17±0.1	0.83±0.1	-1	-0.1±0.07	0.1±0.05	0.4±0.2
	3	0.15±0.1	0.85±0.1	-1	0	0	0
	4	0.5±0.2	0.5±0.2	-1	0	0	0.02±0.01
	5	0.73±0.2	0.27±0.2	-1	0.03±0.02	0.03±0.02	0.12±0.07
	6	0.80±0.15	0.2±0.15	-1	0	0	0.05±0.03
	7	1	-0.2±0.1	-0.8±0.1	0	0	0
	8	1	-0.25±0.15	-0.75±0.15	-0.1±0.05	0.1±0.05	0.05±0.02
	9	1	-0.25±0.10	-0.75±0.10	-0.15±0.05	0.7±0.2	0.1±0.05
	10	0.70±0.15	0.30±0.15	-1	-0.1±0.05	0.8±0.2	0.1±0.05
4.41 c	1	0.7±0.1	0.3±0.1	-1	0	0.08±0.04	0
	2	0.7±0.12	0.3±0.12	-1	0.15±0.10	0.4±0.25	0.2±0.1
	3	0.9±0.08	-0.1±0.08	0.82±0.08	0.3±0.15	1	0.15±0.1
	4	1	-0.26±0.1	-0.74±0.1	0	0.25±0.1	0.1±0.05
	5	1	-0.23±0.1	-0.77±0.1	0	0	0
4.41d	1	0.77±0.07	0.23±0.07	-1	-0.07±0.05	0.02±0.01	0.02±0.01
	2	0.95±0.03	0.05±0.03	-1	-0.15±0.05	0.4±0.15	0.1±0.05
	3	0.6±0.1	-0.2±0.1	0.8±0.1	0.15±0.08	1	0.15±0.1
	4	1	-0.2±0.1	-0.8±0.1	-0.17±0.05	0.15±0.07	0.7±0.05
	5	1	-0.16±0.10	-0.84±0.10	-0.02±0.01	0.02±0.01	0.04±0.02
	6	0.6±0.1	-0.05±0.02	-0.55±0.05	0.09±0.03	1	0.08±0.04
	7	1	-0.15±0.07	-0.85±0.07	0.25±0.15	0.15±0.1	0.1±0.05
4.41e	1	0.86±0.10	0.14±0.10	-1	0.05±0.03	0.02±0.01	-0.02±0.01
	2	0.88±0.10	0.12±0.10	-1	0.04±0.02	0.05±0.02	0.06±0.03
	3	1	-0.20±0.10	-0.80±0.10	0.10±0.05	0.10±0.05	0.10±0.05
	4	0.80±0.10	0.20±0.10	-1	-0.12±0.07	0.05±0.03	0.11±0.05
	5	1	-0.15±0.10	-0.85±0.10	0.10±0.05	0.15±0.10	0.15±0.05
	6	1	-0.15±0.07	-0.85±0.07	0	0	0
	7	0.85±0.10	0.15±0.10	-1	0.05±0.03	0.1±0.07	0.1±0.07

Apart from strain localization, there is an issue of how the macroscopic strain mode is translated to the PADZ. The deformation flow in the PADZ is described by a complex strain field e_{ij} depending on the particle shape and the spatial distribution of particles. Fig.4.41 b shows areas with characteristic strain modes listed in Table 4.2. Characterizing the strain distribution in the PADZ along TD between points A and B (Fig.4.41 b) it becomes obvious that the local strain modes in regions 1 and 2 deviate significantly from the macroscopic one. Region 1 is subjected to compression along the normal direction with essential RD extension (e_{11}) (see Table 4.2) while region 2 is deformed by compression with essentially TD extension (e_{22}) added with minor RD-ND (e_{13}), TD-ND (e_{23}), and RD-TD (e_{12}) shear components. Strain characterization between points B and C in Fig.4.41 suggests that the ND compression with essentially TD strain (e_{22}) in region 3 gradually transforms to compression with essentially RD strain in regions 4 and 5. Region 6 between points C and D is equally characterized by the ND compression with essentially RD strain. Analyzing the strains along the RD between points E and F (Fig.4.41 b) it could be concluded that PSC in point E transforms to tension in region 7 whereas in region 8, located closer to the edge of the particles, the extension is complemented with an RD-ND shear component (e_{13}). In regions located along the path between points F and C, the tensile deformation of region 9 transforms to compression with essentially RD elongation in the region 10. In both regions 9 and 10, the deformation is completed with the RD-ND shear since these areas are located close to the edge of the particle.

In multi-particle cases shown in Figs. 4.41 c-e, the characteristic areas (regions 6-10 between points C and E in Fig.4.41 b) of individual particles tend to overlap during the deformation. The strain mode in region 1 of Fig.4.41 c (see Table 4.2) is identical to the corresponding region 6 of Fig.4.41 b however the strain value is amplified significantly due to an overlap of the strain fields. In area 2 of Fig.4.41 c, located closer to the curved edge of the particle, the shear strain tends to increase and in region 3 the RD-ND shear prevails over the compression along ND. In region 4 (Fig.4.41 c), the tensile strain is added with a small amount of shear deformation while in area 5 the shear components become negligible. The strain distribution in regions 1-5 in the five particle case (Fig.4.41 d) resembles the four-particle case (Fig.4.41 c) despite the fact that one additional particle is placed in the middle. The RD-ND shear prevails over the tensile strain in area 6 of Fig.4.41 d while region 7 is characterized by the tensile strain mixed with minor shear components (see Table 4.2). With five quasi-spherical particles, cf. Fig.4.41 e, the emerging strain patterns suggest that the strain is less concentrated around the curved edges of the particles which implies that shear strain components are less developed compared to elongated particles. Identically to the cases shown in Figs. 4.41 c and d, the strain state in the regions 1, 2, 4 and 7 (Fig. 4.41 e) is characterized by compression while regions 3, 5, and 6 are subjected to tensile deformation with minor shear strain components.

5. Recrystallization

5.1 Diversity of annealing textures in Al alloys: theoretical background and experimentally observed evidences

Recrystallization annealing is the finishing texture forming process in the chain of subsequent solid-state transformations occurring in the production route. Recrystallization is accompanied by a drastic change in microstructural morphology and softening of deformed material via nucleation and subsequent growth of strain-free grains. The qualitative and quantitative evolution of the crystallographic texture during recrystallization annealing is affected by a number of parameters such as the mechanical parameters pertaining to strain mode and amplitude and the thermal parameters pertaining to annealing time and temperature, summarized in Refs. [2s, 7s, 9s, 10s, 15s, 17s-19s, 21s, 26s-29s, 31s, 35s].

Because of its “genetic” character, the recrystallization microstructure and texture depend both on hot band and cold rolling microstructural features [2s]. During the plastic deformation, grains of various orientations accumulate different amounts of stored energy due to the diverse activity of slip systems. The evolution of substructure is conditioned by strain mode and strain amplitude [18s]. Even when the macroscopic strain mode is monotonic the stresses necessary to deform grains of different orientations are distributed heterogeneously across the grains because the neighboring grain boundaries strongly affect the local strain state. This heterogeneous strain distribution accounts for local orientation spread within each particular orientation, thus creating a sub-structure network.

Apart from the strain mode and strain amplitude, the evolution of substructure in a particular grain is conditioned by the crystallographic orientation of the grain. The grains of a polycrystalline aggregate change their shape according to the macroscopic strain mode applied. During plastic deformation, only a limited fraction of the deformation energy is stored in the material in the form of elastic energy associated with the dislocation density which is distributed heterogeneously among the individual grains. The diversity of the stored energy in the crystals is one of the major factors affecting the kinetics of recovery as well as the recrystallization behavior during annealing. Both recovery and recrystallization are softening mechanisms driven by the release of stored energy [26s]. Thus, strict control of the deformed state is of key importance since it determines the initial structure for the subsequent recrystallization treatment. This is particularly true for texture as there is ample evidence that the cold rolling texture is of major importance for the ensuing recrystallization texture. Various combinations of the α and β deformation fibres produce a vast variety of recrystallization textures that strongly differ both qualitatively and quantitatively even though the metals under consideration have comparable values of stacking fault energy. In conventionally hot and cold rolled Al alloys, the deformation texture transforms to the α and θ fibres with characteristic maxima on the Goss, P ($\{011\}\langle 233\rangle$) and cube orientation [2s, 51, 113, 114].

During nucleation and growth stage of recrystallization, an orientation selection takes place which is referred to *oriented nucleation* or *oriented growth* [2s, 51]. Oriented nucleation occurs by the formation of recrystallization nuclei at preferred microstructural sites of specific orientations, which recover more easily than others. The annihilation of dislocations produces dislocation-free areas, which grow by virtue of a difference in the stored energy between the nucleus and the deformed matrix. According to the oriented growth mechanism, the nuclei of particular misorientations with respect to the deformed matrix exhibit increased mobility as compared to nuclei of arbitrary misorientation. In FCC metals, the preferred relationship of increased mobility during annealing is generally described by a 40° rotation about a common <111> axis between disappearing deformed and growing recrystallized grains [2s, 51].

Low or high stored energy nucleation is another much ado question pertaining to recrystallization phenomena [2s, 51]. Low stored energy nucleation claims that regions with a reduced stored energy of plastic deformation (either by a less dense network of dislocations or lower misorientation gradients) are more prone to develop recrystallization nuclei which grow at the expense of regions with a high stored energy, e.g. by a mechanism as strain-induced boundary migration (SIBM). Conversely, nucleation may be favored in high stored energy regions of the substructure because of a local increase in driving force for recovery and sub-grain growth or coalescence at the expense of the surrounding regions where the recovery is sluggish.

The vast body of experimental evidence [115-117] supports that RX is controlled by low stored energy nucleation in metals. Recent measurements of the stored energy after deformation show that the low-stored energy grains are favored during recrystallization.

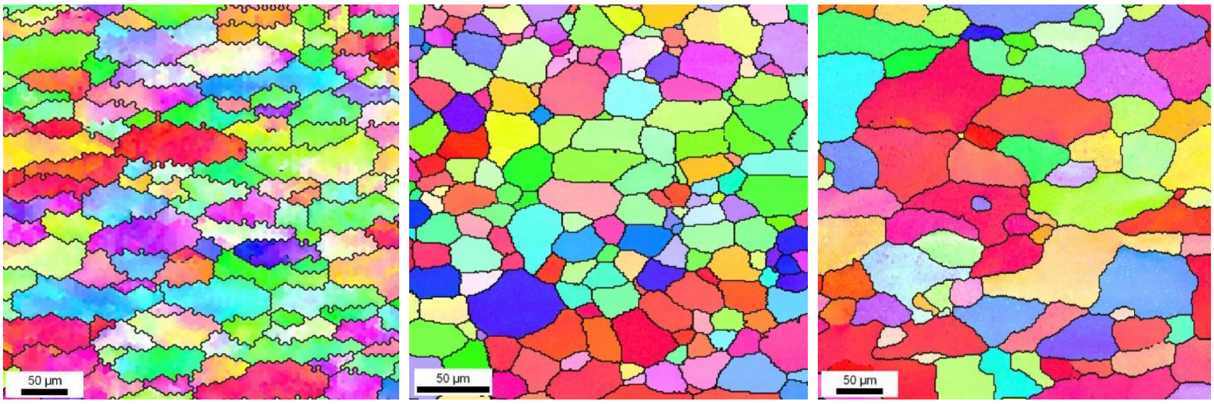

(a) (b) (c)

Fig. 5.1. Microstructures (TD-plane, the scale bar is ‖ to RD), revealed by the orientation contrast microscopy, evolved in conventionally rolled and annealed 6016 aluminum alloy: a) ~87% reduction followed by annealing at 360°C/3600 seconds; b) 87% reduction followed by annealing at 550°C/30 seconds; c) 20% reduction followed by annealing at 550°C/30 seconds [2s]. The IPF color stereographic triangle is shown in Fig. 5.3.

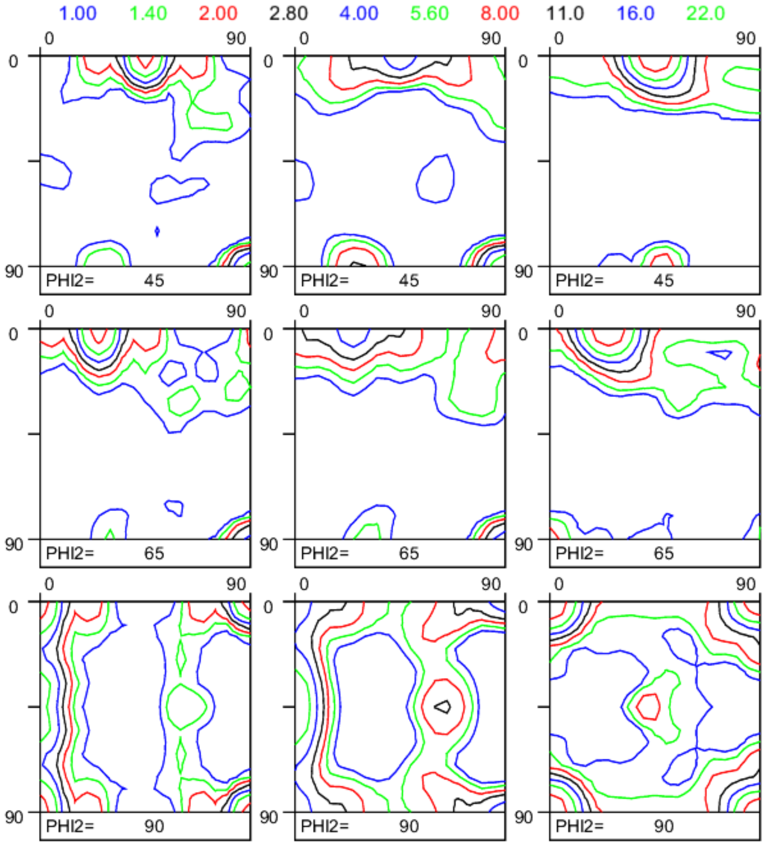

(a) (b) (c)

Fig. 5.2. Texture evolution in recrystallized 6016 aluminum alloy: a) ~87% reduction followed by annealing at 360°C/3600 seconds; b) 87% reduction followed by annealing at 550°C/30 seconds; c) 20% reduction followed by annealing at 550°C/30 seconds [2s].

The principle of low stored energy nucleation is also confirmed by transmission electron microscopy and neutron diffraction measurements [115-117]. Alternatively, for other materials, it appears that new RX nuclei appear in the high stored energy domains of the deformed structure. The high stored energy nucleation occurs in cold rolled low-carbon steels, different geological materials and materials with a low symmetry [51]. In the case of steel, it turns out that high-stored energy nucleation after cold rolling changes to low-stored energy after rolling at elevated temperatures (500-700°C). These observations suggest that the orientation selection in the nucleation stage depends on the extent of dynamic recovery during deformation. In materials with little or no dynamic recovery, the static recovery processes occurring more extensively in the high stored energy domains probably play a more dominant role.

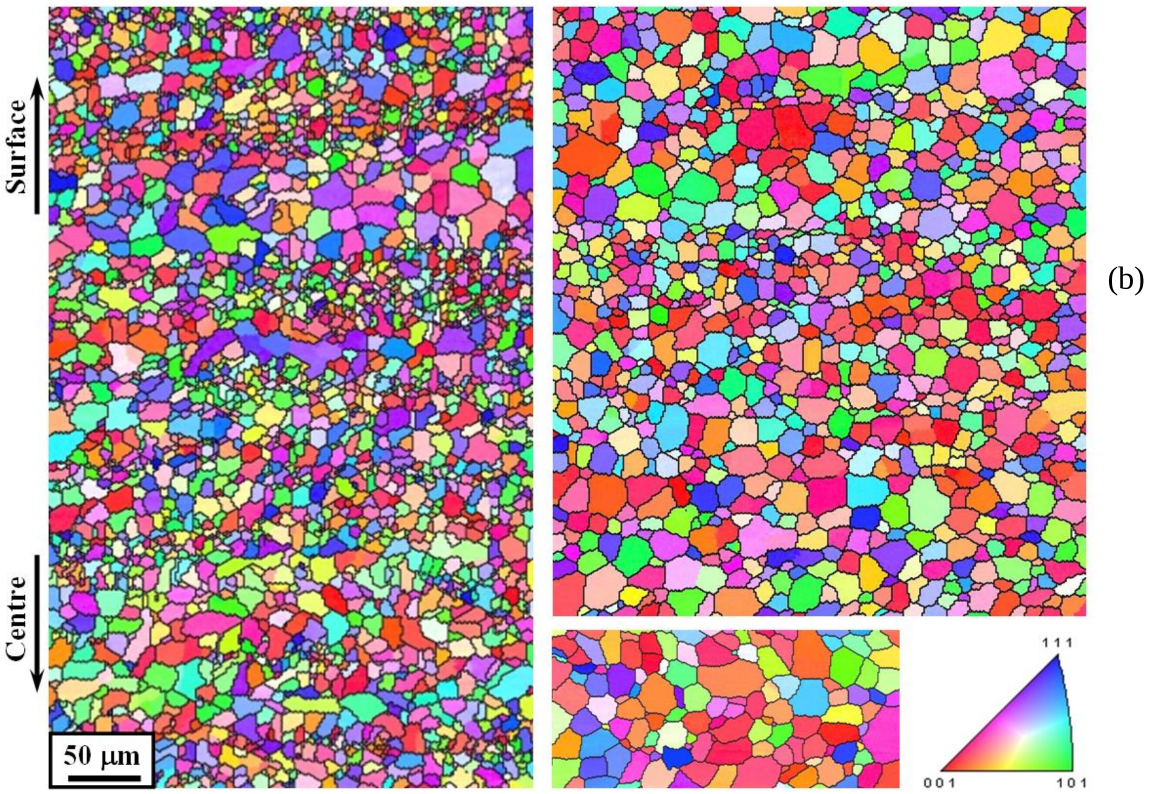

(a) (c)

Fig. 5.3. Inverse pole figure maps (TD-plane, the scale bar is || to RD) of Al-2.8Mg alloy recrystallized at 550°C for ~4 seconds after various rolling reductions: a) ~85.0% reduction; b) 96.9% reduction; c) 99.1 % reduction. The maps are of the same scale [2s].

Although the rolling textures after various rolling reductions in different Al alloys are qualitatively identical and only exhibit differences in intensity, the corresponding annealing textures may reveal significant differences. Commercially pure aluminum alloys account for a very strong cube component in the recrystallized state, whereas Si/Mg alloyed aluminum products (6xxx alloys) tend to reveal a more scattered cube along the θ-fibre, mixed with a {110}⟨122⟩ component (see Figs 5.1 and 5.2) [1, 2s]. Another example is the Al-2.8Mg alloy subjected to various rolling reductions (Figs. 5.3 and 5.4). Although the deformation textures are qualitatively identical, different RX textures tend to emerge after annealing and characterized by various degrees of rotation along the θ- fibre [9s, 17s]. The {001}⟨120⟩, {001}⟨130⟩, {001}⟨140⟩ components are typically observed after recrystallization the mentioned alloy. The conventionally observed cube component is scattered along the θ-fibre at a lower reduction (74%), whereas an increase of thickness reduction gives rise to an intensification of the texture around the ~ {001}⟨130⟩ component [9s, 17s]. It was shown that the intensities of observed P and Goss orientations do not change significantly with the amount of reduction, though the intensity of the Q ({013}⟨231⟩) orientation tends to rise with the increase of strain [9s]. The evolution of non-conventional texture components could be explained by means of numerical approaches.

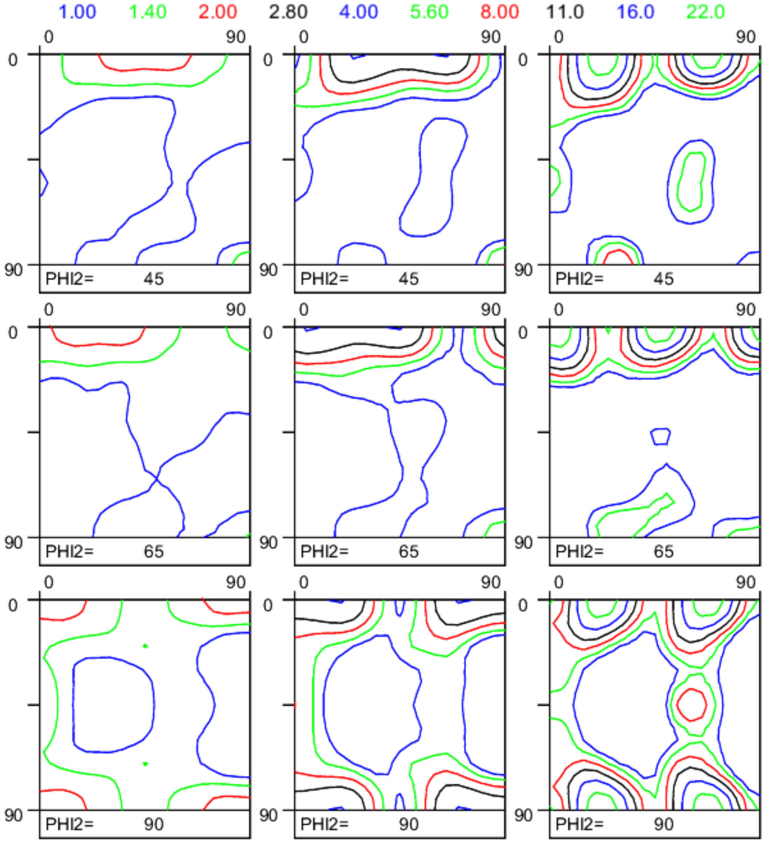

(a) (b) (c)

Fig. 5.4. Texture evolution in Al-2.8Mg alloy recrystallized at 550°C for ~4 seconds after various rolling reductions: a) ~85.0% reduction; b) 96.9% reduction; c) 99.1 % reduction [2s].

The strain path applied in cold rolling strongly affects both the microstructure and texture evolution during recrystallization. Fig. 5.5 shows microstructure evolution after various asymmetric rolling schedules. The evolved RX microstructures (Figs. 5.5 a and b) are relatively homogeneous with the exception of material rolled in three passes (Fig. 5.5 c). It is obvious that multi-pass rolling reduction does not account for grain refinement due to strain localization within the sub-surface region of a rolled sheet [1, 118]. The strong shear strain localization occurs at low values of the geometric shape factor and low thickness reductions. As a result, the RX microstructure of the asymmetrically rolled material in three passes of small reductions (Fig. 5.5c) is inhomogeneous and contains coarsened grains.

Generally, recrystallized ASR sheets reveal a finer recrystallized grain structure as compared to conventionally produced material [1, 40, 42, 96, 97, 119-124]. The grain refinement after asymmetric rolling is attributed to the additional shear deformation imposed during deformation, as it is described in [2s, 16s, 18s, 21s, 30s]. The larger amount of accumulated strain leads to an increased population of nuclei and thus fine-grained structures.

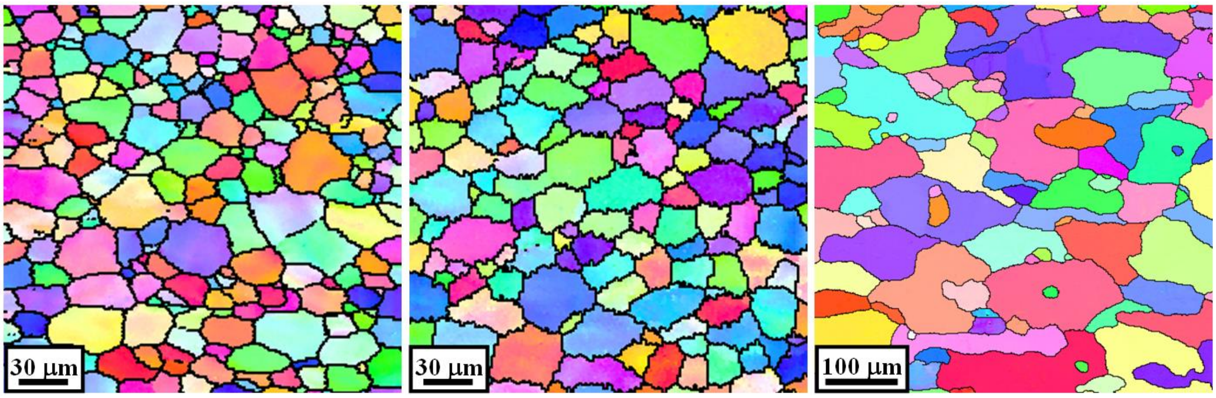

(a) (b) (c)

Fig. 5.5. Inverse pole figure maps with HAGBs (TD-plane, the scale bar is || to RD) of 6016 alloy recrystallized at 550°C/30s after various ASR processes: a) 20% thickness reduction in one pass with roll diameter ratio of 1.5; b) 41% thickness reduction in two passes (30%→17.5%) with roll diameter ratio of 1.5; c) multi-pass ASR (3.7% → 7.6% → 3.7%) with roll diameter ratio of 1.3 [2s].

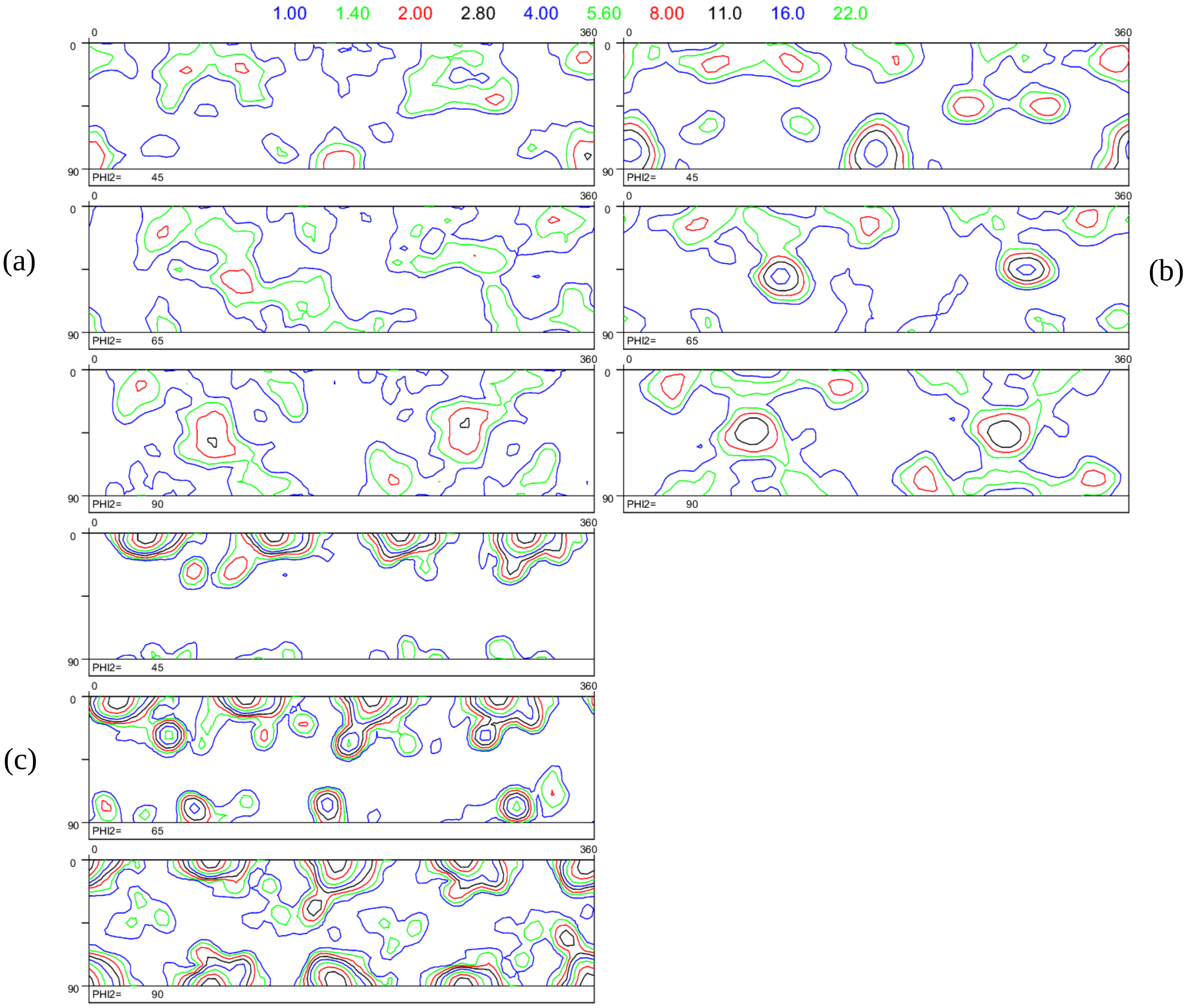

Fig. 5.6. Through-thickness recrystallization textures observed in 6016 Al alloy recrystallized at 550°C/30s after various ASR processes [2s]: a) 20% thickness reduction in one pass with roll diameter ratio of 1.5; b) 41% thickness reduction in two passes (30%→17.5%) with roll diameter ratio of 1.5; c) multi-pass ASR (3.7% → 7.6% → 3.7%) with roll diameter ratio of 1.3.

As it is described in [2s, 16s, 18s, 21s, 30s], in asymmetrically rolled materials displayed in Fig. 5.5, the shear-type texture of deformation is not retained during recrystallization at 550°C but instead, a weak non-conventional texture has developed (Figs. 5.6 a and b [2s]). Both 20% and 41% ASR rolled sheets reveal identical textures characterized with a 90° rotated Goss component (L-component) added with somewhat displaced shear texture orientations (H and γ-fibre components). The texture of material rolled in three passes (Fig. 5.6 c) differs both quantitatively and qualitatively from the ASR sheets rolled in one and two passes (Figs. 5.6 a and b). The recrystallization texture of the multi-pass ASR rolled sheet is dominated by a strong cube component (Fig. 5.6 c), while the recrystallization textures of the asymmetrically rolled sheets in one and two passes are much weaker and display a different group of orientations. The evolved texture of Fig. 5.6 c is identical to the ODF observed after small thickness reduction in symmetric rolling process (Fig. 5.2 c).

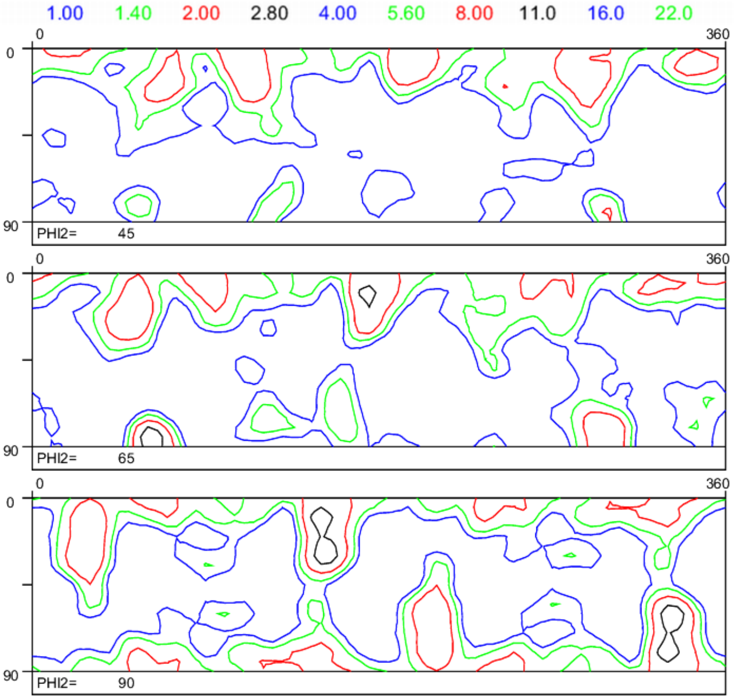

Fig. 5.7. ODF of 6016 alloy conventionally rolled with 70% thickness reduction and afterwards asymmetrically rolled with 18% reduction and recrystallized at 550°C for 30 seconds [2s].

The effect of strain path change, involved in cold rolling, on recrystallization texture is summarized in Fig. 5.7. A drastic change of the strain path during rolling tends to induce texture weakening in recrystallized material [16s]. The weakly developed textures spread around the θ-fibre together with weak retained rolling components are the main textural features of the material rolled first symmetrically and asymmetrically afterward. The same material subjected to identical thickness reduction (87%) in symmetric rolling produces a relatively strong RX texture with pronounced Goss, cube and P orientations (Fig. 5.2 b). Thus, it is summarized here that the strain path change in cold rolling has a tremendous effect on the final RX texture.

5.2 Recrystallization texture modeling

Crystal plasticity models enable analyzing the evolution of the deformation texture as well as estimating the dissipated plastic power in each crystal orientation during deformation. Additionally, the CP models offered a platform for a vast variety of RX models [9s, 15s, 125-132]. Modeling RX texture evolution is far more complex compared to the simulation of deformation textures since a particular local event in RX can give rise to significant long-range effects that may drastically affect the overall texture evolution. A typical example is abnormal grain growth occurring when a specific nucleus consumes the surrounding deformed or recrystallized matrix due to particular local events such as variant selection or solute drag of neighboring boundaries. Giving the complexity of the processes involved in RX the goal of building a comprehensive, accurate and relevant model for industrial application is of particular importance.

The evolution of recrystallization texture in complex structures such as particle-matrix systems could be calculated with the recrystallization model proposed in Refs. [9s, 15s]. This approach considers strain heterogeneities in the particle affected deformation zones (PADZ) by introducing different strain modes and assumes: (i) micro-growth selection via enhanced mobility of specific grain boundaries and (ii) orientation selection during nucleation based on the crystallographic dependence of the stored energy of plastic strain. A comprehensive description of the model is reported in Refs. [9s, 15s].

The essence of the RX approach developed by Sidor et al. [9s, 15s] is expressed by equations 5.1 and 5.2, whereby the nucleation $\hat{P}_n(g)$ and growth $\hat{R}$ operators applied on the experimental deformation texture $f_D(g)$ produce the calculated recrystallization texture $f_R(g)$:

$$F_{GP}(g) = \hat{R} f_D(g) \tag{5.1}$$

$$f_R(g) = \hat{P}_n(g) F_{GP}(g) \tag{5.2}$$

Growth selection is implemented in the model via equation 5.1 by attributing enhanced mobility to the nuclei exhibiting a particular orientation relationship with respect to the deformed matrix. In the current case, the growth operator $\hat{R}$ is represented by the frequently observed ⟨111⟩40° nucleus-matrix orientation relationship in FCC metals [2s, 15s, 114], expressed by 8 crystallographic variants of the ⟨111⟩40° axis-angle pair:

$$\hat{R} \equiv \langle 111 \rangle 40^{\circ} \tag{5.3}$$

The calculated growth potential texture $F_{GP}(g)$ by means of equations 5.1 and 5.3 represents crystals potentially favorably oriented for growth, provided these orientations are present in the nucleation texture. A nucleation selection is implemented in the computational algorithm by applying a nucleation operator $\hat{P}_n(g)$ on the growth potential texture $F_{GP}(g)$. The orientation selection suggested by equation 5.2 implies that from all the orientations with a potential for growth only the ones that have nucleated according to a specified nucleation law will appear in the recrystallized matrix.

In FCC metals, low stored energy nucleation is favored during recrystallization as it is reported by Etter et al. [115] and Baudin et al. [116]. According to Hutchinson [117], the energy stored in a particular crystal orientation as a result of plastic deformation could be approximated by the Taylor factor (TF) calculated e.g. by the full constraints Taylor theory [73]. Even though the TF, i.e. the instantaneous dissipated plastic power, neglects the deformation history, microstructural heterogeneities in the deformation matrix, and strain hardening phenomena, it still provides approximate information on the energy accumulated in differently oriented grains. By applying this hypothesis, the locally stored energy can be calculated for each particular strain mode ε involved in the deformation of the particle-matrix system. In the present approach the following nucleation operator was considered:

$$P_n^{\varepsilon}(g) = \left\{ \begin{array}{ll} 1 \quad \text{if} & \dfrac{M^{\varepsilon}(g) - M_{\min}^{\varepsilon}}{M_{\min}^{\varepsilon}} \in [0, c_1] \\ 0 & \text{for all other orientations} \end{array} \right\} \tag{5.4}$$

where $M_{\min}^{\varepsilon}$ is the absolute minimum TF value for a particular strain mode, which is referred to by the superscript ε and the constant c_1 is a model parameter.

The model of Sidor et al. [7s, 9s, 15s] suggests that the recrystallization texture consists of combined contributions corresponding to local strain modes. The characteristic texture $f_R^{\varepsilon}(g)$ for each specific strain mode ε is the result of micro-growth selection and oriented nucleation mechanisms. The simulated overall RX texture $f_R(g)$ is subsequently obtained as the weighted average of the considered $f_R^{\varepsilon}(g)$ orientation distribution functions:

$$f_R(g)=\sum w_\varepsilon P_n^\varepsilon(g)F_{GP}(g)=\sum w_\varepsilon f_R^\varepsilon(g) \tag{5.5}$$

where the weight factors w_ε ($\sum w_\varepsilon = 1$) correspond to the volume fraction of crystals that were deformed according to strain mode ε.

The role of the microstructural sites that give rise to randomly oriented grains is taken into account in the RX model by adding a fraction w_{rand} of randomly oriented grains $f_{rand}(g)$ to the recrystallization texture of eq. 5.5, producing the following expression:

$$f_R(g)=\sum w_\varepsilon f_R^\varepsilon(g)+w_{rand}\, f_{rand}(g) \tag{5.6}$$

with $\sum w_\varepsilon + w_{rand} = 1$.

Growth potential textures (GPT) derived from the corresponding deformation textures by equation 5.1 are shown in Fig. 5.8 for the individual materials after different reductions (see Ref. [9s] for details). The calculated GPT textures are in a good qualitative agreement with the experimentally measured annealing textures of Fig. 5.4.

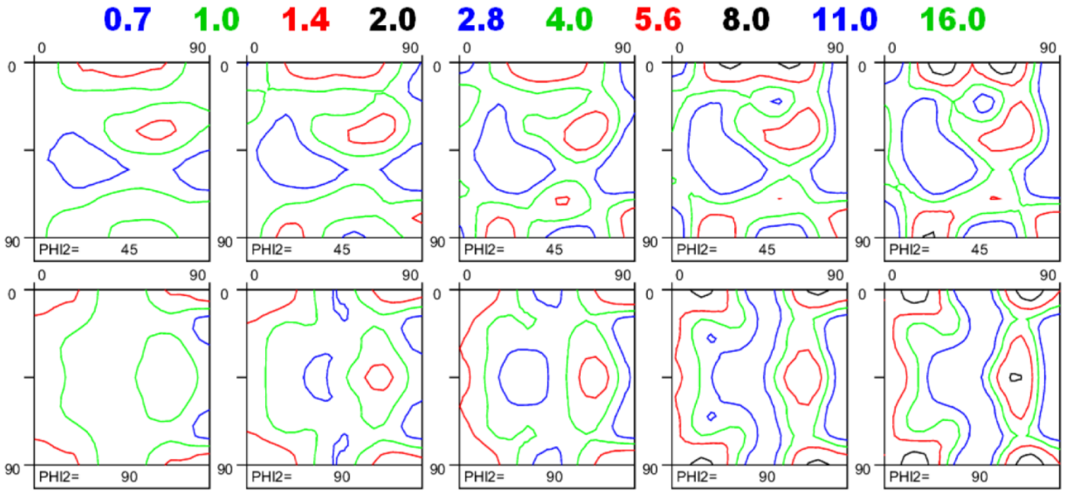

(a) (b) (c) (d) (e)

Fig.5.8. Growth potential textures derived from the corresponding experimentally measured deformation textures of Al-2.8%Mg alloy after various reductions [9s]: a) 74%, ID_N=0.07; b) 85%, ID_N=0.14, c) 96%, ID_N=0.37; d) 97%, ID_N=0.25, e) 99.1%, ID_N=0.56. The ID_N-*s* are calculated between the growth potential ODFs and experimentally measured RX textures.

The low values of calculated ID_N numbers for materials rolled with 74 and 85% reductions (Figs. 5.8 a and b) support the argument for micro-growth selection in recrystallization, although this mechanism alone is not capable of explaining the evolution of the RX texture after higher thickness reductions (96% - 99%) as the GPT textures (Figs. 5.8 c-e) reveal both quantitative and some qualitative deviations with respect to the experimentally measured counterparts (Fig. 5.4).

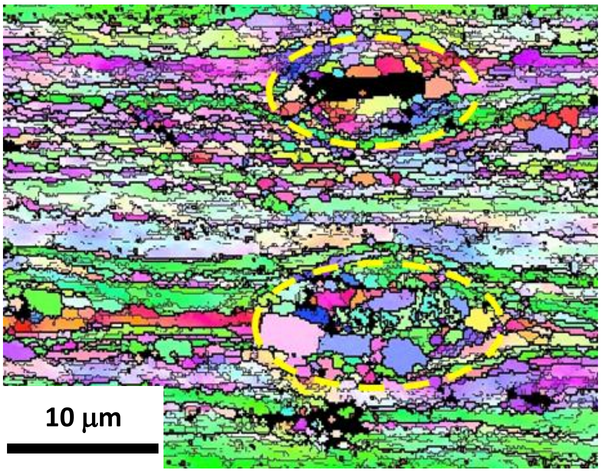

Fig. 5.9. EBSD orientation contrast map of partially recrystallized aluminum after annealing at 360 °C for 1 min (TD-plane, the scale bar is || to RD). The nucleation is observed in the vicinity of large non-deformable particles within PADZ.

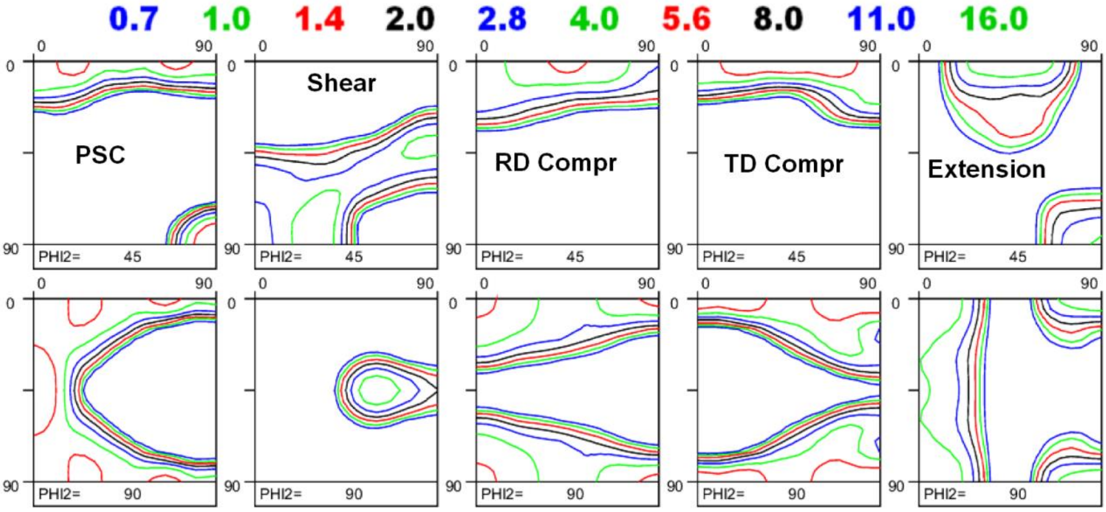

(a) (b) (c) (d) (e)

Fig. 5.10. Calculated ODFs for individual strain modes by eq.5.5 assuming low stored energy nucleation with c_1=0.258 [9s]: a) RX texture produced by PSC; b) RX texture produced by shear; c) RX texture produced by compression with essential RD strain; d) RX texture produced by compression with essential TD strain; e) RX texture produced by extension.

In addition to published results [133], the conducted FEM calculations [9s] show that the particle affected deformation zone is very heterogeneous in terms of strain distribution caused by a variety of strain modes and strain localization. The highly stained regions lead to a well-known mechanism of recrystallization, called particle-stimulated nucleation (PSN). The first recrystallized nuclei appear in the vicinity of the large particles via PSN (see Fig. 5.9). In the current RX model the strain state outside the PADZ is approximated by plane strain compression (PSC) (e_{11}=-e_{33}, e_{ij}=0) whereas the PADZ is approximated with the following simplified strain modes: (i) compression along the normal direction (ND) with essentially RD elongation ($e_{11}/e_{22}/e_{33}$=0.7/0.3/-1 and e_{ij}=0 for i≠j), (ii) compression along the ND with essentially TD elongation ($e_{11}/e_{22}/e_{33}$=0.15/0.85/-1 and e_{ij}=0 for i≠j), (iii) near uni-axial extension along the rolling direction ($e_{11}/e_{22}/e_{33}$=1/-0.32/-0.68, e_{ij}=0 for i≠j), (iv) shear along RD (e_{13}) at the edge of the particle. Orientation selection based on the crystallographic dependence of stored energy by means of equations 5.2 and 5.5 allows revealing the nature of the RX components characteristic for various strain modes involved. As shown in Fig. 5.10a the appearance of the <001>//ND fibre and the Goss component in the material after 74% reduction could be attributed to the nucleation in the bulk of the material deformed by PSC, assuming low stored energy nucleation (c_1=0.258). The P orientation and the γ-fibre components conceivably are produced by shearing of the matrix in the vicinity of particles (Fig. 5.10 b), whereas the cube orientations rotated along the RD and ND directions can be attributed to extension and two considered compression modes (Fig. 5.10 c-e).

Crystallographically resolved orientation selection based on a low stored energy nucleation mechanism is implemented in the model by equation 5.4, whereby the stored energy of individual crystal orientation is approximated by the instantaneous plastic power, which was calculated by the FCT crystal plasticity theory. The constant c_1 in equation 5.4 is fitted in a way that all crystals, irrespective of the strain mode, comply with the low stored energy criterion. It implies that a spectrum of orientations with a normalized TFs between 0 and c_1 (eq. 5.4) will produce nuclei which can potentially grow. In the RX model [9s, 15s] the parameter c_1 was optimized by a meticulous comparison of the calculated TF distributions with the ensuing recrystallization textures for various strain modes. It was found that for 6016 alloys of different hot band textures and rolled with 85-87% reduction the constant value of c_1=0.258 ensures a satisfactory agreement between the calculated and experimental RX textures [15s].

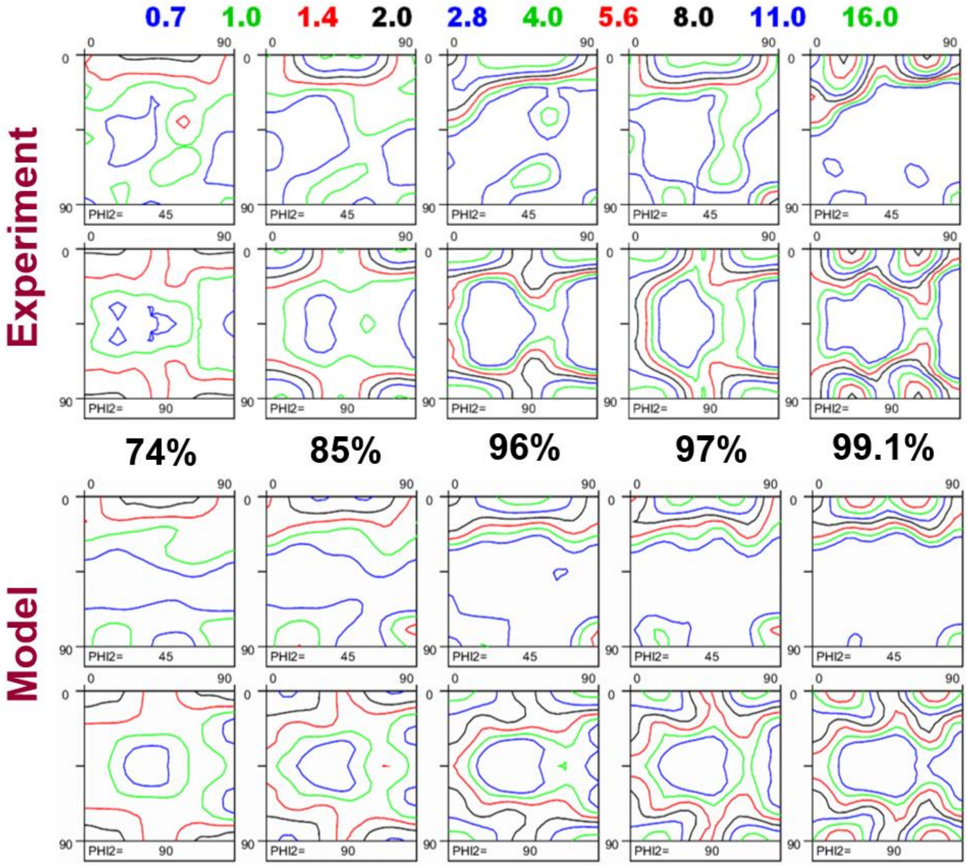

Fig. 5.11 [9s]. Experimentally observed ODFs in Al-2.8%Mg alloy after various rolling reductions and simulated recrystallization textures with equation 5.6.

A further quantitative improvement could be achieved by fine-tuning the characteristics of the nucleation events. As partitioning of the macroscopic deformation takes place in particle-containing materials, the simulation of the overall RX texture with equation 5.6 requires attributing a weight factor to each strain mode involved in the local strain repartition. The weight factors w_ε should correspond to the volume fractions of grains that were deformed according to the considered strain modes. Since the volume fraction of non-deformable particles is related to the fraction of nuclei appearing in their vicinity, the volume fraction of crystals generated by PSN could be approximated by relating the size of the particle to the geometry of PADZ, as it is described in [9s, 10s, 15s].

The recrystallization textures of Figs. 5.11 and 5.12 were computed by equation 5.6 assuming that: (i) nucleation of recrystallization occurs in low stored energy domains (ii) the bulk of the material is shaped by plane strain compression, (iii) the strain mode in the PADZ could be approximated by simplified strain modes such as two types of compression mode, shear and extension (iv) the nuclei produced by microstructural heterogeneities such as shear/deformation bands are of random nature [9s, 15s]. The simulated textures of Figs. 5.11 and 5.12 reasonably resemble the main features of the corresponding experimental counterparts.

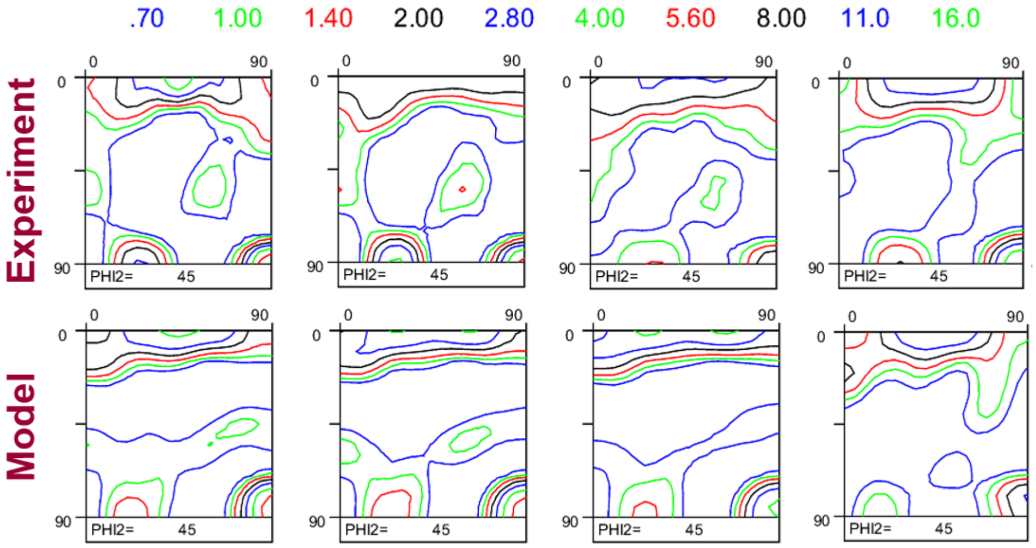

Fig. 5.12. Experimentally observed ODFs in 6016 Al alloys after ~85-87% thickness reductions and simulated counterparts with equation 5.6. Detailed description of modeling procedure can be found in [9s, 10s, 15s].

6. Plastic anisotropy: experiment and modeling

Understanding and controlling the texture evolution via TMP is important since texture development introduces anisotropy on the macroscale which, in turn, affects a large variety of practical applications. A critical assessment of the main sources of anisotropy in metals is discussed in detail by Hutchinson [134]. The conventional measure of plastic anisotropy is the Lankford value (*r*-value) measured for various angles (usually 0°, 45° and 90°) with respect to rolling direction. The average parameters of the normal and planar anisotropy are expressed by the $\bar{r}$ and the Δr values, respectively [2s, 7s, 16s, 18s, 50, 51]:

$$r=\frac{e_{22}}{e_{33}};\ \bar{r}=\frac{(r_0+2r_{45}+r_{90})}{4};\ \Delta r=\frac{(r_0-2r_{45}+r_{90})}{2} \qquad (6.1)$$

where indexes 2 and 3 of the true strain *e* refer to TD and ND, respectively.

To ensure the enhanced level of deep drawability, the material should reveal a high *r*-value whereas the in-plane anisotropy should be minimized. Crystal plasticity calculations, enabling investigating the effect of texture characteristics on the measures of plastic anisotropy, provide valuable information facilitating proper material's design.

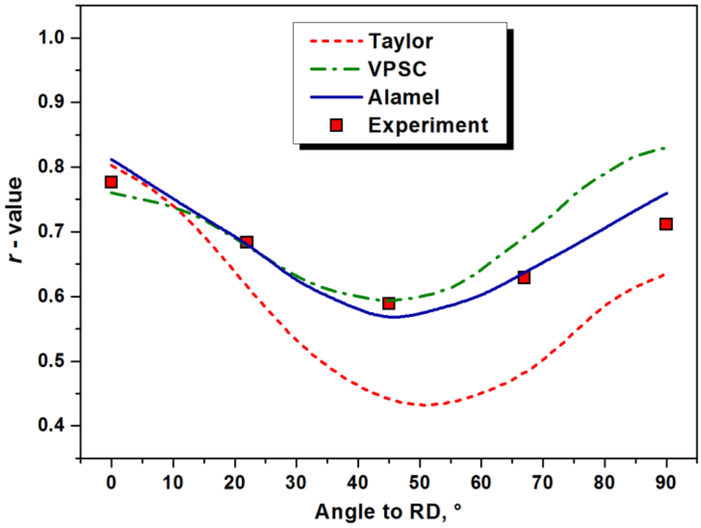

Fig. 6.1. Measured and calculated Lankford profiles with various CP approaches for 6016 alloy [7s]. The corresponding texture is shown in Fig. 6.2a.

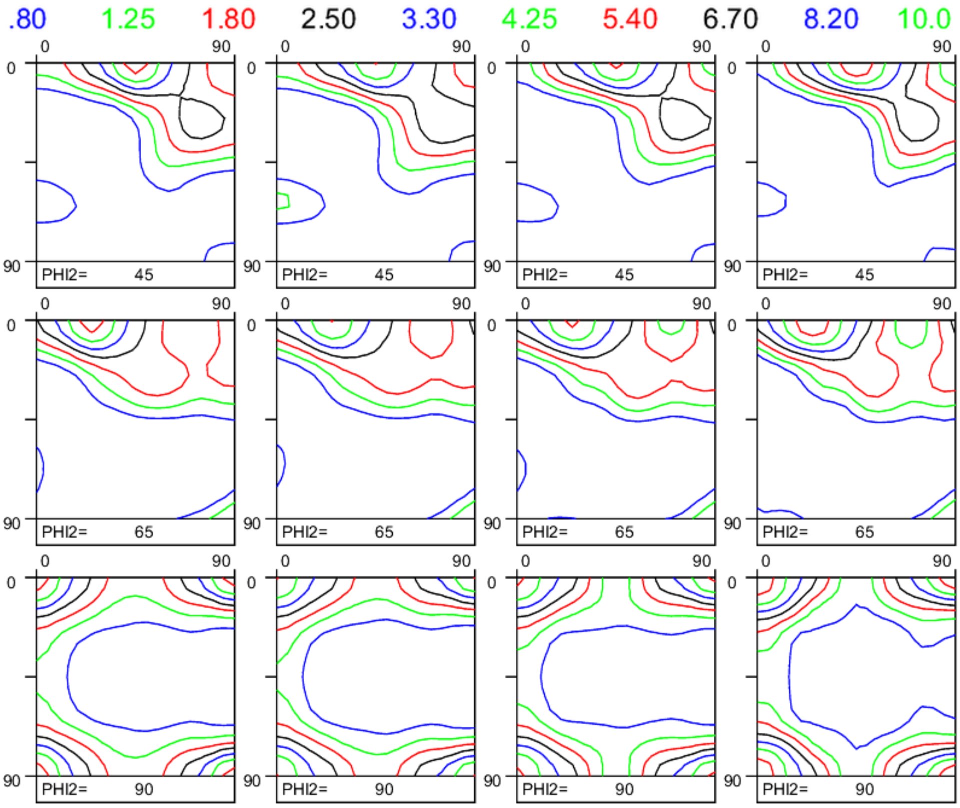

(a) (b) (c) (d)

Fig. 6.2. Through-thickness RX textures of 6016 alloy calculated for various number of grains [7s]: a) 24300 grains; b) 13500 grains; c) 5400 grains; d) 2700 grains.

Fig.6.1 presents both measured and calculated Lankford values for 6016 alloy with the texture of Fig. 6.2a [7s]. It is evident that the *r*-value is highly anisotropic, i.e. dependent on the direction of the tensile sample axis. The RX texture evolved during annealing (Fig.6.2 a) accounts for a V-type Lankford value profiles with a minimum at a 45° with respect to RD.

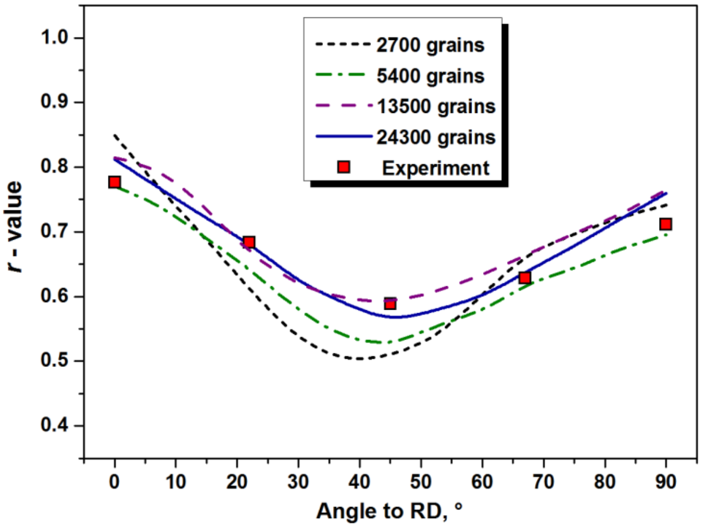

Fig. 6.3. Effect of grain statistics on the quality of *r*-profile simulations accomplished by the Alamel model [7s]. The corresponding textures are presented in Figs. 6.2 a-d.

The employed CP models predict the *r*-profile with various degrees of accuracy (Fig.6.1). Since the normal anisotropy is measured at relatively low strain, the Alamel model, employing a short-range grain interaction, serves to produce the most accurate correspondence between the calculated and measured values. It should be underlined that the quality of *r*-value prediction depends on the choice of representative volume element (RVE), independently of the choice of CP approach [7s]. Fig. 6.2 a shows the texture calculated from ~24300 grains. This ODF was computed by merging 9 EBSD maps (~2700 grains per map), each covering the entire thickness of a sheet. In order to ensure randomly selected data sets, the EBSD maps were collected from four specimens cut from different locations in the investigated material. Since the Alamel model provides a very satisfactory agreement between the calculated and experimentally measured *r*-profiles (Fig.6.1), this approach was employed to reveal the effect of grain statistics on the quality of *r*-profile simulations (Fig. 6.3). The ODFs corresponding to the calculated Lankford curves of Fig.6.3 are presented in Fig. 6.2 b-d. Fig.6.3 shows that the RVE represented by a low number of grains (2700 and 5400) accounts for significant discrepancies between the measured and calculated *r*-profiles while the accuracy of prediction tends to improve with increasing the number of grains in the RVE. In order to exclude the effect of texture heterogeneity on the results of *r*-value simulation, the quantitative difference among the ODFs should be estimated.

Considering the texture with the largest total number of grains (Fig. 6.2a) as a reference, the degree of heterogeneity could be estimated between the reference ODF and the textures, containing less grains (Figs. 6.2b-d), by calculating the ID_N numbers. The texture differences computed for ODFs of Figs. 6.2b-d (ID_N(13500 grains)=5.6·10^{-3}, ID_N(5400 grains)=3.1·10^{-3}, ID_N(2700 grains)=1.2·10^{-2}) with respect to the reference texture of Fig.6.2a indicates that the level of heterogeneity in the investigated sample is negligibly small.

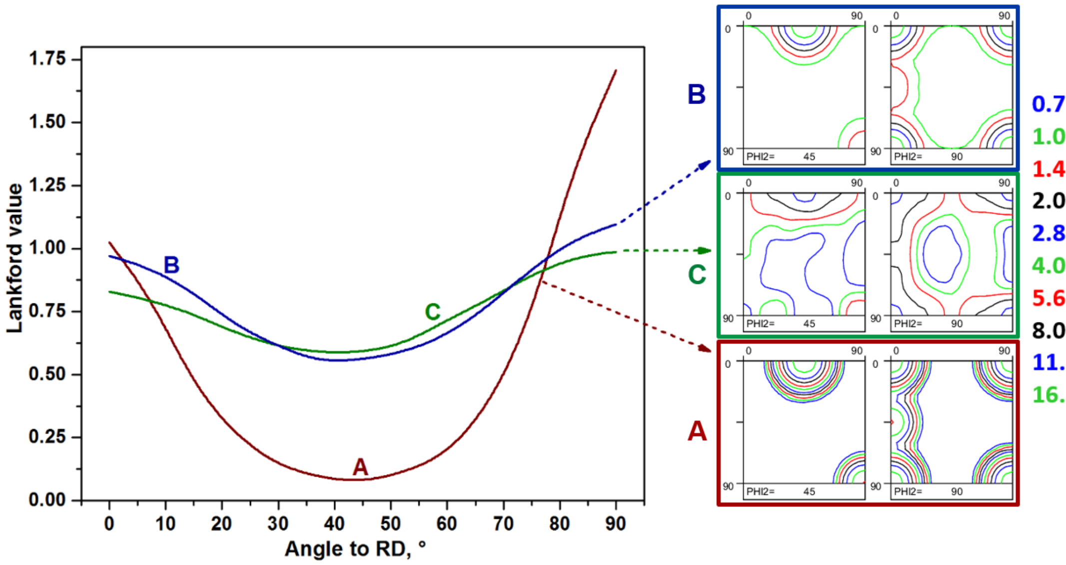

Fig.6.4. Simulated *r*-value profiles with the Alamel model for three hypothetical textures A-C [24s].

Various RX modeling approaches [9s, 15s, 126, 131, 132] are based on orientation selection or determination of nucleation spectra, considering the diversity in the dissipation of plastic power in different crystal orientations. This is of particular importance while investigating the effect of microstructural heterogeneities on the evolution of recrystallization texture. The evolution of nucleation spectra in the bulk of a material as well as at micro shear bands [8s, 14s] or in the particle affected deformation zone might be explained by RX models considering both basic principles of micromechanics and crystal plasticity approaches [7s-9s, 15s]. Accounting for strain path heterogeneities in the vicinity of non-deformable inclusions allows explaining the appearance of the P {011}<233>, {100}<130> or weak γ-fibre <111>//ND orientations, which typically evolve in particle-containing Al alloys [9s, 15s]. Likewise, considering strain path deviations inside the copper-type shear bands from the macroscopic one sheds light on the evolution of P, Goss {011}<100> and Q {013}<231> orientations [8s, 135]. The evolution of mentioned texture components has a decisive influence on anisotropy of plastic strain ratio. Fig. 6.4 reveals the effect of various hypothetical RX textures on the anisotropy of plastic yielding.

First, the *r*-value profile of a material, characterized by a strong Cube {001}<100> mixed with a weaker Goss texture, is examined (Fig. 6.4, texture A). This type of texture often dominates in Al-alloys [1, 2s, 18s, 51, 113, 118] after recrystallization and tends to produce a V-shaped *r*-profile with a local minimum at ~45° with respect to RD (Fig. 6.4 [24s], Lankford profile A). The estimated normal anisotropy for the A-type texture ($\bar{r}$=0.72) might ensure a minimum level of deep drawability, however, the high value of in-plane anisotropy (Δr=1.29) makes this material inappropriate for deep drawing.

In an ideal case, the in-plane anisotropy should be minimized to zero and this can be accomplished by texture randomization. Taking into consideration that it is almost impossible to produce an isotropic material with a random texture, it is assumed here that the strongly textured material A is partially randomized and as a result, a B-type texture is evolved, consisting of a weakly developed Cube and Goss components (Fig. 6.4, texture B). The A and B-type textures are qualitatively identical, while the quantitative diversity accounts for significant changes in Lankford profiles. Even if the normal anisotropy of B-type texture ($\bar{r}$=0.8) did not improve drastically as compared to the A-type counterpart, the planar anisotropy (Δr=0.47) reveals considerable improvement. It is evident that even after severe texture randomization the *r*-value is still anisotropic, i.e. dependent on the direction of the tensile sample axis. It should be mentioned, that during TMP, the evolution of a particular texture component occurs at the expense of other orientations. For instance, the evolution of Cube-oriented grains, which dominate in Al alloys after recrystallization, can be suppressed by activating nucleation at microstructural heterogeneities (shear bands) or via particle stimulated nucleation mechanism. Each nucleation phenomenon produces a characteristic orientation spectrum, as noted previously. Since texture weakening caused either by PSN or via nucleation at shear bands is not of random nature [8s, 9s, 14s], it is assumed that the A-type texture is randomized by the P, Q, weak γ-fibre and components scattered around these orientations. The resulting C-type texture (Fig. 6.4) serves to produce a V-shaped *r*-value profile with $\bar{r}$=0.75 and Δr=0.32. Even though the normal anisotropy remains far below the desired value of $\bar{r}$=1, the planar anisotropy seems to be acceptable for deep drawing. Fig. 6.4 clearly demonstrates that the presence of orientations, originating from microstructural heterogeneities (P and Q) which evolve at the expense of components evolved in the bulk of a material, leads to a decrease in planar anisotropy while the value of normal anisotropy does not improve significantly.

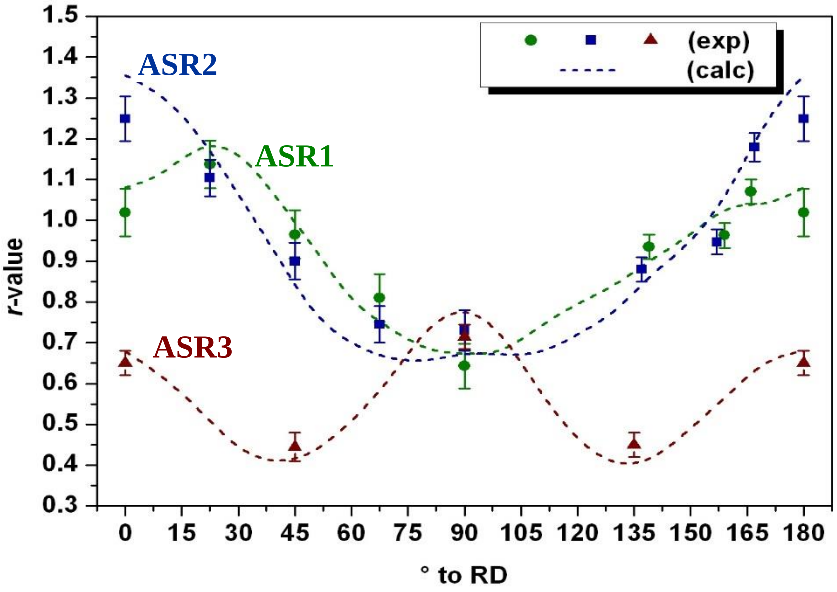

Fig. 6.5. Experimentally measured and calculated Lankford value profiles with the ALAMEL model for asymmetrically rolled and recrystallized materials [18s]: ASR1 – 20% thickness reduction, ASR2 – 41% reduction, ASR3 – 20% reduction in three rolling passes. The corresponding annealing textures are shown in Fig.5.6.

The normal anisotropy conventionally measured in a tensile test at three angles, *i.e.*, 0°, 45°, and 90° with respect to rolling direction, provide incomplete information on the plastic anisotropy since the in-plane *r*-value distribution displays a non-symmetric character in the asymmetrically rolled sheets ASR1 and ASR2, as it is shown in Fig. 6.5. In this case, the *r*-profile should be determined in the range from 0° to 180° and the average measure of the normal anisotropy is calculated by a trapezoidal rule from the profile of *r*-values calculated or measured at angle x_i:

$$\bar{r} \approx \frac{1}{x_n - x_0} \int_{x_0}^{x_n} r(x)dx \approx \frac{1}{2n}\left(r(x_0) + 2r(x_1) + 2r(x_2) + ... + r(x_n) \right) \tag{6.2}$$

Equation (6.2) is valid for a uniform grid, whereas if the experimental data are measured with a non-constant increment of the angle, then the total angle interval should be split into smaller subintervals, and then the trapezoidal rule can be applied on each of them with a variable trapezium width as follows [18s]:

$$\bar{r} \approx \frac{0.5}{x_n - x_0} \sum_{i=1}^{n} (x_i - x_{i-1})\left(r(x_i) + r(x_{i-1}) \right) \tag{6.3}$$

As was shown in Refs. [2s, 18s], the recrystallization texture in the asymmetrically rolled materials is considerably weaker than that of conventionally rolled ones and therefore, these materials exhibit *r*-values ($\bar{r}$ ≈ 0.9) which are comparable to randomly textured material ($\bar{r}$

=1). It was also revealed that the displaced shear texture components and a 90° rotated Goss component, observed in the asymmetrically rolled and recrystallized materials, produce significantly improved *r*-value in the 0° and 45° tensile directions while conventionally rolled sheets show an inverse tendency. It is evident from Fig. 6.5 and Tab. 6.1 that the rolling reduction in the ASR does not affect the normal anisotropy significantly and the multi-pass ASR process with the roll diameter ratio of 1.3 produces *r*-profile, which resembles many features of conventionally rolled sheets.

Alternatively to eqs. 6.2 and 6.3, an effective normal anisotropy r_{eff} could be computed based on the width to elongation ratios, *i.e.*, *q*-values ($q_x=r_x/(1+r_x)$), predicted at angles *x* [50]:

$$r_{eff}=\frac{\overline{q}}{(1-\overline{q})} \tag{6.4}$$

where $\overline{q}$ is calculated by employing either equation 6.2 or 6.3.

In the present study, the planar anisotropy is characterized by a Δq-value since it is normalized in the range of $0<q<1$, while the conventional measure of the in-plane anisotropy Δr is defined in the infinite range $0<\Delta r<\infty$. A simple measure of Δq is introduced [50] as the difference between the maximum and minimum *q*-values:

$$\Delta q=q_{max}-q_{min} \tag{6.5}$$

The calculated Δq values are more representative as compared to the Δr values. For instance, materials ASR1 ($\Delta r=-0.14$) and ASR2 ($\Delta r=0.08$) have similar *r*-profiles while displaying completely different Δr values, however, the Δq-value are comparable (Δq(ASR1)$=0.14$ and Δq(ASR2)$=0.13$).

Table 6.1. Comparison between measured anisotropy values and calculated ones with the Alamel model [18s].

Material	**measured**				**calculated**			
	$\overline{r}$	r_{eff}	$\overline{q}$	Δq	$\overline{r}$	r_{eff}	$\overline{q}$	Δq
ASR1	0.91	0.89	0.47	0.14	0.94	0.95	0.49	0.14
ASR2	0.93	0.91	0.48	0.13	0.94	0.93	0.48	0.18
ASR3	0.57	0.56	0.36	0.11	0.58	0.57	0.36	0.16

Results of current crystal plasticity simulations clearly indicate that the average Lankford value and the planar anisotropy could be derived from the texture of a material evolved during TMP. However, it should be emphasized that the plastic strain ratio is a result of a complex interaction among numerous texture components constituting the polycrystalline aggregate. This implies that even small texture modification, induced by TMP, is capable of changing the extent of both normal and planar anisotropy in a material.

7. Summary

1. Results of numerous experimental observations, presented in this work, clearly indicate that the conventional cold rolling process tends to produce a complex-shaped β-fibre in Al alloys, independently of the straining level, number of passes and initial texture. Both the intensity and intensity distribution along the β-fibre depends on the nature of the process, chemical composition and pre-rolling texture of materials.
2. The strain mode applied in rolling strongly affects the evolution of deformation texture. Combinations of plane strain compression and simple shear, as a result of different circumferential velocities of the upper and the lower rolls, result in rotation of the conventional rolling texture towards the shear texture components, while the intensity of the developed orientations depend on the amount of strain imposed during the asymmetric rolling process (ASR).
3. The performance of various crystal plasticity models was tested on Al alloys with FCC crystal structures subjected to a variety of strain modes. It was concluded that more accurate texture simulations, should be tilted toward (i) implementation of strain heterogeneity, involved in the deformation process, and (ii) considering grain interaction phenomena. Analyzing the quality of texture predictions indicates that application of continuum mechanics-based approximation of deformation, which accounts for strain heterogeneities evolved across the thickness of a rolled sheet, tends to improve the accuracy of crystal plasticity simulation. The analytical flow line model (FLM) employed in combination with a particular crystal plasticity model is capable of providing texture prediction comparable to one simulated with the strain path obtained from the finite element simulation (FEM). The developed simplified geometric model combined with crystal plasticity approaches provides an accurate prediction of the overall texture, however, this simple model is not efficient in capturing the evolution of texture with a high degree of accuracy in the individual through-thickness layers. Careful analysis of both FEM and FLM model outputs concludes that the FLM model parameters are directly correlated to the roll gap geometry and friction coefficient. Analytical expressions for the determination of FLM model parameters were developed, which ensures the practical implementation of this approach without fitting parameters. Results of texture simulations likewise show that the texture heterogeneities in a rolled material tend to evolve due to both (i) unequal deformation flow across the thickness and (ii) heterogeneous nature of pre-rolling texture.

4. Conventional cold rolling and subsequent short time annealing account for the development of Cube-Goss-dominated texture. Both deformation and recrystallization textures developed in the single-pass ASR process are considerably weaker in comparison to the ones obtained by conventional rolling and multi-pass ASR processes. In severely deformed particle-containing Al alloys, recrystallization is majorly governed by nucleation at strain heterogeneities, caused by the presence of non-deformable inclusions. The deformation flow around the hard and non-plastic phases is responsible for the appearance of non-conventional annealing texture components, which tend to evolve due to particle stimulated nucleation.
5. A new recrystallization model was developed, which enables analyzing the evolution of texture, based on principles of continuum mechanics and crystal plasticity theory. The results of this study demonstrate that after various degrees of rolling reduction the corresponding recrystallization textures show significant qualitative and quantitative differences with respect to each other. The differences in the recrystallized textures are explained by competitive nucleation at various nucleation sites. Recrystallization textures can be successfully simulated in view of: (i) strain mode heterogeneities in the particle affected deformation zone, (ii) nucleation selection criterion related to low stored energy nucleation and (iii) orientation growth selection associated with high mobility of <111>40° oriented boundaries.
6. Both crystal plasticity simulations and results of texture measurements clearly indicate that anisotropy of plastic strain ratio is strongly correlated with the textures evolved during the final annealing process. Both, normal and in-plane anisotropy are conditioned by the texture intensity and the volume fraction of recrystallization texture components.
7. The conventionally produced Al alloys with Cube-Goss-P type texture reveal V-shaped *r*-value profiles, however, results of crystal plasticity calculations clearly demonstrate that the presence of orientations, originating from microstructural heterogeneities which evolve at the expense of components evolved in the bulk of a material, leads to decrease in planar anisotropy while the value of normal anisotropy does not improve significantly. In asymmetrically rolled materials, the monoclinic sample symmetry ensures a non-conventional asymmetric *r*-profile. The recrystallization texture issued from the asymmetric rolling process improves the average Lankford value, whereas the in-plane anisotropy does not benefit significantly from this process. The *r*-value profiles can be accurately reproduced by crystal plasticity models, employing a short-range grain interaction, on condition of reliable grain statistics. For successful simulation, the representative volume element should contain approximately 20000 grains.

8. New Scientific Results, Theses

1. Analytical description of rolling texture in FCC metals

All known texture fibres, which evolve in thermomechanical processing of Al alloys, have an exact description in terms of Miller indices, except of a complex shaped β-fibre, which tends to develop during rolling in metals with FCC crystal structure. For many decades, this fibre was defined as a skeleton line connecting the copper, S and brass components in Euler space without a unified description of components belonging to the given orientation chain. A precise crystallographic description of the β-fibre is presented and the derived expression allows analyzing a deviation of the evolved deformation texture with respect to the analytically described counterpart, revealing the true nature of deformation process.

2. Computationally efficient modeling strategy for simulation of deformation textures

There is a broad spectrum of computational methods allowing simulation of texture evolution during deformation processes. Crystal plasticity finite element model (CPFEM) is the most comprehensive approach, which provides detailed information on microstructure and texture evolution, however, this approach requires enormous computational power. The crystal plasticity models, which employ various homogenization schemes, are far more efficient in terms of texture modeling compared to CPFEM. In the present work, the performance of various crystal plasticity models was tested on Al alloys subjected to a variety of strain modes and it was shown that more accurate texture simulations, should be tilted toward (i) implementation of strain heterogeneity, involved in the deformation process, and (ii) considering grain interaction phenomena. The results of simulations performed suggest that both the simple geometric approach and the analytical flow line model developed in combination with an arbitrary crystal plasticity approach are capable of providing accurate texture predictions, which are comparable to one simulated with the strain path obtained from the finite element simulation.

3. Crystallographic aspect of conventional and non-conventional technologies

Deformation textures emerging after accumulative roll bonding and severe rolling reductions reveal an evolutionary pattern, which resembles many features of conventional rolling, whereas the diversity in texture intensity and distribution of components along the characteristic fibres are related to the degree of straining level, chemical composition, pre-rolling texture and characteristic nature of roll gap geometry of each path. In asymmetrically rolled materials, where the amount of shear component is significantly higher compared to conventional rolling, the traditional rolling texture tends to rotate towards the shear texture components, while both the intensity and sharpness of the developed orientations depend on the amount of shear imposed during the process. Independently of reduction degree, conventional cold rolled and recrystallized Al alloys reveal Cube-Rotated Cube-Goss-P type dominated textures, whereas these components are replaced by significantly weaker ones, which are scattered around the α, θ and γ-fibres. In severely deformed particle-containing Al alloys, recrystallization is majorly governed by nucleation at strain heterogeneities, caused by the presence of non-deformable inclusions.

4. Modeling the Recrystallization textures

A new recrystallization model was developed, which implements crystallographically resolved orientation selection based on a low stored energy nucleation mechanism. Recrystallization textures in Al alloys can be successfully simulated in view of: (i) strain mode heterogeneities, triggered by the presence of hard non-deformable particles, (ii) nucleation selection criterion related to low stored energy nucleation and (iii) orientation growth selection associated with high mobility of favorably oriented boundaries.

5. Assessment of plastic strain ratio

Comparing the results of experimental evidence to crystal plasticity calculations clearly indicates that anisotropy of plastic strain ratio is strongly correlated to the texture evolved during the final annealing process. The conventionally produced Al alloys reveal V-shaped *r*-value profiles, whereas the presence of microstructural heterogeneities tends to decrease the degree of planar anisotropy. The asymmetrically rolled and recrystallized materials show asymmetric Lankford value profiles with the improved value of normal anisotropy while the in-plane anisotropy does not benefit significantly from this novel process. The anisotropy of plastic strain ratio can be successfully reproduced by crystal plasticity calculation with a representative volume element containing approximately 20000 grains.

References

Note: Literature sources numbered as [xs] are (co)-authored by Jurij Sidor (self-citations).

[1] Engler, O., Hirsch, J. Texture control by thermomechanical process using of AA6xxx Al–Mg–Si sheet alloys for automotive applications—a review, Mater Sci Eng A 336 (2002) 249–262.

[2s] Sidor, J., Petrov, R., Kestens, L. “Texture Control in Aluminum Sheets by Conventional and Asymmetric Rolling” in Comprehensive Materials Processing. Editor in Chief: Hashmi, S. Elsevier Science & Technology. Vol. 3.17, 2014, 447-498.

[3s] Sidor, J.J. Assessment of Flow-Line Model in Rolling Texture Simulations. Metals. 2019, 9(10), 1098, 21 pages.

[4s] Sidor, J.J. Deformation texture simulation in Al alloys: continuum mechanics and crystal plasticity aspects. Modelling and Simulation in Materials Science and Engineering. Vol. 26, nr. 8, 2018, 085011.

[5s] Xie, Q., Van Bael, A., An, Y.G., Lian, J., Sidor, J.J. Effects of the isotropic and anisotropic hardening within each grain on the evolution of the flow stress, the r-value and the deformation texture of tensile tests for AA6016 sheets. Materials Science and Engineering A. 721, 2018, 154-164.

[6s] Shore, D., Kestens, L.A.I., Sidor, J., Van Houtte, P., Van Bael, A. Process Parameter Influence on Texture heterogeneity in Asymmetric Rolling of Aluminium Sheet Alloys. Int. Journal of Mater. Forming. 11(2), 2018, 297-309.

[7s] Sidor, J.J., Petrov, R., Xie, Q., Van Houtte, P., Kestens L. Evaluation of crystallographic changes and plastic strain ratio in Al alloys. Mater. Science and Techn. 33, 2017, 667-677.

[8s] Lapeire, L., Sidor, J., Verleysen, P., Verbeken, K., De Graeve, I, Terryn, H., Kestens, L.A.I. Texture comparison between room temperature rolled and cryogenically rolled pure copper. Acta Materialia. 95, 2015, 224–235.

[9s] Sidor, J.J., Decroos, K., Petrov, R.H., Kestens, L.A.I. Evolution of recrystallization textures in particle containing Al alloys after various rolling reductions: experimental study and modeling. International Journal of Plasticity. 66, 2015, 119–137.

[10s] Sidor, J.J., Petrov, R.H., Kestens, L.A.I. Modeling the crystallographic changes in processing of Al alloys. Journal of Materials Science. 9, 2014, 3529-3540.

[11s] Xie, Q., Van Bael, A., Sidor, J., Moerman, J., Van Houtte, P. A new cluster type model for the simulation of textures of polycrystalline metals. Acta Mater. 69, 2014, 175–186.

[12s] Decroos, K., Sidor, J., Seefeldt, M. A new analytical approach for the velocity field in rolling processes and its application in through-thickness texture prediction. Metallurgical and Materials Transactions A. 45A, 2014, 948-961.

[13s] Sidor, J.J., Kestens, L.A.I. Analytical description of Rolling textures in face centered cubic metals. Scripta Materialia. 68, 2013, 273-276.

[14s] Nguyen-Minh T., Sidor, J.J., Petrov, R.H., Kestens, L.A.I. Occurrence of shear bands in rotated Goss ({110}<110>) orientations of metals with bcc crystal structure. Scripta Materialia. 67, 2012, 935-938.

[15s] Sidor, J., Petrov, R., Kestens, L.A.I. Modeling the Crystallographic Changes in Aluminum Alloys During Recrystallization. Acta Materialia. 59, 2011, 5735–5748.

[16s] Sidor, J., Petrov, R., Kestens, L.A.I. Texture Induced Anisotropy in Asymmetrically Rolled Aluminum Alloys. Advanced Engineering Materials. 13, 2011, 1-6.

[17s] Sidor, J., Petrov, R., Kestens, L.A.I. Microstructural and Texture Changes in Severely Deformed Aluminum Alloys. Materials Characterization. 62, 2011, 228-236.

[18s] Sidor, J., Petrov, R., Kestens, L.A.I. Deformation, Recrystallization and Plastic Anisotropy of Asymmetrically Rolled Aluminum Sheets. Materials Science and Engineering A. 528, 2010, 413–424.

[19s] Bennett, T.A., Sidor, J., Petrov, R.H., Kestens, L.A.I. The effect of intermediate annealing on texture banding in aluminium alloy 6016 that exhibits roping. Advanced Engineering Materials. 12, 2010, 1018-1023.

[20s] Sidor, J., Miroux, A., Petrov, R., Kestens, L. Microstructural and crystallographic aspects of conventional and asymmetric rolling processes. Acta Materialia. 56, 2008, 2495–2507.

[21s] Sidor, J., Miroux, A., Petrov, R., Kestens, L. Controlling the plastic anisotropy in asymmetrically rolled aluminium sheets. Philosophical Magazine. 88, Nos. 30–32, 2008, 3779–3792.

[22s] Pirgazi, H., Akbarzadeh, A., Petrov, R., Sidor, J., Kestens, L. Texture evolution of AA3003 aluminum alloy sheet produced by accumulative roll bonding. Materials Science and Engineering A. 492, 2008, 110–117.

[23s] Sidor, J.J., Xie, Q. Deformation Texture Modelling by Mean-Field and Full-Field Approaches. Advanced Materials Letters. 2019, 10(9), 643-650.

[24s] Sidor, J.J. Crystal plasticity and continuum mechanics-based modelling of deformation and recrystallization textures in aluminum alloys. IOP Conf. Series: Materials Science and Engineering. Vol. 375, 2018, 012028.

[25s] Van Houtte, P., Xie, Q., Van Bael, A., Sidor, J., Moerman, J. A new cluster-type statistical model for the prediction of deformation textures. IOP Conference Series: Materials Science and Engineering, Vol. 82, Issue 1, 24 April 2015, Article number 012015.

[26s] Shore, D., Van Bael, A., Sidor, J., Roose, D., Van Houtte, P., Kestens, L. Modelling the stored energy of plastic deformation for individual crystal orientations. IOP Conference Series: Materials Science and Engineering, Vol. 82, Issue 1, 24 April 2015, Article number 012052.

[27s] Sidor, J.J., Petrov, R.H., Decroos, K., Kestens, L.A.I. Modeling the recrystallization textures in particle containing Al alloys after various rolling reductions. In proceeding of 13th International Conference on Aluminum Alloys (ICAA13), June 3-7, 2012, Pittsburgh, PA, USA. pp. 299-304.

[28s] Sidor, J.J., Petrov, R.H., Kestens, L.A.I. Recrystallization textures in aluminum alloys: experimental study and modelling. In proceeding of Int. Conference on Texture of Materials – ICOTOM-2011, December 12-17, 2011, Mumbay, India. Materials Science Forum. Vols. 702-703, 2012, pp. 611-614.

[29s] Sidor, J.J., Decroos, K., Petrov, R.H., Kestens, L.A.I. Particle Stimulated Nucleation in Severely Deformed Aluminum Alloys. In proceeding of Int. Conference on Processing&Manufacturing of Advanced Materials - Thermec’ 2011, August 1-5, 2011, Quebec City, Canada. Materials Science Forum. Vols. 706-709, 2012, pp. 389-394.

[30s] Sidor, J., Petrov, R., Kestens, L.A.I. Improved plastic anisotropy in asymmetrically rolled 6xxx alloy. 3rd International Conference on Texture and Anisotropy of Polycrystals (ITAP-3). Göttingen, Germany. 23-25 September, 2009. Solid State Phenomena. Vol.160, 2010, pp.165-170.

[31s] Sidor, J., Kestens, L., Miroux, A., Petrov, R. Recrystallization texture development under various thermo-mechanical conditions in aluminium alloys. Light Metals. Edited by Geoff Bearne. TMS, 2009. USA, pp. 1221-1224.

[32s] Ghosh, M., Miroux, A., Sidor, J., Kestens, L. Deformation Textures And Plastic Anisotropy of AA6XXX At Warm Temperature. Aluminum Alloys: Fabrication, Characterization and Applications II. Eddited by Weimin Yin, Subodh K. Das and Zhengdong Long, TMS, 2009, USA. pp.101-106.

[33s] Sidor, J., Miroux, A., Petrov, R., Kestens, L. Texture Modification in Asymmetrically Rolled Aluminum Sheets. Ceramic Transactions, Volume 201A, Collection of Papers Presented at the 15th International Conference on Texture in Materials (ICOTOM 15). June 1-6, 2008 Pittsburgh, Pennsylvania. Edited by A. Rollet. pp.547-554.

[34s] Sidor, J., Zhuang, L., Van Der Winden, M., Kestens, L. Effect of asymmetric rolling on texture and anisotropy of AA6016alloy for automotive applications. Proc. of TMS – 2008 Conference. March 9-13, 2008. New Orleans, USA. Editors: Y. Yin, S.K. Das. pp. 113-118.

[35s] Sidor, J., Kestens, L., Petrov, R., Miroux, A., Zhuang, L., Van Der Winden, M., De Smet, P., Ratchev, P. Deformation and Recrystallization Texture Control in 6016 Al alloy. Proceeding of Int. Conference ICAA-11. Edited by J. Hirsch, B. Skrotzki, G. Gottstein. Wiley-VCH Verlah GmbH&Co. KGaA, Weinheim-2008. Vol.2, pp.1149-1155.

[36] Wronski, S., Ghilianu, B., Chauveau, T., Bacroix, B. Analysis of textures heterogeneity in cold and warm asymmetrically rolled aluminium. Mater. Charact. 62, 2011, 22–34.

[37] Jin, H., Lloyd, D.J. Evolution of texture in AA6111 aluminum alloy after asymmetric rolling with various velocity ratios between top and bottom rolls. Mater. Science and Engineering A. 465, 2007, 267–273.

[38] Shimamura, T., Sakai, T., Utsunomiya, H., Kaneko, S. Texture and microstructure control of Al-Mg-Si alloy sheet by differential speed rolling. Mater. Sc. Forum. 558-559, 2007, 1443-1447.

[39] Lee, D.N. Asymmetric Rolling as Means of Texture and Ridging Control and Grain Refinement of Aluminum Alloy and Steel Sheets. Mater. Sc. Forum. 449-452, 2004, 1-7.

[40] Sakai, T., Yoneda, K., Osugi, S. Microstructure and Texture Control of Al-Mg Alloy Sheets by Differential Speed Rolling. Materials Science Forum. 495-497, 2005, 597-602.

[41] Kim, K-H., Lee, D.N. Analysis of deformation textures of asymmetrically rolled aluminum sheets. Acta Materialia. 49, 2001, 2583–2595.

[42] Lee, J-K., Lee, D.N. Texture control and grain refinement of AA1050 Al alloy sheets by asymmetric rolling. International Journal of Mechanical Sciences. 50, 2008, 869–887.

[43] Beausir, B., Biswas, S., Kim, D.I., Tóth, L.S., Suwas, S. Analysis of microstructure and texture evolution in pure magnesium during symmetric and asymmetric rolling. Acta Materialia. 57, 2009, 5061-5077.

[44] Uniwersał, A., Wroński, M., Wróbel, M., Wierzbanowski, K., Baczmański, A. Texture effects due to asymmetric rolling of polycrystalline copper. Acta Materialia. 139, 2017, 30-38.

[45] Wronski, S., Bacroix, B. Microstructure evolution and grain refinement in asymmetrically rolled aluminium. Acta Materialia. 76, 2014, 404-412.

[46] Zhang, T., Li, L., Shi-hong, L., Zhang, J., Gong, H. Comparisons of flow behavior characteristics and microstructure between asymmetrical shear rolling and symmetrical rolling by macro/micro coupling simulation. J. of Computational Sc. 29, 2018, 142-152.

[47] Xie, Y., Deng, Y., Wang, Y., Guo, X. Effect of asymmetric rolling and subsequent ageing on the microstructure, texture and mechanical properties of the Al-Cu-Li alloy. Journal of Alloys and Compounds. 836, 2020, Article 155445.

[48] Afifeh, M., Hosseinipour, S. J. Jamaati, R. High-strength and high-conductivity nanograined copper fabricated by partial homogenization and asymmetric rolling. Materials Science and Engineering: A. 768, 2019 Article 138451.

[49] Ren, X., Huang, Y., Liu, Y., Zhao, Y., Li, H. Evolution of microstructure, texture, and mechanical properties in a twin-roll cast AA6016 sheet after asymmetric rolling with various velocity ratios between top and bottom rolls. Materials Science and Engineering A. 788, 2020Article, 139448.

[50] Kocks, U.F., Tomé, C.N., Wenk, H.-R. Texture and Anisotropy. Preferred Orientations in Polycrystals and their Effect on Materials Properties. (1998) Cambridge University press.

[51] Humphreys, F.J., Hatherly M. Recrystallization and related annealing phenomena 2nd edn. (2004) Elsevier, Oxford.

[52] Bunge, H. Texture Analysis in Materials Science. (1982) Butterworth, London.

[53] Hirsch, J., Lucke, K. Overview no. 76: Mechanism of deformation and development of rolling textures in polycrystalline f.c.c. metals—II. Simulation and interpretation of experiments on the basis of Taylor-type theories. Acta Metall. 36, 1988. 2883-2904.

[54] Engler, O. On the influence of orientation pinning on growth selection of recrystallisation. Acta mater. 46, 1998, 1555-1568.

[55] Bhattacharjee, P.P., Ray, R.K., Tsuji, N. Cold rolling and recrystallization textures of a Ni–5at.% W alloy. Acta Materialia. 57, 2009, 2166-2179.

[56] Escher, C., Neves, S., Gottstein, G. Recrystallization texture evolution in Ni3Al. Acta mater. 46, 1998, 441-450.

[57] Huang, K., Engler, O., Li, Y.J. Marthinsen, K. Evolution in microstructure and properties during non-isothermal annealing of a cold-rolled Al–Mn–Fe–Si alloy with different microchemistry states. Mater. Sc. Eng. A. 2015, 628, 216–229.

[58] Bracke, L., Verbeken, K., Kestens, L., Penning, J. Microstructure and texture evolution during cold rolling and annealing of a high Mn TWIP steel. Acta Materialia. 57, 2009, 1512-1524.

[59] El-Danaf, E., Kalidindi, S.R., Doherty, R.D., Necker, C. Deformation texture transition in brass: critical role of micro-scale shear bands. Acta Mater. 48, 2000, 2665-2673.

[60] Vercammen, S., Blanpain, B., De Cooman, B.C., Wollants, P. Cold rolling behaviour of an austenitic Fe–30Mn–3Al–3Si TWIP-steel: the importance of deformation twinning. Acta Mater. 52, 2004, 2005-2012.

[61] Weidner, A., Klimanek, P. Shear Banding and Texture Development in Cold-Rolled α-Brass. Scripta Mater. 38, 1998, 851-856.

[62] Ridha, A.A., Hutchinson, W.B. Recrystallisation mechanisms and the origin of cube texture in copper. Acta Metall. 30, 1982, 1929-1939.

[63] Muzyk, M., Pakiela, Z., Kurzydlowski, K.J. Ab initio calculations of the generalized stacking fault energy in aluminium alloys. Scripta Mat. 64, 2011, 916-918.

[64] Heye, W., Wassermann, G. The formation of the rolling textures in FCC metals by slip and twinning. Scripta Metall. 2, 1968, 205-207.

[65] Dillamore, I.L., Roberts, W.T. Rolling textures in f.c.c. and b.c.c. metals. Acta Metal. 12, 1964, 281-293.

[66] Holscher, M., Raabe, D., Lucke, K. Relationship between rolling textures and shear textures in f.c.c. and b.c.c. metals. Acta Metall Mater. 42, 1994, 879-886.

[67] Hansen, N., Juul Jensen, D. Deformation and recrystallization textures in commercially pure aluminum. Metall. Trans. A. 17, 1986, 253-259.

[68] Engler, O., Randle, V. Introduction to texture analysis. Macrotexture, microtexture and orientation mapping. Second ed. (2010) Boca Raton, CRC Press, Taylor & Francis Group.

[69] Raabe, D. Computational Materials Science, 1st ed., (1998) WILEY-VCH: New York, USA, pp. 111–298.

[70] Lenard, J.G., Pietrzyk, M, Cser, L. Physical Simulation of The Properties of Hot Rolled Products, 1st ed., (1999) Elsevier: Oxford, UK, pp. 61–317.

[71] Delannay, L., Jacques, P. J., Kalidindi, S. R. Finite element modeling of crystal plasticity with grains shaped as truncated octahedrons. Int. J. Plast. 22, 2006, 1879-1898.

[72] Lebensohn, R. A., Kanjarla, A. K., Eisenlohr, P. An elasto-viscoplastic formulation based on fast Fourier transforms for the prediction of micromechanical fields in polycrystalline materials. Int. J. Plast. 32–33, 2012, 59-69.

[73] Van Houtte, P., Li, S., Seefeldt, M., Delannay, L. Deformation texture prediction: from the Taylor model to the advanced Lamel model. Int. J. Plast. 21, 2005, 589-624.

[74] Van Houtte, P., Kanjarla, A. K., Van Bael, A., Seefeldt, M., Delannay, L. Multiscale modeling of the plastic anisotropy and deformation texture of polycrystalline materials. European J. Mech. A/Solids. 25, 2006, 634-648.

[75] Lebensohn, R. A., Tome, C. N. A self-consistent anisotropic approach for the simulation of plastic deformation and texture development of polycrystals: application to zirconium alloys. Acta Metal. Mater. 41, 1993, 2611-2624.

[76] Mao, W. On the Taylor principles for plastic deformation of polycrystalline metals. Front. Mater. Sci. 10, 2016, 335-345.

[77] Engler, O., Huh, M.-Y., Tome, C. N. A study of through-thickness texture gradients in rolled sheets. Met. Mat. Trans. A. 31, 2000, 2299-2315.

[78] Zhang, S. H., Zhao, D. W., Gao, C. The calculation of roll torque and roll separating force for broadside rolling by stream function method. Int. J. Mech. Sc. 57, 2012, 74-78.

[79] Dogruoglu, A. N. On constructing kinematically admissible velocity fields in cold sheet rolling. J. Mater. Proc. Techn. 110, 2001, 287-99.

[80] Beausir, B., Toth, L. S. In Microstructure and texture in steels and other materials, 1st ed., Haldar, A., Suwas, S., Bhattacharjee, D., Eds., (2009) Springer-Verlag London Ltd: London, UK, pp. 415-417.

[81] Tian, Y., Guo, Y-H., Wang, Z-D., Wang G-D. Analysis of Rolling Pressure in Asymmetrical Rolling Process by Slab Method. Journal of Iron and Steel Research International 16, 2009, 22-26.

[82] Aboutorabi, A., Assempour, A., Afrasiab, H. Analytical approach for calculating the sheet output curvature in asymmetrical rolling: In the case of roll axis displacement as a new asymmetry factor. International Journal of Mechanical Sciences. 105, 2016, 11-22.

[83] Liu, Y-M., Ma, G-S., Zhang, D-H., Zhao, D-W. Upper bound analysis of rolling force and dog-bone shape via sine function model in vertical rolling. Journal of Materials Processing Technology. 223, 2015, 91-97.

[84] Tome, C. N., Canova, G. R., Kocks, U. F., Christodoulou, N, Jonas, J. J. The relation between macroscopic and microscopic strain hardening in FCC polycrystals. Acta Metall. 32, 1984, 1637–1653.

[85] Han, C.-S., Ma, A., Roters, F., Raabe, D. A finite element approach with patch projection for strain gradient plasticity formulations. Int. J. Plast. 23, 2007, 690–710.

[86] Van Houtte, P., Kumar Yerra, S., Van Bael, A. The facet method: a hierarchical multilevel modelling scheme for anisotropic convex plastic potentials. Int. J. Plast. 25, 2009 332–360.

[87] Lee, S.-B., Lebensohn, R.A., Rollett, A.D. Modeling the viscoplastic micromechanical response of two-phase materials using Fast Fourier Transforms. Int. J. Plast. 27, 2011, 707-727.

[88] Lee, C. S., Duggan, B. A simple theory for the development of inhomogeneous rolling textures. Metall. Mater. Trans. A. 22, 1991, 2637–2643.

[89] Dawson, P. R., Boyce, D. E., Rogge, R. Issues in modeling heterogeneous deformations in polycrystalline metals using multiscale approaches. Comput. Model. Eng. Sci. 10, 2005, 123–141.

[90] Mishin, O. V., Bay, B., Winther, G., Juul Jensen, D. The effect of roll gap geometry on microstructure in cold-rolled aluminum. Acta Mater. 52, 2004, 5761-5770.

[91] Truszkowski, W., Krol, J., Major, B. Inhomogeneity of rolling texture in fcc metals Metall. Trans. A. 11, 1980, 749-758.

[92] Tian, Y., Guo, Y.-H., Wang, Z.-D., Wang, G.-D. Analysis of Rolling Pressure in Asymmetrical Rolling Process by Slab Method. J. Iron Steel Res. Int. 16, 2009, 22–26.

[93] Aboutorabi, A., Assempour, A., Afrasiab, H. Analytical approach for calculating the sheet output curvature in asymmetrical rolling: In the case of roll axis displacement as a new asymmetry factor. Int. J. Mech. Sci. 105, 2016, 11–22.

[94] 18. Liu, Y.-M., Ma, G.-S., Zhang, D.-H., Zhao, D.-W. Upper bound analysis of rolling force and dog-bone shape via sine function model in vertical rolling. J. Mater. Process. Technol. 223, 2015, 91–97.

[95] Avitzur, B. Friction-aided strip rolling with unlimited reduction. Int. J. Mach. Tool. Des. Res. 20, 1980, 197–210.

[96] Kang, S.-B., Min, B. K., Kim, H. W., Wilkinson, D. S., Kang, J. Effect of Asymmetric Rolling on the Texture and Mechanical Properties of AA6111 – Aluminum Sheet. Metall. Mater. Trans. A. 36, 2005, 3141–3149.

[97] Cui, Q., Ohori, K. Grain Refinement of High Purity Aluminium by Asymmetric Rolling. Mater. Sci. Tech. 2000, 16, 1095–1101.

[98] Saito, Y., Sakai, T., Maeda, F., Kato, K. Deformation and Recrystallization Behavior of Ferritic Stainless Steel in High Speed Hot Rolling. Tetsu-to-Hagane 72, 1986, 799–806.

[99] Saito, Y., Utsunomiya, H., Tsuji, N., Sakai, T. "Novel Ultra-High Straining Process for Bulk Materials - Development of the Accumulative Roll-Bonding (ARB)". Acta Materialia. 47 (2), 1999, 579–583.

[100] Tsuji, N., Saito, Y., Lee, S.-H., Minamino, Y. "ARB (Accumulative Roll-Bonding) and other new Techniques to Produce Bulk Ultrafine Grained Materials". Advanced Engineering Materials. 5 (5), 2003, 338-344.

[101] Kim, H. W., Kang, S. B., Tsuji, N., Minamino, Y. Deformation textures of AA8011 aluminum alloy sheets severely deformed by accumulative roll bonding. Metallurgical and Materials Transaction A. 36, 2005, 3151–3163.

[102] Heason, C.P., Prangnell, P.B. Texture Evolution and Grain Refinement in Al Deformed to Ultra-High Strains by Accumulative Roll Bonding (ARB). Materials Science Forum. 408–412, 2002, 733–738.

[103] Kamikawa, N., Tsuji, N., Huang, X., Hansen, N. Quantification of annealed microstructures in ARB processed aluminum. Acta Materialia. 54, 2006, 3055–3066.

[104] Ashby, M.F. Work hardening of dispersion-hardened crystals. Phil. Mag. 14, 1966, 1157–1178.

[105] Ashby, M.F. The deformation of plastically non-homogeneous materials. Phil. Mag. 21, 1970, 399–424.

[106] Humphreys, F.J. The nucleation of recrystallization at second phase particles in deformed aluminium. Acta Metall. 25, 1977, 1323–1344.

[107] Xu, W., Ferry, M., Cairney, J.M., Humphreys, F.J. Three-dimensional investigation of particle-stimulated nucleation in a nickel alloy. Acta Mater. 55, 2007, 5157–5167.

[108] Humphreys, F.J. Local lattice rotations at second phase particles in deformed metals. Acta Metall. 27, 1979, 1801–1814.

[109] Engler, O. Influence of particle stimulated nucleation on the recrystallization textures in cold deformed Al-alloys Part II—modeling of recrystallization textures. Scripta Mater. 37, 1997, 1675–1683.

[110] Liu, Q., Yao, Z., Godfrey, A., Liu, W. Effect of particles on microstructural evolution during cold rolling of the aluminum alloy AA3104. J. Alloy. Compd. 482, 2009, 264–271.

[111] Pinto De Siqueira, R., Zschommler Sandim, H.R., Raabe, D. Particle stimulated nucleation in coarse-grained ferritic stainless steel. Metal. Mater. Trans. A. 44, 2013, 469–478.

[112] Humphreys, F.J., Ardakani, M.G. The deformation of particle-containing aluminium single crystals. Acta Metall. Mater. 42, 1994, 749–761.

[113] Lücke, K, Engler, O. Effects of particles on development of microstructure and texture during rolling and recrystallisation in fcc alloys. Materials Science and Technology. 6, 1990, 1113-1130.

[114] Albou, A., Raveendra, S., Karajagikar, P., Samajdar, I., Maurice, C., Driver, J.H. Direct correlation of deformation microstructures and cube recrystallization nucleation in aluminium. Scripta Mater. 62, 2010, 469-472.

[115] Etter, A.L., Mathon, M.H., Baudin, T., Branger, V., Penelle, R. Influence of the cold rolled reduction on the stored energy and the recrystallization texture in a Fe–53%Ni alloy. Scripta Mater. 46, 2002, 311-317.

[116] Baudin, T., Solas, D., Etter, A.L., Ceccaldi, D., Penelle R. Simulation of primary recrystallization from TEM observations and neutron diffraction measurements. Scripta Mater. 51, 2004, 427-430.

[117] Hutchinson, B. Deformation microstructures and textures in steels. Phil. Trans. R. Soc. Lond. A. 357, 1999, 1471-1485.

[118] Daaland, O., Nes, E. Recrystallization texture development in commercial Al-Mn-Mg alloys. Acta Materialia, 44, 1996, 1413-1435.

[119] Jiang, J., Ding, Y., Zuo, F., Shan, A. Mechanical properties and microstructures of ultrafine-grained pure aluminum by asymmetric rolling. Scripta Mater. 60, 2009, 905–908.

[120] Ding, Y., Jiang, J., Shan, A. Microstructures and mechanical properties of commercial purity iron processed by asymmetric rolling. Mater. Sc. and Eng. A. 509, 2009, 76–80.

[121] Farè, S., Vedani, M., Angella, G. Features on Grain-Structure Evolution During Asymmetric Rolling of Aluminium Alloys. Mater. Sc. Forum. 604-605, 2009, 77-85.

[122] Jin, H., Lloyd, D.J. Development of Grain Structure and Texture during Annealing in Asymmetrically Rolled AA5754. Materials Science Forum. 467-470, 2004, 381-386.

[123] Jin, H., Lloyd, D.J. The Tensile Response of a Fine-Grained AA5754 Alloy Produced by Asymmetric Rolling and Annealing. Metal. and Mater. Trans. A. 35, 2004, 997-1006.

[124] Jin, H., Lloyd, D.J. Effect of a duplex grain size on the tensile ductility of an ultra-fine grained Al–Mg alloy, AA5754, produced by asymmetric rolling and annealing. Scripta Materialia. 50, 2004, 1319–1323.

[125] Abbruzzese, G., Lucke, K. A theory of texture controlled grain growth—I. Derivation and general discussion of the model. Acta Metall. 34, 1986, 905-914.

[126] Jonas, J.J., Toth, L.S. Modelling oriented nucleation and selective growth during dynamic recrystallization. Scripta Metall Mater. 27, 1992, 1575-1580.

[127] Engler, O., Löchte, L., Hirsch, J. Through-process simulation of texture and properties during the thermomechanical processing of aluminium sheets. Acta Mater. 55, 2007, 5449-5463.

[128] Ko, K.-J., Rollett, A.D., Hwang N.-M. Abnormal grain growth of Goss grains in Fe–3% Si steel driven by sub-boundary-enhanced solid-state wetting: Analysis by Monte Carlo simulation. Acta Mater. 58, 2010, 4414-4423.

[129] Raabe, D., Hantcherli, L. 2D cellular automaton simulation of the recrystallization texture of an IF sheet steel under consideration of Zener pinning. Computational Mater. Sc. 34, 2005, 299-313.

[130] Vatne, H.E., Furu, T., Øsrund, R., Nes, E. Modelling recrystallization after hot deformation of aluminium. Acta Mater. 44, 1996, 4463-4473.

[131] Engler, O. Simulation of the recrystallization textures of Al-alloys on the basis of nucleation and growth probability of the various texture components. Textures and Microstructures. 28, 1997, 197-209.

[132] Rajmohan, N., Szpunar, J.A. A new model for recrystallization of heavily cold-rolled aluminum using orientation-dependent stored energy. Acta Mater. 48, 2000, 3327-3340.

[133] Schäfer, C., Song, J., Gottstein, G. Modeling of texture evolution in the deformation zone of second-phase particles. Acta Mater. 57, 2009,1026-1054.

[134] Hutchinson, B. Critical Assessment 16: Anisotropy in metals. Materials Science and Technology. 31, 2015, 1393-1401.

[135] Engler, O. An EBSD local texture study on the nucleation of recrystallization at shear bands in the alloy Al-3%Mg. Scripta Materialia. 44, 2001, 229-236.